The Thesis Committee for Hualing Zhang
Certifies that this is the approved version of the following thesis:

Lithofacies, Diagenesis, and Reservoir Quality of the Unconventional Wolfcampian Succession in the Southeast Midland Basin, West Texas

APPROVED BY
SUPERVISING COMMITTEE:

Supervisor:

Xavier Janson

Co-Supervisor:

Qilong Fu

Charles Kerans

Ronald J Steel

Lithofacies, Diagenesis, and Reservoir Quality of the Unconventional Wolfcampian Succession in the Southeast Midland Basin, West Texas

by

Hualing Zhang

Thesis

Presented to the Faculty of the Graduate School of

The University of Texas at Austin

in Partial Fulfillment

of the Requirements

for the Degree of

Master of Science in Geological Sciences

The University of Texas at Austin

August 2017

Dedication

To my parents.

Acknowledgements

Foremost, I would like to thank my supervisors Dr. Xavier Jason and Dr. Qilong Fu for their guidance, insight, and support during my time at the University of Texas at Austin. I would also like to thank my committee members Dr. Charles Kerans and Dr. Roland J Steel for their advices and guidance. Additionally, I would like to thank the PI of my project William A Ambrose for his guidance and support, and thank the State of Texas Advanced Oil and Gas Resources Recovery (STARR) for funding my research project.

Major thanks to the researcher at the Bureau of Economic Geology (BEG). Thank Dr. H. Scott Hamlin, Dr. Stephen C Ruppel, Dr. Shirley P. Dutton, Robert Baumgardner, and Tucker F. Hentz for all of their assistance, insights, and comments on my thesis. I would like to thank the BEG Core Research Center staffs: Nathan Ivicic, Brandon Williamson, James Donnelly, Evan and Rudy provided great help for my core data collection process. I really appreciate their time and efforts. I also would like to thank Patrick Smith for his assistant on my SEM sample observation and his support on my research. Additionally, I would like to thank Ganser, John Grillo, Jarred Garza from the Premier Oilfield Laboratories for their help in the attainment of the XRF, XRD, and TOC data.

Thanks to my colleagues: Junwen Peng, Jin Lai, Zhaoqi Li, Lucy Ko, Lei Jiang, Ian Moede, Ziyuan Wang, Heng Zhang, Li Liu, Hanyue Zheng, Zhaohui Xu, Ningjie Hu for providing help with my research. Thanks to my dear friends: Tianjian Cheng, Mingyu

Yang, Takonporn Kunpitaktakun, Brooklyn Gose, Yawen He, Chuyi Wen, Dong Yan, Yang Shao, Xia Wu, Boxue Chen, Zongyao Li, Miaomiao Meng, Wentao Wang for their endless support and encouragement.

Finally, I would like to thank my Mom and Dad for their lifelong encouragement, support, and love. I could never accomplish anything without you.

Abstract

Lithofacies, Diagenesis, and Reservoir Quality of the Unconventional Wolfcampian Succession in the Southeast Midland Basin, West Texas

Hualing Zhang, M.S. Geo. Sci

The University of Texas at Austin, 2017

Supervisors: Xavier Janson, Qilong Fu

The Lower Permian Wolfcampian basinal succession in the Midland Basin has become an important unconventional reservoir. Reservoir characterization of Wolfcampian strata is challenging because of the complex arrangement of lithofacies. This study combined petrographic and scanning electron microscope (SEM) cube observations from cores, and thin sections, as well as X-ray fluorescence (XRF) data, X-ray diffraction (XRD) data, and total organic carbon (TOC) data in order to provide an integrated characterization of the Wolfcamp succession.

Lithofacies investigations were made using six cores (totally 667 ft total) from Glasscock, Sterling, and Irion Counties in Texas. Seven lithofacies were defined based on petrographic observations: (1) sandy siltstone, (2) argillaceous mudstone, (3) very fine to fine sandstone, (4) massive to weakly laminated calcareous mudstone, (5) laminated calcareous mudstone, (6) mud-dominated bioclastic packstone/rudstone, and (7) grain-dominated bioclastic packstone-grainstone/rudstone. Mudrocks were deposited mostly through hemipelagic settling and diluted turbidity flow. Depositional processes for

sandstone, siltstone, and carbonate lithofacies include turbidity flows, debris flows, and hyperconcentrated density flows. These sediments are interpreted to be deposited in a deep-water, dysoxic to anoxic slope to basinal setting. High-frequency cyclicity is observed in meter scale as a relative carbonate-rich lithofacies overlain by a relative siliclastic-rich lithofaices.

The Wolfcamp succession reveals a complex diagenetic history in sandstone and carbonate facies, including compaction, calcite, silica, and siderite cementation, and dissolution. The combined effects of compaction and cementation result in relatively low porosity. However, dissolution and siderite grain-coating in the sandstones create/save pore spaces for hydrocarbon storage. Measured core-plug porosity and permeability (por–perm) in sandstone successions suggest moderate porosity up to 11.6%. Based on por–perm results, siderite-coated sandstone is considered to be of the highest reservoir potential. The Wolfcamp has fair to good organically rich mudrocks, with an average TOC of 1.4%. TOC is facies-dependent with the highest value in the argillaceous mudstone lithofacies. The enrichment of organic matter increases with increasing primary productivity by showing positive relation with Ni, Cu, and P element. Organic enrichment also increases with bottom water anoxia by showing a positive relation with Mo and U elements. TOC enrichment is also affected by sediment influx during early Wolfcampian.

Table of Contents

List of Tables xi

List of Figures xii

Introduction 1

Study Area 2

Previous Work 3

Research Objectives 4

Geological Setting 6

Regional Tectonism 6

Stratigraphy and Paleogeography 7

Glaciation and Eustasy 9

Methods and Dataset 13

Petrographic Observation 13

Core Description 13

Thin Sections Analysis 16

SEM Analysis 16

Core Plugs Analysis 17

Chemostratigraphic Data 17

XRF Analysis 17

XRD and TOC analysis 19

Results 20

Lithofacies and Interpreted Depositional Environment 20

Sandy Siltstone 23

Argillaceous Mudstone 27

Very Fine to Fine Sandstone 30

Massive to Weakly Laminated Calcareous Mudstone 34

Laminated Calcareous Mudstone 39

Mud-dominated Bioclastic packstone/Rudstone 44

Grain-dominated Bioclastic Packstone-Grainstone/Rudstone.....47
Diagenesis and Pore Evolution.....50
Compaction.....50
Dissolution.....51
Silica Cementation.....51
Siderite Coating.....52
Calcite Cementation.....52
Geochemical data integration.....57
XRF-based Facies Correlations.....57
Cyclicity.....62
Paleoenvironment and TOC Preservation.....65
Reservoir Potential Evaluation.....70
Discussion.....74
Depositional setting.....74
Depositional cyclicity.....74
TOC preservation and reservoir quality.....75
Conclusions.....77
Appendix: Wolfcampian Core Description.....79
References.....103
Vita.....113

List of Tables

Table 3-1: Table of cored wells, located in Figure 1. 14

Table 4-1: Summary of Wolfcampian succession lithofacies and interpreted depositional process. 21

Table 4-1 (continued).....22

List of Figures

Figure 1-1: Map of the Permian Basin area with major basin structures (from Fu et al., in press). Study area in the red box with core location, and the boundary of the Eastern Shelf is in blue dash line (from Hamlin and Baumgardner, 2012). 2

Figure 2-1: Stratigraphic and operational names used in oil industry of formations in the Midland Basin (Modified from Baumgardner et. al, 2016). 8

Figure 2-2: North American paleogeographic map of in Early Permian, ca. 290 Ma, highlighting the Permian Basin region (From Blakey, 2017). 9

Figure 2-3: Timing, duration, and character of the late Paleozoic Ice Age (Veevers & Powell 1987; Frakes & Francis 1988; Crowley & Baum 1991, 1992; Frakes et al. 1992; Crowell 1999; Isbell et al. 200) and recognized glacial intervals (from Fielding et al., 2008b).....10

Figure 2-4: Stratigraphic intervals and corresponding eustacy curve in Lower Permian (Modified from Ross and Ross, 1987). 11

Figure 3-1: Northwest to southeast cross section displaying core positions and stratigraphic units. 15

Figure 4-1: Mudstone nomenclature diagram based on mineral composition (from Lazar et al., 2015). Si= siliceous, ca=calcareous, Ar= argillaceous .20

Figure 4-2: (A) Slabbed core photo of sandy siltstone with ripped up clasts (in the red box), Noelke #38, 6702.8-6703.4 ft. (B) Wavy lamination, Rocker "B" #3031-3, 7765.1 ft. (C) Inclined wavy lamination, State University #1-EM, 7062 ft. (D) Soft sediment deformation present locally, State University #1-EM, 7066 ft. (E) Sandy siltstone topped by fine to very fine sandstone facies with scouring surface, Noelke #38, 6671-6672 ft. 25

Figure 4-3: Photomicrographs of sandy siltstone: (A)(B) Mineral composition is dominated by quartz grains and clay-sized sediments, Noelke #38, 6696.4 ft, State University #1-EM, 7063.9 ft. (C) Quartz gains are poorly sorted, angular to sub-angular shape. (D) Quartz grains can rich up to 120 micron. (E)Sandy siltstone laminate with very fine sandstone, Sterling Fee #6-G, 7642.5 ft, State University #1-EM, 7063.9 ft. (F) Quartz grains in sand laminae are poorly sorted, sub-angular to sub-rounded shape, very-fine sandstone size, State University #1-EM, 7063.9 ft. 26

Figure 4-4: Slabbed core photo of argillaceous mudstone, broken, minor lamination locally, Noelke #38, 6681-6690 ft. 28

Figure 4-5: Photomicrographs of argillaceous mudstone. (A) Argillaceous mudstone, clay mineral dominated, with minor quartz grains. Pyrite is sparsely present. Sterling Fee #6-G, 7706.9 ft. (B), (C) and (D) Argillaceous mudstone in Powell E.L #1, 8841 ft. 29

Figure 4-6: (A) SEM images of Noelke #38, 6681.6 ft. (B) SEM-EDS images. Quartz grains (in red) are sub-angular to sub-rounded shape. Directional alignment of clay minerals (mixture of yellow and green) indicates compaction. Albite presents locally (in blue). Abundant organic matters (in black) present, Noelke #38, 6681.6 ft.....30

Figure 4-7: Slabbed core photo of very fine to fine sandstone. (A) Sandstone beds show overall fining upward trend from massive bed (Bouma A) to bed with planar lamination (Bouma B). Flame structure (dash line). Noelke #38, 6712-6712.6 ft. (B) Multiple finning upward sequences followed by ripple lamination (dash line) at the top, Noelke #38, 6739-6740 ft. (C) Planar laminated sandstone topped by mudstone. Soft sediment deformation at the contact (dash line), Noelke #38, 6665.5. (D) Massive sandstone with ripped-up clay clast, Noelke #38, 6672.9 ft. (E) Load structure (red box) present at the base of planar laminated sandstone, which overlies mudstone. (F) Fluid escape structure (red arrow) cutting through planar laminated sandstone. Flame structure (dash line). Noelke #38, 6713.8 ft. (G) Normal grading, Rocker “B” #3031-3, 7730 ft..32

Figure 4-8: Photomicrographs of very fine to fine sandstone. **(A)** Sandstone with mud stripes (red arrow), State University #1-EM, 7057.6 ft. **(B)** A zoom in view of sandstone with mud stripe, clay minerals (c) in the muddy stripe occlude the pore space, Noelke #38, 6721.8 ft. **(C)** Sandstone with big mud clast (to the left), Sterling Fee #6-G, 7689.2 ft. **(D)** Quartz grains have long contact (red arrow). Presence of dissolution pore (P), Sterling Fee #6-G, 7948.2 ft. **(E), (F)** Massive fine-grain sandstone, rock fragments (R) present as a small amount, feldspar is very rarely present, Sterling #6-G, 7669 ft. 33

Figure 4-9: Slabbed core photo of massive to weakly laminated calcareous mudstone of the Harwood Trust #2 core. (A) Massive calcareous mudstone, 7598.6-7599.5 ft. (B) Calcareous mudstone with very weak lamination (arrow), 7491-7492 ft. (C) Calcareous mudstone shows coarsening upward trend with a sharp contact (arrow) towards to top, 7596.5-7597.5 ft. (D) Calcareous mudstone brecciated locally. The cracks are filled by calcite cement (arrow).....36

Figure 4-10: Photomicrographs of massive to weakly laminated calcareous mudstone in Harwood Thrust #2 core. **(A), (B)** Massive to weakly laminated calcareous mudstone, 7498.3 ft. **(C)** Minor gastropode (G) fragments, 7489.3 ft. **(D)** Rardiolarins (R) are commonly present, 7489.3 ft. **(E)** The infilling cement is dominated by calcite, 7497.7 ft. **(F)** Locally brecciated calcareous mudstone, 7497.7 ft. 37

Figure 4-11: SEM and EDS images of Massive to Weakly Laminated calcareous mudstone, Harwood Trust #2, 7486.6 ft (A) SEM images of calcareous mudstone. (B) SEM-EDS images. Fossil fragments are in dark blue, clay minerals are dominated by illite (in green), some quartz grains (in red) are poorly sorted, pyrite framboids (upper right, in white) are commonly present, albite presents locally (in dark blue). (C) SEM images of organic matter (bitumen) (in red arrow) filling into the space between minerals. (D) SEM-EDS image shows pyrite rims are commonly seen around dolomite grains. 38

Figure 4-12: Slabbed core photo of laminated calcareous mudstone in Harwood Trust #2 core. **(A)** Laminated calcareous mudstone, 7709-7710 ft. **(B)** Load structure (arrow), 7669.1 ft. **(C)** Laminated calcareous mudstone (L) fines up into weakly laminated to massive calcareous mudstone (M), 7684 ft. **(D)** Lamination with small scale finning upward trend, 7718.9 ft. 41

Figure 4-13: Photomicrographs of laminated calcareous mudstone. (A) Lamination is caused by grain size difference, Harwood Trust #2, 7554.6 ft. (B) Lamination is caused by grain size difference (the thin section was half stained), Harwood Trust #2, 7710.4 ft. (C) Miliolid foraminifer (red arrow) in the laminated bioclastic packstone, Harwood Trust #2, 77695.7 ft. (D) Gastropod fragment (red arrow) in the laminated wackestone, Harwood Trust #2, 7652 ft. 42

Figure 4-14: (A) SEM image of laminated calcareous mudstone and bioclastic packstone, Harwood Trust #2, 7679 ft. (B) SEM-EDS image: organic matters (in black) are less common compared to calcareous mudstone. Quartz grains (in red) and albite (in blue) are presence as a small amount.....43

Figure 4-15: Slabbed core photo of mud-dominated bioclastic packstone/rudstone. (A) Skeletal fragments floating in the matrix rich sediments, Powell E.L #1, 8910-8911 ft. (B) Crinoid fragments are commonly seen (red box). It is topped by calcareous mudstone with a sharp contact, Powell E.L #1, 8905-8906 ft.....45

Figure 4-16: Photomicrographs of mud-dominated bioclastic packstone/rudstone, Powell E.L #1core. **(A)** Bryozoan fragment, 8907.6 ft. **(B)** Epimastoporid algae (arrow), 8907.6 ft. **(C)** Bivalve fragments, 8907.6 ft. **(D)** Large fusulinid fragment partially lose its internal structure due to quartz replacement, intraparticle pores are filled with calcite cements, 8907.6 ft. **(E)** Lithoclasts (L) present locally, 8907.6 ft. **(F)** Radiolarian (red arrow) showing concentric structure, 8822.3 ft.....46

Figure 4-17: Slabbed core photo of grain-dominated bioclastic packstone-grainstone/rudstone in Harwood Trust #2 core. (A) Mollusk fragment (arrow) and other fossil fragment commonly present, 7572.8 ft. (B) Grain-dominated bioclastic packstone-grainstone/rudstone with muddy stripe, 7672.8 ft. (C) Concentrated fusulinid (red arrow) and visible porosity (yellow arrow), 7574.8 ft. 48

Figure 4-18: Photomicrographs of grain-dominated bioclastic packstone-grainstone/rudstone, Harwood Trust #2. **(A)** Lithoclast (L) and fusulinid (F) in bioclast grainstone, 7570.8 ft. **(B)** Crinoid (Cr), epimastoporids algae (E) in bioclast grainstone, thin section was half stained, 7569.2 ft. **(C)** Large bryozoan fragment in bioclast rudstone, 7570 ft. **(D)** Dissolution pores concentrated within skeletal fragments in bioclastic packstone, 7574.8 ft. **(E)** Epimastoporid algae (arrow) and crinoid (Cr), 7569.2 ft. **(F)** Permocalculus algae (arrow) in bioclastic packstone, 7568.8 ft. 49

Figure 4-19: Photomicrographs and SEM-EDS photos of diagenesis processes in the Wolfcampian succession. **(A)** Quartz grains show line (red arrow) and concave-convex grain contacts (yellow arrow). Clay minerals (C) occlude surrounding pore space. Soft rock fragments (RF) form pseudomatrix, Sterling Fee #6-G, 7665 ft. **(B)** Skeletal grains show tangential to long contact (red arrow), Harwood Trust #2, 7567.8 ft. **(C)** Differential compaction (red arrow) between lithoclast (L) and mud dominated grains, Harwood Trust #2, 7567.8 ft. **(D)** Moldic pores (MP), and dissolution pores (P), Sterling Fee #6-G, 7948.2 ft. **(E)** Partial dissolution of feldspar grain (arrow), plane light, Sterling Fee # 6-G, 7950.9 ft. **(F)** Partial dissolution of feldspar grain (arrow), cross-polarized light, Sterling Fee # 6-G, 7950.9 ft. 54

Figure 4-19: Continued. **(G)** Partial dissolution of rock fragment (arrow), Sterling Fee # 6-G, 7950.9 ft. **(H)** Dissolution within skeletal fragments in bioclastic packstone, Harwood Trust #2, 7574.8 ft. **(I)** Quartz overgrowth (arrow) in sandstone, cross-polarized light, Sterling Fee #6-G, 7917 ft. **(J)** Quartz overgrowth (arrow) in sandstone, plane light, Sterling Fee #6-G, 7917 ft. **(K)** Grain-coating siderite cement (arrow), plane light, Sterling Fee #6-G, 7950.9 ft. **(L)** Grain-coating siderite cement (arrow), plane light, Sterling Fee #6-G, 7950.9 ft. 55

Figure 4-19: Continued. **(M)** Grain-coating siderite cement (arrow) predates calcite cement (Ca), plane light, Sterling Fee #6-G, 7651 ft. **(N)** Grain-coating siderite cement (arrow) predates calcite cement (Ca), cross-polarized light, Sterling Fee #6-G, 7651 ft. **(O)** Isopachous-equant calcite cement (red arrow) pre-dates the blocky calcite cement (Ca) in bioclastic packstone-rudstone, plane light, Harwood Trust #2, 7569.2ft. **(P)** Isopachous-equant calcite cement (red arrow) pre-dates the blocky calcite cement (Ca), cross-polarized light, Harwood Trust #2, 7570 ft. **(R)** Intraparticle pores of fusulinid fragment are filled with mosaic calcite cement, cross-polarized light, Harwood Trust #2, 7570.8 ft. **(S)** Syntaxial overgrowth calcite cementation (red arrow) around echinoid grain, cross-polarized light, Harwood Trust #2, 7592 ft. 56

Figure 4-20: Plots showing correlative relationships between XRD minerology and XRF data. 58

Figure 4-21: XRF-based facies correlation data in Harwood Trust #2 core with core description, GR log, and CGR log. 60

Figure 4-22: XRF-based facies correlation data in Noelke #38 core with core description, GR log, and CGR log. 61
Figure 4-23: Closed up sections from the Harwood Trust #2 core showing the siliciclastic/calcareous cycles with marked cycle tops 63
Figure 4-24: Even cycles caused by gravity-flow deposition from the Harwood Trust #2 core with marked cycle tops. 64
Figure 4-25: Closed up sections from the Noelke #38 core mudrock interval showing the siliciclastic/calcareous cycles with marked cycle tops. 64
Figure 4-26: Plots showing correlative relationships between TOC enrichment and XRF elemental concentration. 67
Figure 4-27: Variation of trace elements, P, Ti/Al, TOC, XRF-based facies interpretation and core description for Harwood Trust #2 core. TOC show positive covariance with redox indicators and productivity indicators (red arrow).....68
Figure 4-28: Variation of trace elements, P, Ti/Al, TOC, XRF-based facies interpretation and core description for Nolke #38 core. In the mudrock interval, TOC show positive covariance with redox indicators and productivity indicators (red arrow). 69
Figure 4-29: Measured core plug porosity and permeability result.....71

Figure 4-30: SEM images for Wolfcampian mudrock pore system. (A) SEM image of organic matter (in black), no organic pore presence, Noelke #38, 6696.4 ft. (B) SEM image of interparticle pores between clay minerals and quartz grains (arrow), Harwood Trust #2, 7697ft. (C) SEM image of interparticle pores, Harwood Trust #2, 7486.6 ft. (D) SEM images of intraparticle pores (circle) and organic pores (arrow), Harwood Trust #2, 7486.6 ft. 73

Introduction

The Permian Basin of West Texas and southeast New Mexico is one of the world's most significant hydrocarbon-producing provinces with mixed siliciclastic-carbonate reservoirs. The Permian Basin is considered to be the most prolific oil-producing basin in the United States (Kim and Ruppel, 2005). It has been producing oil for over 90 years, accounting for 17% of U.S. hydrocarbon production as of 2002 (Dutton, et al., 2005). The Permian Basin covers 52 counties and spans around 86,000 square miles, with estimated United States proved oil reserves of 5 billion bbl (Dutton, et al., 2005). Production has been concentrated on conventional shallow-water carbonate reservoirs during 1960s. With advances in technology such as hydraulic fracturing and horizontal drilling, unconventional oil and gas reservoirs have become an important target for petroleum exploration in the Permian Basin.

The Permian Basin is segmented into two primary sub-basins: the Delaware Basin and the Midland Basin, separated by the Central Basin Platform. In the Midland Basin, the Wolfcamp basinal succession consists of complex deep-water density-flow deposits alternating with more organic-matter (OM) rich hemipelagic sediments (Hamlin and Baumgardner, 2012). The Wolfcampian succession combined with the Spraberry Formation is informally called the *Wolfberry Play*, which is one of the largest unconventional oil plays in the United States, producing approximately 55 million barrels in 2011 (Hamlin and Baumgardner, 2012). The Wolcampian succession is considered to have important unconventional-reservoirs potential for future hydrocarbon production.

STUDY AREA

The study area is located in Glasscock, Sterling, and Irion counties along the nose of Eastern Shelf of the southeast Midland Basin (Figure 1-1).

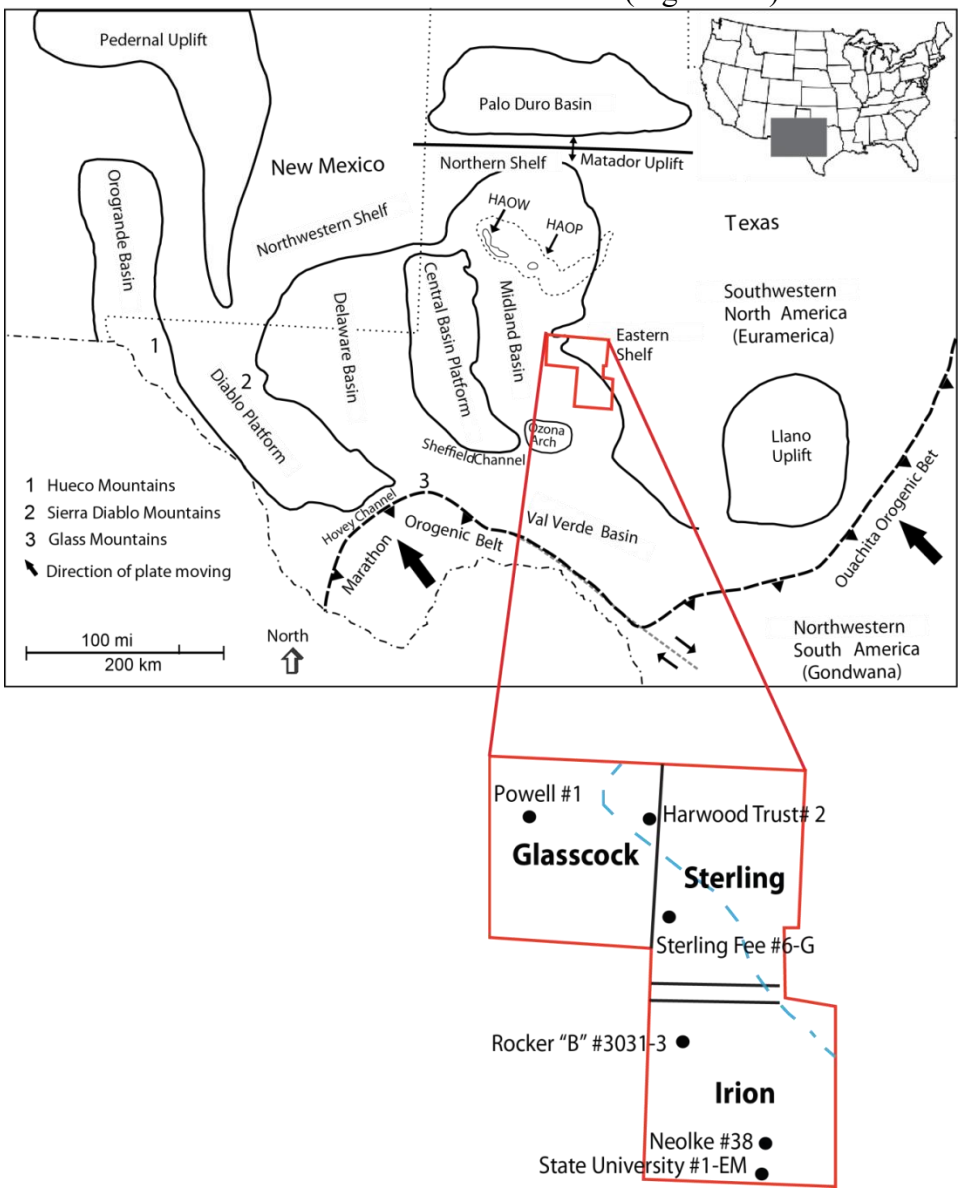

Figure 1-1: Map of the Permian Basin area with major basin structures (from Fu et al., in press). Study area in the red box with core location, and the boundary of the Eastern Shelf is in blue dash line (from Hamlin and Baumgardner, 2012).

PREVIOUS WORK

The earliest attempt to describe Wolfcampian basinal lithofacies in the Midland Basin was made by Cole (1939). Since then, authors began to include Wolfcampian basinal rocks in their studies of platform and shelf facies in the Midland Basin (e.g., Silver and Todd, 1969; Hills, 1972; Cook, 1983). Some studies described the lithofacies, reservoir potential, and depositional setting of platform-derived deep-water allochthonous limestone of Late Pennsylvanian to Early Permian (Wolfcamp) age in the southern and eastern parts of the Midland Basin (e.g., Hobson et al., 1985; Morgan et al., 1996). Mazzullo and Reid (1987, 1989) studied the regional stratigraphy and depositional system of Wolfcamp–Leonard carbonate-shale basinal sections in the northern Midland Basin. A more recent study by Playton and Kerans (2002) examined outcrops to characterize late Wolfcampian slope and toe-of-slope carbonates in the Sierra Diablo. Fu (2015) summarized previous studies on Wolfcamp platform-carbonate and basinal facies, as well as on cyclicity on the eastern Central Basin Platform.

Compared to platform to deep-water carbonate, Wolfcampian fine-grained sediments have less been studied in the Midland Basin. The Hamlin and Baumgardner (2012) study on Wolfcampian–Leonardian basinal successions summarized lithofacies, stratigraphy, and reservoir characterization in the Midland Basin. With the development of instruments such as X-ray fluorescence (XRF) machines, researchers began to apply geochemical data analysis to Wolfcampian basinal mudrock facies. Cortez (2012) studied chemostratigraphy, paleoceanography, and sequence stratigraphy of the Wolfcamp formation in Reagan County of the Midland Basin by using geochemical data. Baumgardner et al. (2016) combined core analysis and geochemical data to characterize Wolfcampian basinal mudrocks and associated facies in the same county. Their study

results inspired this author to integrate petrographic and geochemical data for this research.

Previous studies on Wolfcampian basinal mudrocks have, however, generally been conducted toward the northern or central part of the Midland Basin. Few studies focus specifically on the Wolfcampian deposition near the toe of the Eastern Shelf. Some recent studies focus on reservoir modeling using seismic data interpretation (e.g., Johnston, 2012). But because the slope-to-basinal sediments, especially fine-grained sediments, of the southeast Midland Basin need more-detailed description, this study will focus in detail on the lithofacies, diagenesis process, and reservoir characterization by integrating petrographic and geochemical datasets.

RESEARCH OBJECTIVES

As a mixed-siliciclastic-carbonate depositional system, lithofacies composition in the Wolfcampian succession changes rapidly within meter scale vertically and shows great lateral heterogeneity (Hamlin and Baumgardner, 2012). There is, however, still a significant amount of uncertainty in terms of the integrated description of lithofacies within the study area. By incorporating interpretations of regional depositional setting and stratigraphy from previous studies, the first goal of this study is to investigate lithofacies variation and diagenesis processes, and to interpret depositional processes in the less-studied southeast Midland Basin.

The development of fine-sediment-related technology, such as X-ray Fluorescence (XRF) data, allows us to better understand the sedimentation record within mudrocks, including the detailed geochemical and depositional composition of the mudrock system of this area and its contribution to hydrocarbon production. The second

objective of this study is to gain a detailed understanding of the mineral and chemical composition in Wolfcampian mudrock intervals, their indications of paleoenvironment change, and their relations with reservoir potential. Findings in this study will demonstrate the importance of integrating petrographic and geochemical analysis into studies on Wolfcampian mudrocks intervals.

Because the Wolfcampian succession is considered to have important unconventional-reservoirs potential for future hydrocarbon production in the Midland Basin, the third objective of this study is to evaluate Wolfcampian-succession reservoir potential based on lithofacies variation, influences from diagenesis processes, and geochemical results. The results of this study will help future hydrocarbon exploration in the Midland Basin.

Geological Setting

REGIONAL TECTONISM

The Permian Basin region was deformed and segmented as a consequence of the late Paleozoic Marathon-Ouachita orogeny of the Marathon-Ouachita foreland bordering the southern margin of the North American Craton (Figure 1-1; Ross and Ross, 1987; Poole, et al., 2005). The Marathon-Ouachita orogeny is the local reflection of continental collision of Gondwana and Laurussia, which began in the Mississippian and continued into the Pennsylvanian and Permian (Blakey, 2003). The Permian Basin region experienced intricate faulting, followed by differential subsidence. The structural outcomes from Pennsylvanian to Early Permian include formation of the Midland and Delaware foreland Basins, along with structural high platforms such as the Central Basin Platform, the Diablo Platform, and the Ozona Arch (Ball, 1995; Frenzel et, al., 1998; Hills, 1984).

The Midland Basin experienced tectonically driven subsidence during the Wolfcampian followed by sediment infill from mid- to late-Permian while the Central Basin Platform continued to rise, or subside more slowly, separating the Midland and the Delaware Basins (Ewing, 1993; Horak, 1985). Tectonic activity in this region decreased greatly following the Early Permian, and came to an end around mid-Permian (Ewing, 1993).

STRATIGRAPHY AND PALEOGEOGRAPHY

The term Wolfcamp was first used in Udden et al. (1916) referring the lowermost Permian strata of the Glass Mountains. The "Wolfcamp Formation" referring to the first series of the Permian System has been accepted into the North American Stratigraphic Code (NASC) and has been used by both academia and industry since 1939 (Adams et, al, 1939). For industry purpose, the interval between the base of the Leonardian Dean sandstone and the underlying Strawn limestone had been referred as the Wolfcamp shale and divided them into Wolfcamp A, B, C, and D. But when correlating this nomenclature with North America chronostratigraphic nomenclature during Wolfcampian and lower Loenardian ages, the result could not coincide completely. Based on fusulinid biostratigraphy by Wilde (1975), Mazzullo and Reid (1987) and others, the intervals of Wolfcamp B and C coincide with the actual Wolfcampian strata (Figure 2-1; Baumgardner et al., 2016).

During the Wolfcampian, the Permian region was located in the tropical to subtropical zone slightly north to the equator (Figure 2-2; Ross and Ross, 1990; Walker et al., 1995; Golonka et al., 1994). During the Early Permian (Wolfcampian and Leonardian) time, carbonate debris and siliciclastics were shed from the Eastern Shelf and deposited in the Midland Basin.

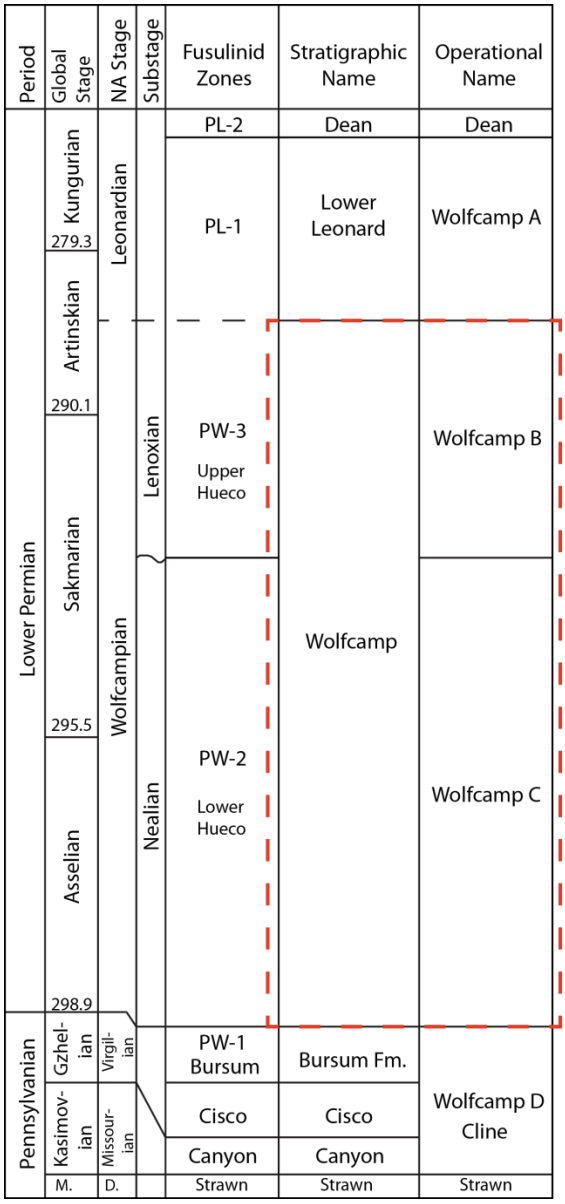

Figure 2-1: Stratigraphic and operational names used in oil industry of formations in the Midland Basin (Modified from Baumgardner et. al, 2016).

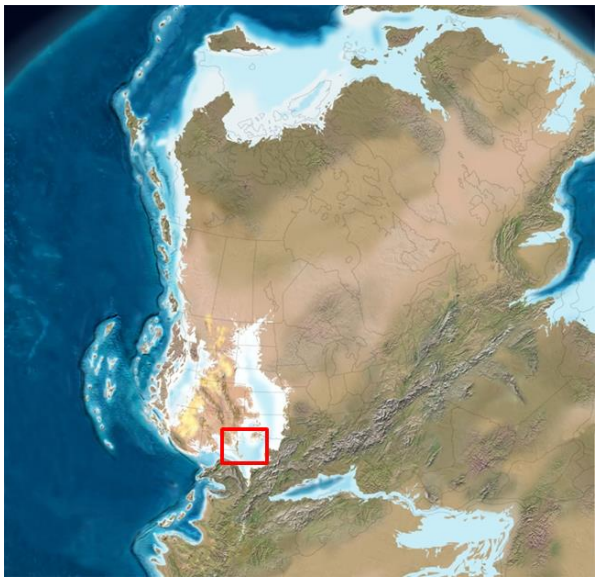

Figure 2-2: North American paleogeographic map of in Early Permian, ca. 290 Ma, highlighting the Permian Basin region (From Blakey, 2017).

GLACIATION AND EUSTASY

Late Paleozoic glaciation across Gondwana has been identified for over 100 years, and it has significant implications for Late Paleozoic sea level and climate interpretation (Ross and Ross, 1988; Fielding et al., 2008a; Holterhoff, 2010). Fielding et al. (2008b) identified four Carboniferous and four Permian glacial intervals in eastern Australia separated by intervals (several million years in duration) with no evidence of glaciation (Figure 2-3). The earliest Permian (Asselian and early Sakmarian stage) experienced Late Paleozoic's most intense icehouse climate condition, which generated composite glacial-eustatic signal in regions like the Permian Basin (Figure 2-3; Fielding et al., 2008a; Holterhoff, 2010). Ross and Ross (1987) noted that the relatively short-term

sea-level changes (Figure 2-4) which associated with third-order depositional sequences during Lower Permian were caused by glaciation.

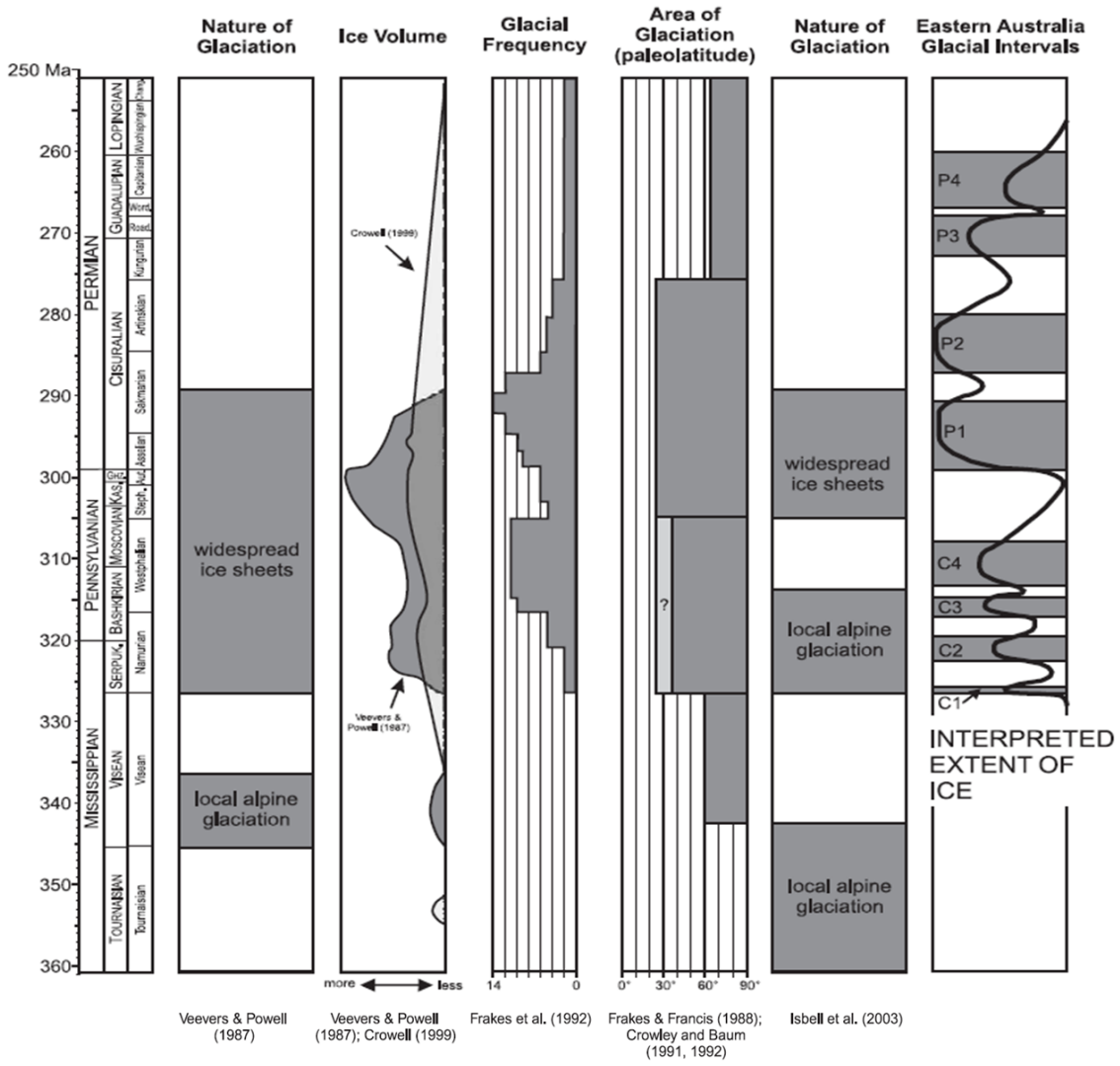

Figure 2-3: Timing, duration, and character of the late Paleozoic Ice Age (Veevers & Powell 1987; Frakes & Francis 1988; Crowley & Baum 1991, 1992; Frakes et al. 1992; Crowell 1999; Isbell et al. 200) and recognized glacial intervals (from Fielding et al., 2008b).

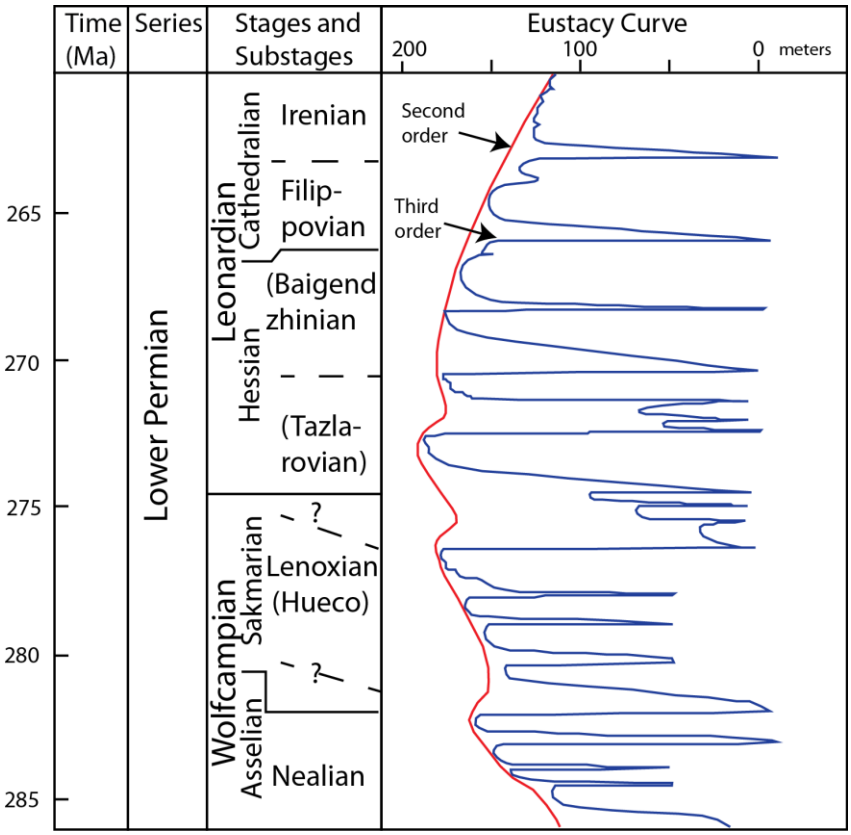

Figure 2-4: Stratigraphic intervals and corresponding eustacy curve in Lower Permian (Modified from Ross and Ross, 1987).

The Eastern Shelf of the Midland Basin has a great influence on Midland Basin basinal sedimentation (Hamlin and Baumgardner, 2012). The Early Permian high-amplitude and high-frequency sea-level fluctuation has been well documented on the Eastern Shelf. Brown et al. (1987, 1990) identified 16 major and several minor depositional sequences in Virgilian to Wolfcampian Series, principally highstand progradational terrigenous clastic subsequences followed by transgressive limestone subsequences, responding to Late Pennsylvanian and Early Permian regressive-

transgressive episodes on the Eastern Shelf. Regional sequence stratigraphic studies on the Eastern Shelf have identified between six to eight 3rd-order sequences in the Wolfcampian section (Morgan et al., 1996; Flamm, 2008). Hentz et al. (2016) mapped 14 series of upper Pennsylvanian and lower Permian mix-siliciclastic-carbonate deposit from the Eastern Shelf into the Southern Midland Basin though wireline log correlation.

Methods and Dataset

Core descriptions were coupled with thin-section observations and SEM and XRD analysis for lithofacies and diagenesis descriptions. Observations were coupled with XRF data for mineralogical facies stacking, especially focusing on mudstone facies. Lithofacies and XRF data were integrated to characterize depositional cyclicity and interpret depositional environment and process. Pore networks for mudrock facies were studied based on data from thin sections and high-resolution SEM images. Sandstone porosity and permeability were analyzed through core plugs. Petrographic data along with TOC analysis help characterize the reservoir potential of the Wolfcampian succession.

PETROGRAPHIC OBSERVATION

Core Description

Six cores (Table 1) from Glasscock, Sterling, and Irion Counties, totaling 667 ft, were logged at a scale of 1 inch:1 foot and photographed. These cores are stored at the Bureau of Economic Geology (BEG) Core Research Center (CRC) in Austin, TX. These cores only cover a portion of the Wolfcampian succession. They were divided into two categories: a siliciclastic-dominated interval which presents in cores from the Irion and Sterling Counties, and a calcareous-dominated interval which presents in cores from Glasscock County.

API Number	County	Operator	Lease name	Surface Latitude	Surface Longitude
42235322460000	IRION	INDIAN WELLs OIL CO	ROCKER "B" #3031-3	31.41888	-101.17336
42235317840000	IRION	EXXON CORPORATION	STATE UNIVERSITY #1-EM	31.0869056	-100.9065683
42235102290000	IRION	ARCO	NOELKE #38	31.1778863	-100.8946605
42173309790000	GLASSCOCK	LINGEN EXPLORATION	HARWOOD TRUST #2	31.9562564	-101.2947335
42173302580000	GLASSCOCK	PAN AMERICAN	POWELL E.L #1	31.9420072	-101.6601901
42431314200000	STERLING	TEXACO INCORPORATED	STERLING FEE #6-G	31.7205044	-101.2128181

Table 3-1: Table of cored wells, located in Figure 1.

The author use the sandstone classification of Folk (1965) and the carbonate classification of Dunham (1962). Mudrock classification follows that of Lazar et al. (2015). Mudrocks in this study refer to sedimentary rocks with a dominant grain size of less than 62.5 micron (Loucks et al., 2009). Bedding thickness, lithology, sedimentary structures, grain size, and fossil assemblages were recorded. Core descriptions are presented in the Appendix. These descriptions were refined by correlating macroscopic with microscopic observations and geochemical data.

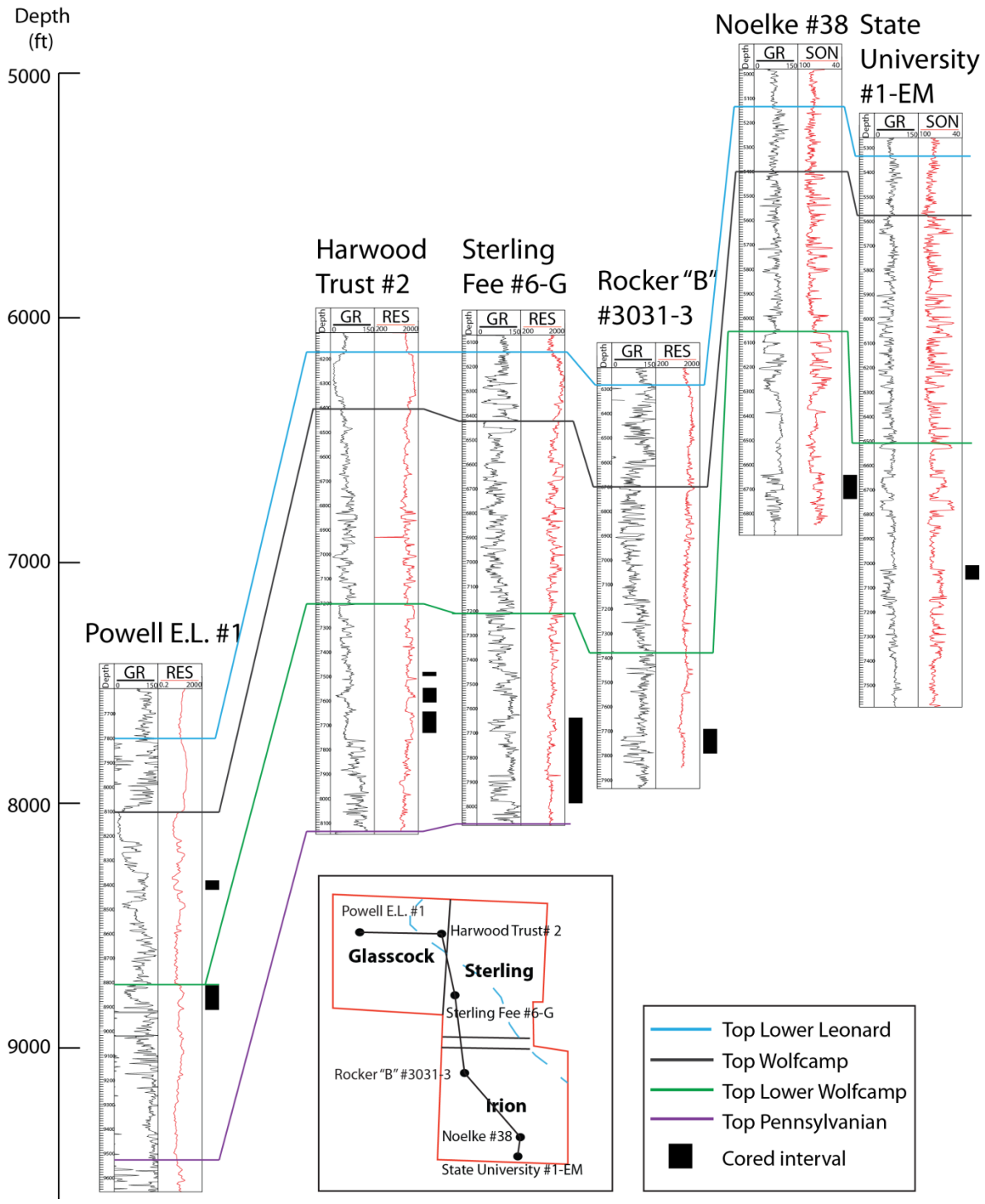

Figure 3-1: Northwest to southeast cross section displaying core positions and stratigraphic units.

Thin Sections Analysis

In total, 103 samples were taken from the six cores, representing various identified lithofacies for thin sections prepared at TPS Enterprises LLC, Houston, TX. The thin sections were epoxy impregnated. Thin sections of carbonate samples were half stained with mixed Alizarin red/potassium ferricyanide, and thin sections for mudrocks were polished for detailed structural observation (information provided by TPS Enterprises LLC). Thin sections were examined using a ZEISS Microscope Axioskop 40 at the Jackson School of Geosciences. Microscope images were acquired with a SONY NEX-VG10 camera.

SEM Analysis

SEM images were acquired in order to conduct a detailed study on mudrock porosity and mineral components. Eight rock chips were selected for SEM observation from Noelke #38, Harwood Trust #2, Powell E.L #1, and Sterling Fee #6-G core. Samples were then re-cut into around 9mm*9mm*2mm cubes, and milled by Argon-Ion miller. The milling process was conducted by Leica EM TIC020 Triple Ion Beam Miller under current of 2.8 mA and 8KV accelerating voltage for 2-3 hours at BEG CRC. Argon-ion-milled surfaces prove to be the best for porosity examinations (Loucks et al., 2009). Samples were then coated by iridium in Leica EM ACE600 Coater. This process eliminates charging and prevents specimen damage by reducing heat, which enhances the resolution for SEM observation (personal talk with SEM research scientist Patrick Smith at BEG).

After sample preparation, sample minerology, pore type, presence of organic content were observed under FEI Nova NanoSEM 430 at BEG imaging backscattered

electron (BSE) and secondary electron (SE) images. Elemental analysis using the attached energy dispersive spectroscopy (EDS) was used to help with mineral identification.

CORE PLUGS ANALYSIS

Based on lithofacies description, 62 core plugs were taken from the Rocker "B" #3031-3, Noelke #38, Harwood Trust #2, and Sterling Fee #6-G core at BEG CRC for porosity and permeability analyses at Weatherford Laboratories, Midland TX. Porosity was measured using Helium at ambient conditions in a Boyle's Law Porosimeter. The measurement on permeability used Darcy's Law at 400 psi Net Confining Stress in a Hassler Sleeve Permeameter.

CHEMOSTRATIGRAPHIC DATA

XRF Analysis

Over 1500 XRF measurements were carried out in two cores. A 2-inch sampling interval was used for major elements in the Harwood Trust #2 core. A 4-inch interval was used for trace elements in the Harwood Trust #2 core, and for both major and trace elements in the Noelke #38 core because of timing constraints. The XRF measurement provides an instant, quantitative, non-destructive understanding for core elemental composition (Rowe, 2012).

High-resolution energy dispersive XRF data were generated by a Bruker Tracer III (T3S2270) for major elements and a Bruker Tracer IV (T4S2602) for trace elements. The XRF spectra for major elements were generated under vacuum using an Rh tube set

at 15 kV and 34.4 μA. The XRF spectra for trace elements were analyzed in air at 40 kV and 25 μA, with an Al-Ti-Cu filter (information provided by Premier Oilfield Laboratories). The cores were washed and scrubbed to remove surface contamination before scanning. A flat, dry core surface was put on a 3mm*4mm elliptical scanning window of the XRF spectrometer. A laptop is connected to the XRF spectrometer to control the scanning process. For quality control, a standard pellet, limestone for major spectrometer and shale pellet for trace spectrometer, was scanned three times at a 180s count time every day before sample scanning. Each sample points were scanned by major and trace XRF spectrometer for both a 60s count time. Core scanning was finished in BEG CRC by the author and staff from Premier Oilfield Laboratories, Houston, TX. Due to overlaps in elemental fluorescence peaks and other effects such as absorption and secondary fluorescence, inter-element corrections must be made. Thus raw data were then calibrated at Premier Oilfield Laboratories to quantify mudrock matrices elemental composition. After the calibration, the compositions of 29 elements are reported in terms of percentage. The major elements include: Na, Mg, Al, Si, P, S, K, Ca, Ti, Mn, and Fe in weight percent, and Ba, V, and Cr in part per million (ppm). Trace elements include: Co, Ni, Cu, Zn, Ga, As, Pb, Se, Th, Rb, U, Sr, Y, Zr, Nb, and Mo in ppm.

Elemental abundances of U, Th, and K can be used to calculate an equivalent spectral Gamma Ray (SGR) curves through the formula,

$$(U * 8) + (Th * 4) + (K * 16) = SGR$$

where U is uranium content in parts per million (ppm), Th, is thorium content in (ppm), and K is in weight percent content of potassium (Doveton and Merriam, 2004). Computed Gamma Ray (CGR) curves can be calculated from adding Th and K content. By omitting the disruptive influence of uranium, CGR curves are able to provide a better

match the clay minerals changes (Doveton and Merriam, 2004; Dr. Stephen C Ruppel at BEG, personal communication).

XRD and TOC analysis

Based on the preliminary results from XRF analysis, 48 sample powders were drilled at selected XRF measurement points. The powders were used for both XRD and TOC evaluation at Premier Oilfield Laboratories, Houston, TX. XRD data contains compositions of major rock forming minerals such as quartz, calcite, and clay. Mineralogical results were compared with XRF elemental data to evaluate the accuracy of XRF results, which helped minerology prediction using XRF data for sample points without XRD data. The integration of XRD and XRF analysis provided the understanding of the variation in depositional environments. TOC data were used to quantify the organic richness of the core.

Results

LITHOFACIES AND INTERPRETED DEPOSITIONAL ENVIRONMENT

In this study, stratigraphic intervals present in the core are mostly in Wolfcamp C (Figure 3-1). Based on core and microscopic observation, seven total lithofacies in the Wolfcampian succession, three siliciclastic-dominated and four carbonate-dominated, were defined based on sedimentary features, grain size, texture, mineral composition, and bioclasts. The lithofacies include (1) sandy siltstone, (2) argillaceous mudstone, and (3) very fine to fine sandstone as siliciclastic-dominated lithofacies; and (4) Massive to Weakly Laminated calcareous mudstone, (5) Laminated calcareous mudstone, (6) mud-dominated bioclastic packstone/rudstone, and (7) grain-dominated bioclastic packstone-grainstone/rudstone as calcareous-dominated lithofacies (Table 2). Mudstone facies in this study were defined based on mineral composition discussed in Lazar et al. (2015) (Figure 4-1).

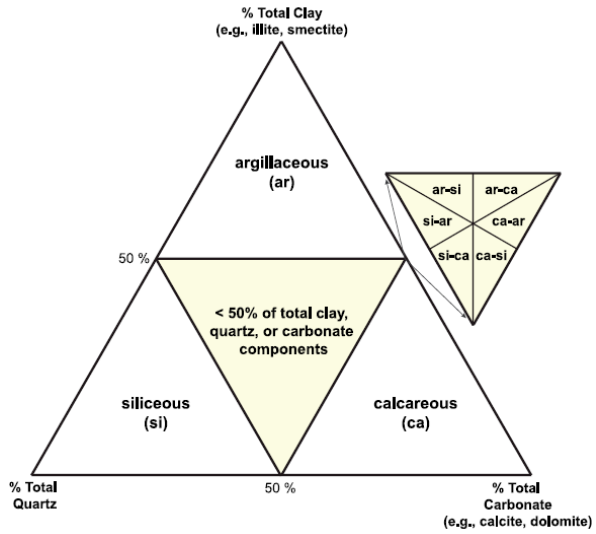

Figure 4-1: Mudstone nomenclature diagram based on mineral composition (from Lazar et al., 2015). Si= siliceous, ca=calcareous, Ar= argillaceous

Lithology	Lithofacies	Composition	Bed thickness	Sedimentary structures	Accessories	Primary depositional mechanism
Mudrock	Sandy Siltstone	Dominated by silt- to very fine sand-size quartz grains. With organic matter, clay minerals. Some are laminated with fine sandstone beds (centimeter scale)	1 cm to 4 ft	Massive	Fissile, ripped-up mud clast locally, bioturbation, average TOC= 1.1 wt.%	Debris flow
	Argillaceous Mudstone	Dominated by clay minerals, with some silt-sized quartz grains and organic matters	2 inch to 4 ft	Massive, weak lamination locally	Pyrite framboids, bioturbation, average TOC= 1.5 wt.%	Hemipelagic settling
	Massive to Weakly Laminated calcareous mudstone	Silt-sized grains, dominated by carbonate mud. With organic matters	5 inch to 3 ft	Massive to weakly laminated	Pyrite framboids, dolomite minerals, average TOC= 1.5 wt.%	Hemipelagic settling
	Laminated Calcareous Mudstone	Silt- to very fine sand-sized grains, dominated by carbonate mud. With organic matters, skeletal fragments	Few millimeters to 1 cm	Laminated	average TOC= 1.3 wt.%	Diluted turbidity current

Table 4-1: Summary of Wolfcampian succession lithofacies and interpreted depositional process.

Sandstone	Very fine to Fine Sandstone	Very fine- to fine-sized grains, dominated by quartz and rock fragments	Few inches to 10 ft	Incomplete Bouma sequences, normal grading, erosional contact	Ripped-up clay clasts, burrow, soft sediment deformation	Turbidity flow
Carbonate	Mud-dominated Bioclastic packstone/Rudstone	Clasts: skeletal fragments, algal fragments, and lithoclasts Matrix: clay-sized carbonate mud	Few inches to 1 ft	Bioclast in fine-grained matrix, clast- to matrix-dominated	Rare, soft sediment deformation	Debris flow
	Grain-dominated Bioclastic Packstone-Grainstone/Rudstone	Clasts: skeletal fragments, algal fragments, peloid, and lithoclasts Highly cemented	18 ft	Normal grading, concentrated fusulinid fragments, grain-dominated	Rare, highly cemented, mud stripes, visible pores on core,	Hyperconcentrated density flow

Table 4-1 (continued)

Sandy Siltstone

Sandy siltstone is characterized by dark-gray to black intervals interbedded with sandstone in core. The color becomes lighter as grain size increases. Bed thickness ranges from 1 cm up to 4 ft. It mostly shows massive structure, but ripped-up clast and weak lamination are present locally (Figure 4-2A). Soft sediment deformation is present locally (Figure 4-2D). Sandy siltstone is commonly topped by sandstone with a scouring surface (Figure 4-2E). It usually laminates with very fine to fine sandstone at a centimeter scale, and is characterized in cores by dark-gray to black beds interbedded with light-gray beds. The lamination usually has a wavy shape (Figure 4-2B). In some places, laminations are inclined at a steep angle around 25 degrees (Figure 4-2C).

Under the microscope, sandy siltstone is dominated by quartz grains and clay-sized fine sediments. The quartz grains are silt-sized to very fine sand-sized, ranging from 30 to 120 microns (Figure 4-3A, B). Quartz grains are poorly sorted with angular to sub-angular shape (Figure 4-3C, D). Different mineral composition of laminated sandy siltstone and very fine to fine sandstone is clearly shown in the thin sections (Figure 4-3E). The sandstone laminae are dominated by silt-sized to very fine sand-sized quartz with minor feldspar (less than 5% through eye estimation). The quartz grains are poorly sorted, ranging from 60 to 200 microns, and are sub-angular to sub-rounded shape (Figure 4-3F).

XRD results show that quartz accounts for an average of 42.6 weight percent (wt.%) of the sandy siliceous mudstone (N=6). Within the three dominant components (quartz, clay, and carbonate), quartz accounts for 54.2 average weight percent (N=6). Total clay minerals (illite, chlorite, montmorillonite, and kaolinite) account for 39.7 wt.% on average, while carbonate minerals (calcite, siderite, and minor dolomite) only account

for an average of 6.1 wt.% (N=6). Sandy siltstone has fair to good richness of organic matter (Peters, 1986), with an average TOC value of 1.1 wt.% (N=6).

Quartz grains in sandy siltstone are mostly in angular shape, sand to silt size, and are poorly sorted. This is more common in debris flow deposits compared to turbidity flow deposits (Mulder and Alexander, 2001). Large clay clast distribute chaotically within the matrix-supported sediment observed in core is another common character for debris flow deposits (Mulder and Alexander, 2001). Thus, in a deep-water depositional setting, the sandy siltstone is interpreted to be deposited through debris flow. Another evidence of debris flow deposit is that sandy siltstone does not show vertical grading or sedimentary structure. The presence of organic matter shown by XRD data indicates that sandy siltstone is deposit under a relative anoxic environment.

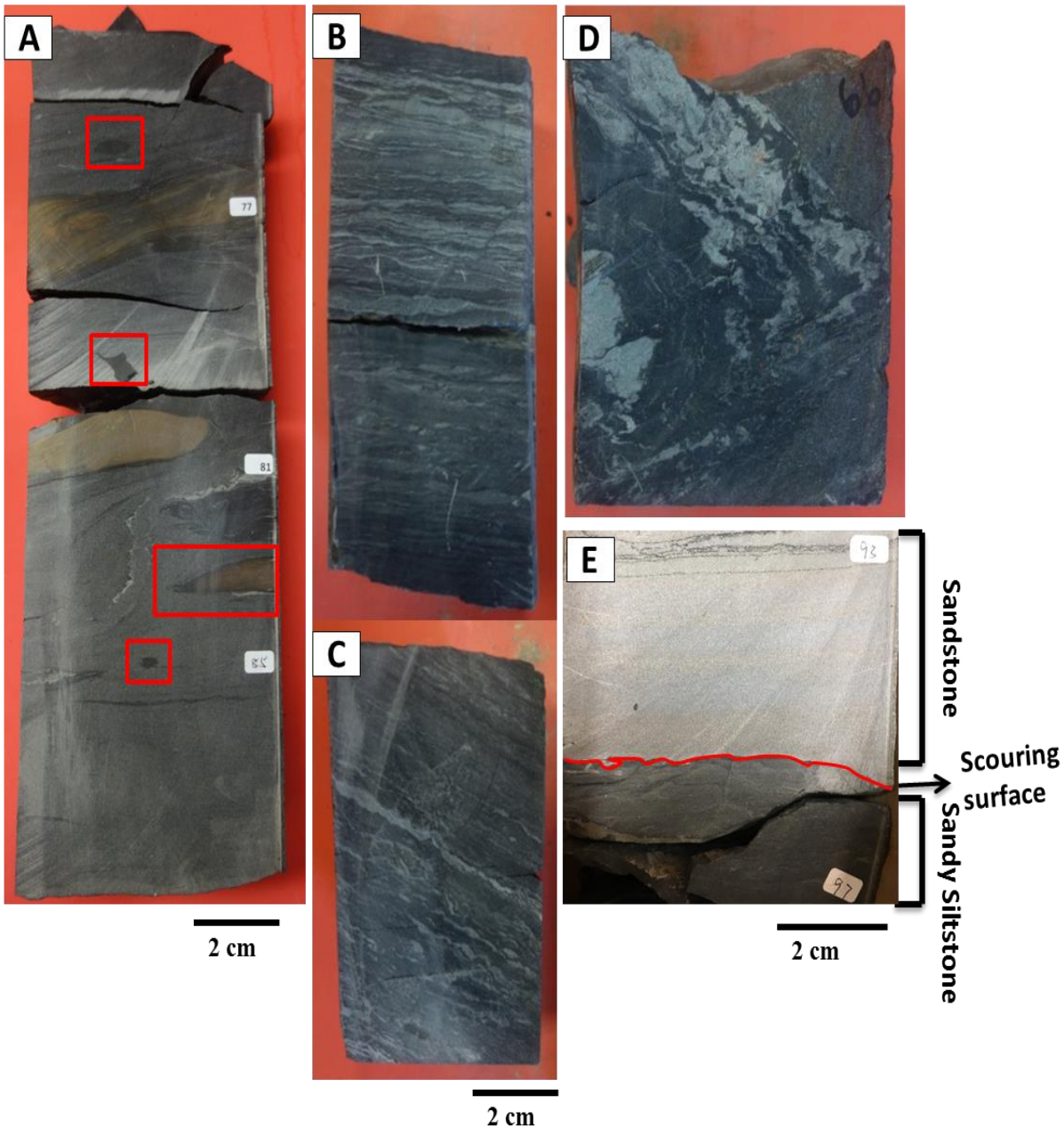

Figure 4-2: (A) Slabbed core photo of sandy siltstone with ripped up clasts (in the red box), Noelke #38, 6702.8-6703.4 ft. (B) Wavy lamination, Rocker "B" #3031-3, 7765.1 ft. (C) Inclined wavy lamination, State University #1-EM, 7062 ft. (D) Soft sediment deformation present locally, State University #1-EM, 7066 ft. (E) Sandy siltstone topped by fine to very fine sandstone facies with scouring surface, Noelke #38, 6671-6672 ft.

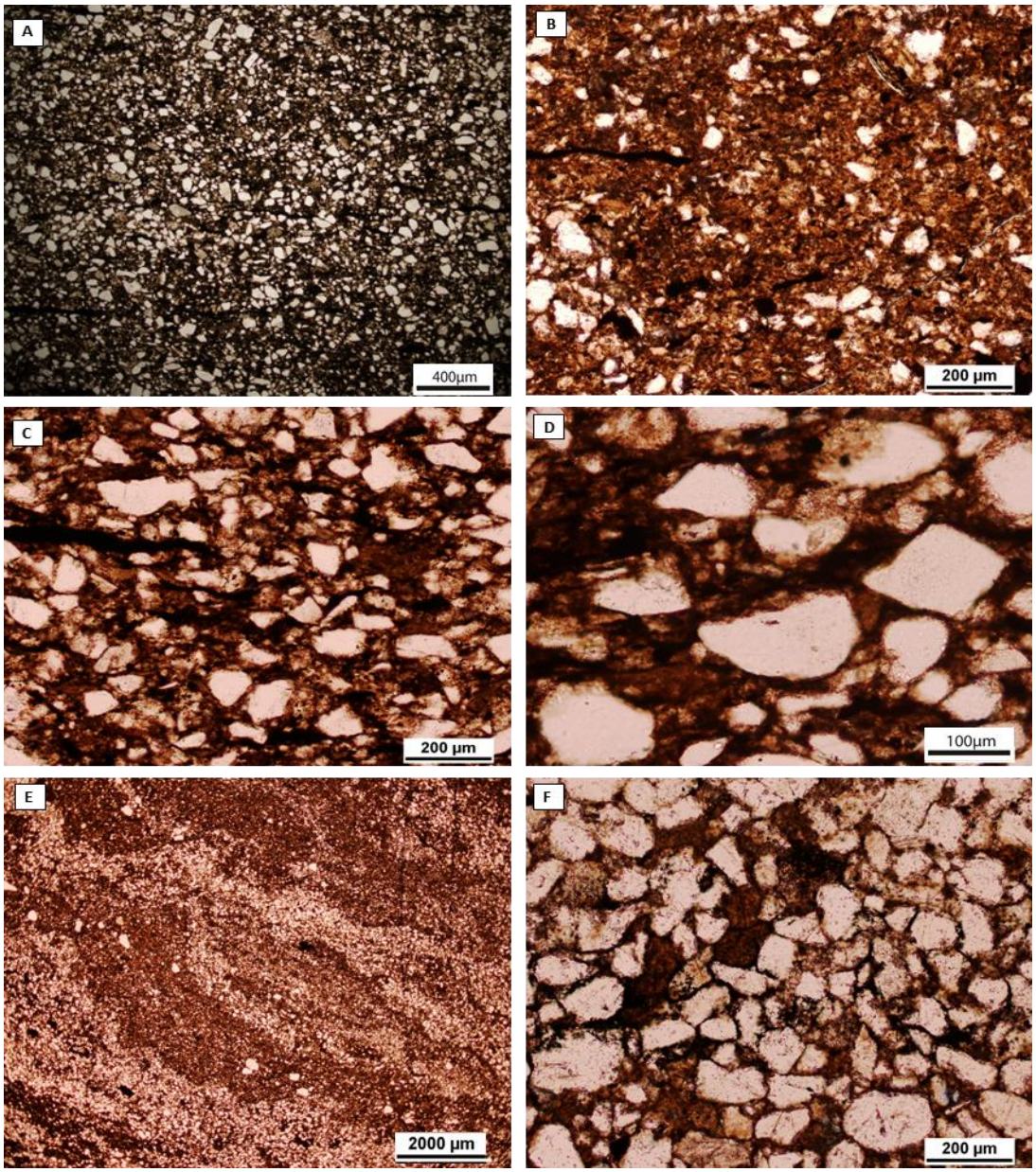

Figure 4-3: Photomicrographs of sandy siltstone: (A)(B) Mineral composition is dominated by quartz grains and clay-sized sediments, Noelke #38, 6696.4 ft, State University #1-EM, 7063.9 ft. (C) Quartz gains are poorly sorted, angular to sub-angular shape. (D) Quartz grains can rich up to 120 micron. (E)Sandy siltstone laminate with very fine sandstone, Sterling Fee #6-G, 7642.5 ft, State University #1-EM, 7063.9 ft. (F) Quartz grains in sand laminae are poorly sorted, sub-angular to sub-rounded shape, very-fine sandstone size, State University #1-EM, 7063.9 ft.

Argillaceous Mudstone

Argillaceous mudstone is characterized by massive dark-gray to black beds ranging from 3 inches to 14 ft. It mostly shows massive structure, but some have minor lamination (~1 mm). Compared to siliceous mudstone, argillaceous mudstone is very fissile and usually broken (Figure 4-4). It commonly overlies massive siliceous mudstone and is topped by sandstone beds.

Argillaceous mudstone differs from sandy siliceous mudstone lithofacies by its high percentage of clay content. Total clay minerals (illite, chlorite, montmorillonite and kaolinite) account for an average of 48 weight percent of the argillaceous mudstone (N=13). Within the three dominant components (quartz, clay, and carbonate), total clay minerals account for 62.4 wt.% on average (N=13). Quartz accounts for 31.4 wt.% on average (N=13). While carbonate (calcite, siderite, and minor dolomite) accounts for 6.2 wt.% on average (N=13). Argillaceous mudstone is enriched in organic matter compared to siliceous mudstone with a slightly higher average TOC value of 1.5 wt.% (N=13).

Under the microscope, argillaceous mudstone is composed mostly of fine-grained sediments with minor quartz grains (Figure 4-5). Quartz grains are silt-sized (Figure 4-5A).

SEM images show that the dominant the clay mineral is illite. Illite averages 34.5 wt.% (N=13) among the total clay minerals according to XRD results. Clay minerals, especially illite, show directional alignment, which indicates compaction (Figure 4-6). Abundant organic matters are present between clay minerals (Figure 4-6).

Argillaceous mudstone is interpreted to deposit in a low-energy, anoxic environment, with evidence, based on SEM observation and TOC result, of very fine grain sediment and the presence of abundant organic matter. Silt-sized, fine grain

sediments are interpreted to deposit through hemipelagic settling, with evidence of rarity of current-generated sedimentary structure and fine grain size dominated by clay-sized sediments (Stow and Piper, 1984).

Figure 4-4: Slabbed core photo of argillaceous mudstone, broken, minor lamination locally, Noelke #38, 6681-6690 ft.

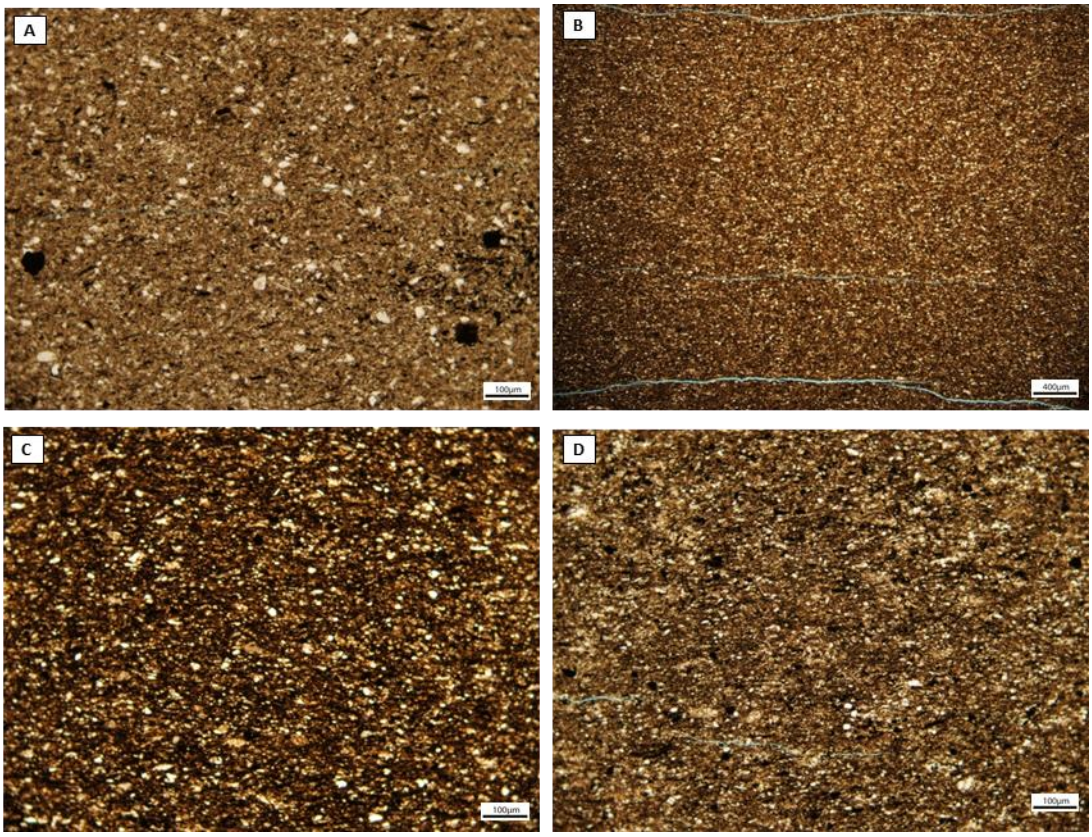

Figure 4-5: Photomicrographs of argillaceous mudstone. (A) Argillaceous mudstone, clay mineral dominated, with minor quartz grains. Pyrite is sparsely present. Sterling Fee #6-G, 7706.9 ft. (B), (C) and (D) Argillaceous mudstone in Powell E.L #1, 8841 ft.

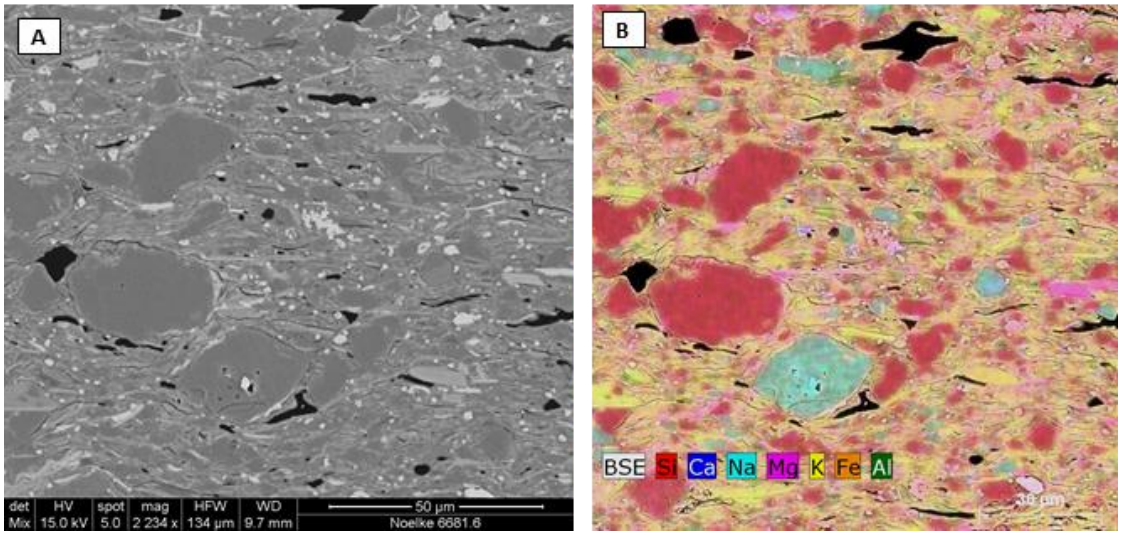

Figure 4-6: (A) SEM images of Noelke #38, 6681.6 ft. (B) SEM-EDS images. Quartz grains (in red) are sub-angular to sub-rounded shape. Directional alignment of clay minerals (mixture of yellow and green) indicates compaction. Albite presents locally (in blue). Abundant organic matters (in black) present, Noelke #38, 6681.6 ft.

Very Fine to Fine Sandstone

Very fine to fine sandstone is characterized in core by light gray- to brown-colored beds ranging from a few inches to 10 ft. The sandstone shows a variety of sedimentary structures in cores. Normal grading presents locally at the base of the sandstone bed. An overall fining-upward trend is commonly seen throughout the study cores, which display incomplete Bouma sequences (Bouma, 1962). For example, thin-bedded, massive sandstone is commonly capped by a thin mudstone layer (Bouma Td and/or Te divisions), commonly with an erosional contact (Figure 4-7A, C, F). Another example of finning-upward trend is that the massive, structureless (Bouma Ta division) sandstone is topped by sandstone with planar lamination (Bouma Tb division) (Figure 4-

7A). Ripple lamination (Bouma Tc division) is present after multiple centimeter-scale upward-fining sequences (Figure 4-7B). Soft sediment deformation such as flame structure and load structure is present locally at the contact between sandstone and mudstone (Figure 4-7E). Ripped-up clay clast and mud clast ranging from millimeter to centimeter scale is common in fine-grained sandstone (Figure 4-7D). Fluid escape structure is common, especially in Noelke #38 core (Figure 4-7F). It lacks the evidence of burrow.

Under the microscope, the sandstone is dominated by quartz grain (> 75% through eye estimate) (Figure 4-8E, F). Rock fragments are present in small amounts (12% through eye estimate), and feldspar is rarely present (3% through eye estimate). The mineral composition puts the sandstone into the sublitharenite category according to the Folk classification of sandstone (Folk, 1965). Quartz grains are sub-angular to sub-rounded in shape and have line contact with each other (Figure 4-8D). Quartz grain size ranges from 30 to 250 microns, and grains are medium sorted (Figure 4-8).

Soft sediment deformation such as flame structure and fluid escape structure present in very fine to fine sandstone indicate rapid deposition, which are common in deep water basins with turbidity currents (RL, 1982; Mulder and Alexander, 2001). The thin-bedded sandstones commonly display incomplete Bouma sequences, which is a strong evidence of turbidity current deposits (Bouma, 1962). In the context of a deep-water depositional setting, the very fine to fine sandstone is deposited by turbidity current (Bouma, 1962; Mulder and Alexander, 2001).

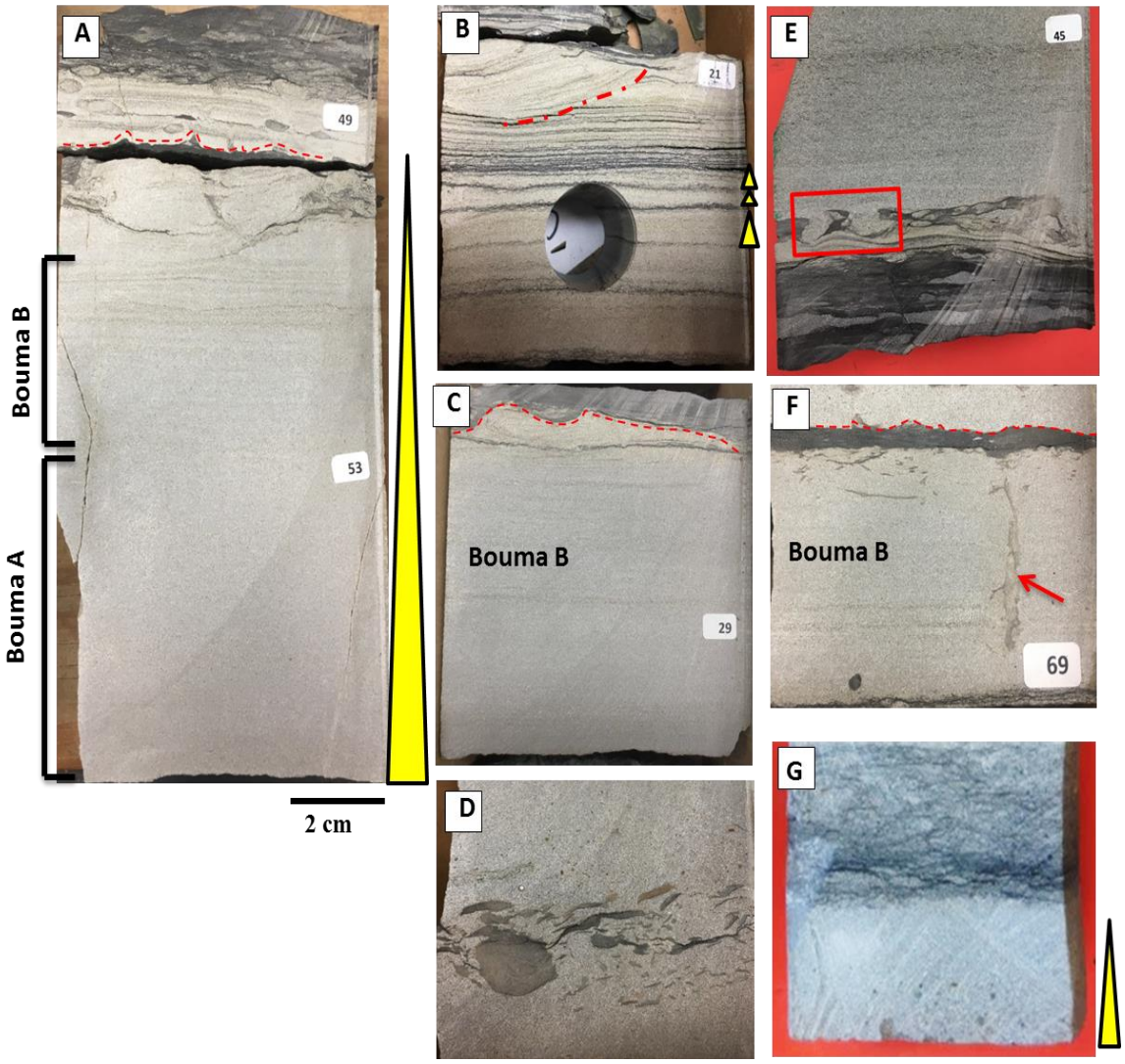

Figure 4-7: Slabbed core photo of very fine to fine sandstone. (A) Sandstone beds show overall fining upward trend from massive bed (Bouma A) to bed with planar lamination (Bouma B). Flame structure (dash line). Noelke #38, 6712-6712.6 ft. (B) Multiple finning upward sequences followed by ripple lamination (dash line) at the top, Noelke #38, 6739-6740 ft. (C) Planar laminated sandstone topped by mudstone. Soft sediment deformation at the contact (dash line), Noelke #38, 6665.5. (D) Massive sandstone with ripped-up clay clast, Noelke #38, 6672.9 ft. (E) Load structure (red box) present at the base of planar laminated sandstone, which overlies mudstone. (F) Fluid escape structure (red arrow) cutting through planar laminated sandstone. Flame structure (dash line). Noelke #38, 6713.8 ft. (G) Normal grading, Rocker "B" #3031-3, 7730 ft.

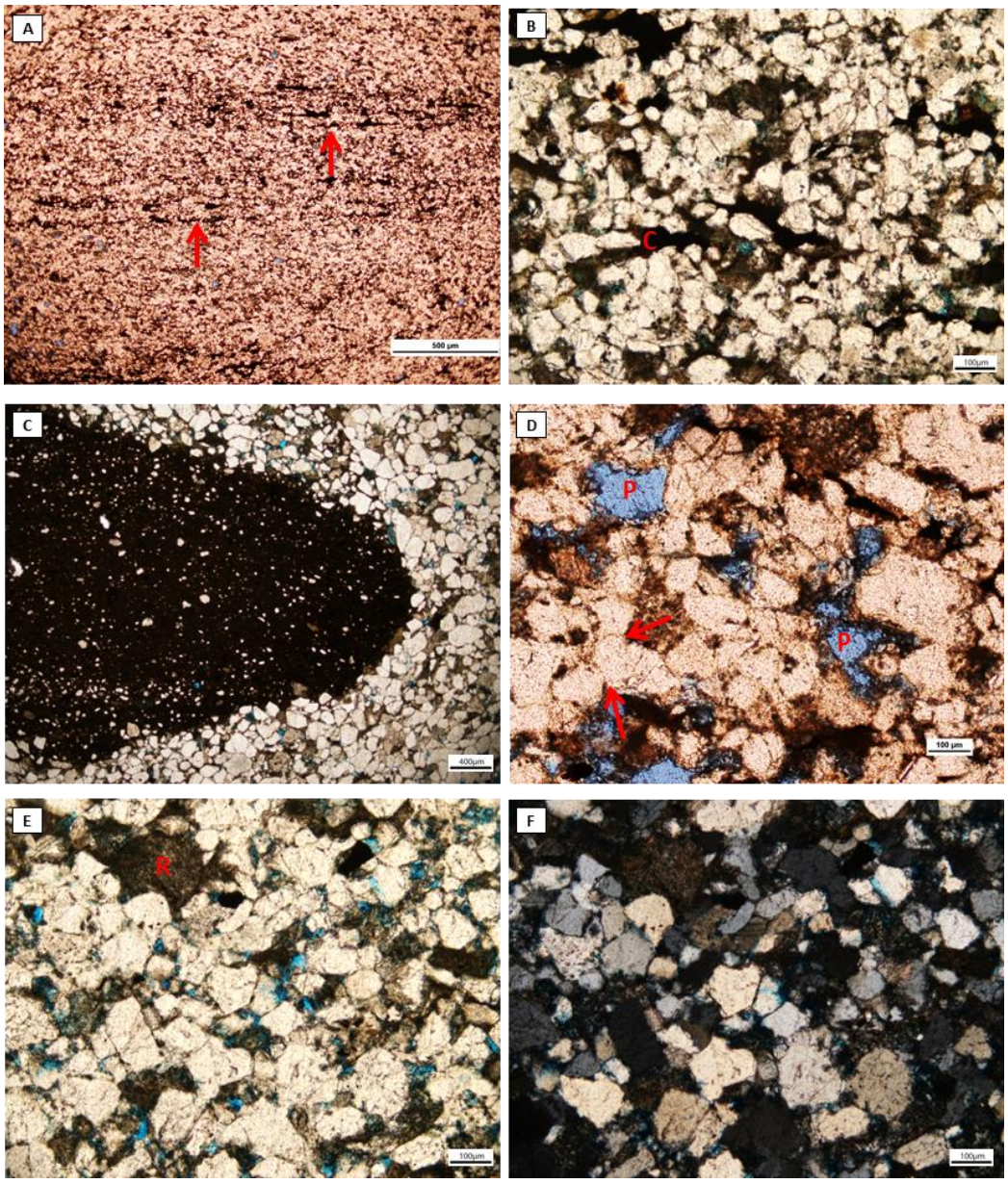

Figure 4-8: Photomicrographs of very fine to fine sandstone. **(A)** Sandstone with mud stripes (red arrow), State University #1-EM, 7057.6 ft. **(B)** A zoom in view of sandstone with mud stripe, clay minerals (c) in the muddy stripe occlude the pore space, Noelke #38, 6721.8 ft. **(C)** Sandstone with big mud clast (to the left), Sterling Fee #6-G, 7689.2 ft. **(D)** Quartz grains have long contact (red arrow). Presence of dissolution pore (P), Sterling Fee #6-G, 7948.2 ft. **(E), (F)** Massive fine-grain sandstone, rock fragments (R) present as a small amount, feldspar is very rarely present, Sterling #6-G, 7669 ft.

Massive to Weakly Laminated Calcareous Mudstone

Massive to weakly laminated calcareous mudstone is characterized in core by medium-gray to black-colored beds ranging from 5 inches up to 3 ft. It is mostly present with massive structure; some weakly laminae less than 1 mm in size are present locally (Figure 4-9B). It is commonly fractured (Figure 4-9A) but less fissile compared to siliciclastic-dominated mudstones. It shows a coarsening upward trend locally, with a sharp contact towards the top (Figure 4-9C). It is brecciated locally, and the cracks are filled with calcite cement (Figure 4-9D). Burrows are rarely observed. Massive to weakly laminated calcareous mudstone in Harwood Trust #2 core has a mild reaction to diluted HCL because of its high carbonate contents.

XRD results show that total carbonate contents (calcite, dolomite, aragonite and siderite) account for 55.5 wt.% on average (N=12). Within the three dominant components (quartz, clay, and carbonate), total carbonate minerals account for 60.7 wt.% on average (N=12). Calcite is the dominant carbonate mineral. Quartz only accounts for an average of 23.2 wt.% (N=12). On average, total clay minerals account for 16.1 wt.% (N=12). The average TOC value in massive to weakly laminated calcareous mudstone is 1.5 wt.% (N=12).

Based on thin section observation, the darkening of color from gray to black observed in cores is related to the presence of carbonate content compased of microfossils and carbonate mud. Based on TOC results, presence of organic matter also affects the color difference; the more carbonate content in the rock, the lighter it looks. Dominant fossils grain size ranges from 10 to 40 microns, only a few reach 200 microns. Fossil fragments contain mainly of calcispheres, radiolarian, and ostracods, with minor gastropod and foraminifer and other skeletal debris (Figure 4-10C, D). Under the

microscope, brecciated cracks are filled in mostly with calcite cement (Figure 4-10E). Brecciated clasts are angular to sub-angular, ranging from sand to pebble size (400 micron to > 4mm) (Figure 4-10F).

SEM images show that quartz grains range from 3 to 15 microns which was not able to be identified in thin sections. Albite and orthoclase are locally present in very small amounts. Organic matter is present around the fossil fragments (Figure 4-11C). Pyrite framboids are common compared to those in sandy silt stone and argillaceous mudstone lithofacies (Figure 4-11A, B). Pyrite also appears around dolomite minerals (Figure 4-11D). The dominant clay mineral is illite (Figure 4-11B).

The massive to weakly laminated calcareous mudstone is interpreted to deposit in a low-energy, anoxic environment below storm wave base, as evidenced by fine sediment size, lack of current-generated sedimentary structure, and richness of organic matter. Commonly present radiolarians also indicates a low-energy environment; they accumulate as a result of sinking from the overlying water after dying (Flügel, 2004). The fine sediment, a mix of biogenic and terrigenous origin, is interpreted to be deposited through hemiplegic settling (Stow and Piper, 1984).

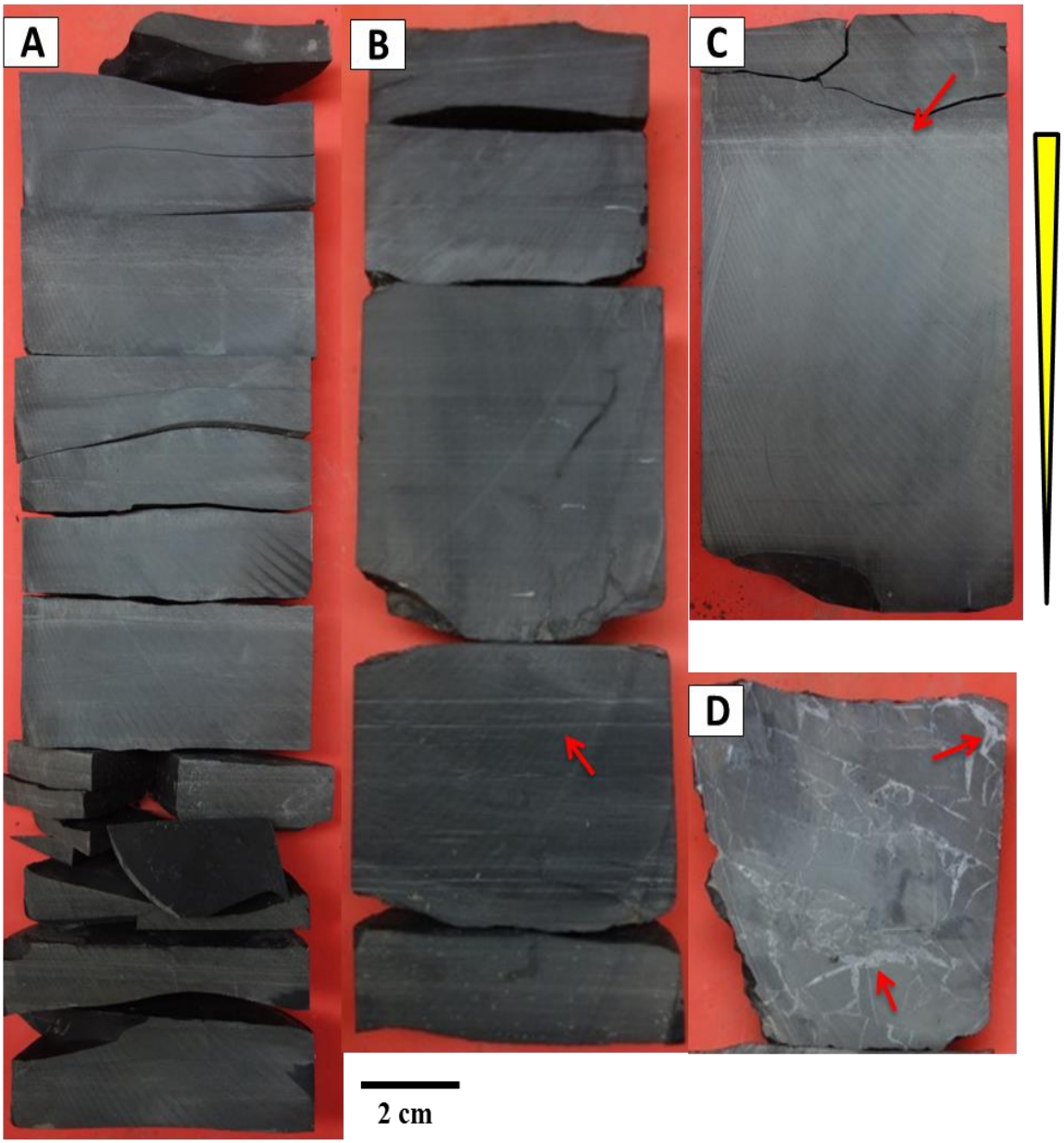

Figure 4-9: Slabbed core photo of massive to weakly laminated calcareous mudstone of the Harwood Trust #2 core. (A) Massive calcareous mudstone, 7598.6-7599.5 ft. (B) Calcareous mudstone with very weak lamination (arrow), 7491-7492 ft. (C) Calcareous mudstone shows coarsening upward trend with a sharp contact (arrow) towards to top, 7596.5-7597.5 ft. (D) Calcareous mudstone brecciated locally. The cracks are filled by calcite cement (arrow).

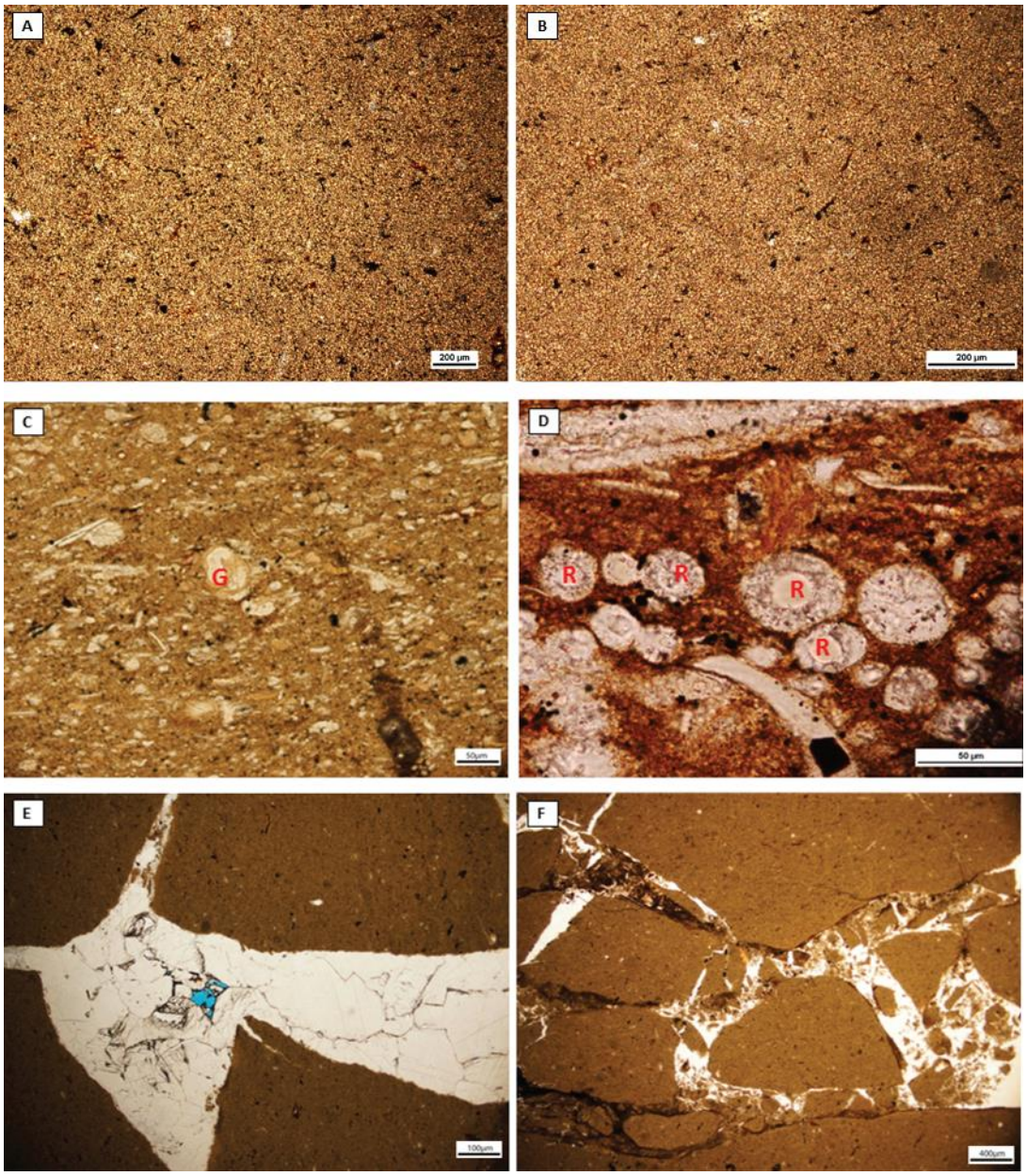

Figure 4-10: Photomicrographs of massive to weakly laminated calcareous mudstone in Harwood Thrust #2 core. **(A), (B)** Massive to weakly laminated calcareous mudstone, 7498.3 ft. **(C)** Minor gastropode (G) fragments, 7489.3 ft. **(D)** Rardiolarins (R) are commonly present, 7489.3 ft. **(E)** The infilling cement is dominated by calcite, 7497.7 ft. **(F)** Locally brecciated calcareous mudstone, 7497.7 ft.

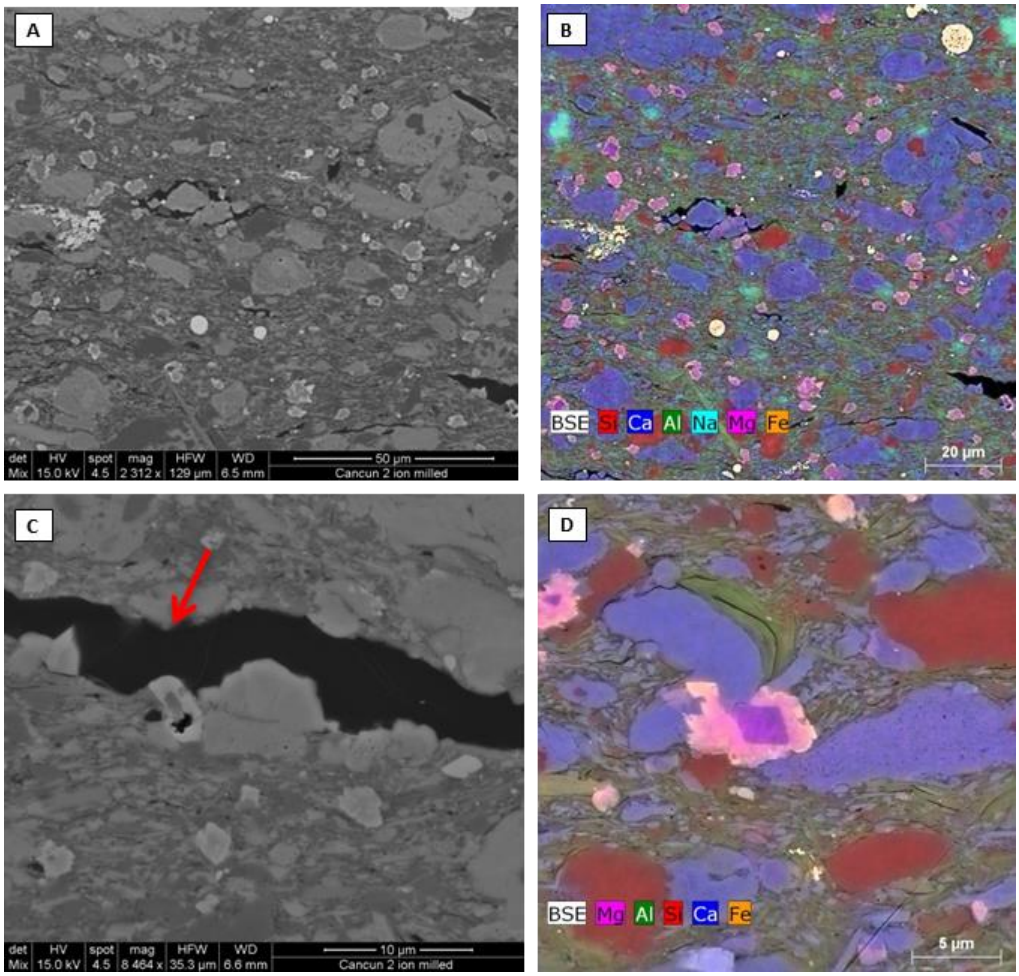

Figure 4-11: SEM and EDS images of Massive to Weakly Laminated calcareous mudstone, Harwood Trust #2, 7486.6 ft (A) SEM images of calcareous mudstone. (B) SEM-EDS images. Fossil fragments are in dark blue, clay minerals are dominated by illite (in green), some quartz grains (in red) are poorly sorted, pyrite framboids (upper right, in white) are commonly present, albite presents locally (in dark blue). (C) SEM images of organic matter (bitumen) (in red arrow) filling into the space between minerals. (D) SEM-EDS image shows pyrite rims are commonly seen around dolomite grains.

Laminated Calcareous Mudstone

Laminated calcareous mudstone is characterized by light-gray beds interbedded with dark-gray to black beds ranging from several to tens of feet. Light-gray laminae are present at a scale ranging from millimeters to centimeters, and their grain size is coarser than that of the darker laminae. Laminated calcareous mudstone in Harwood Trust #2 core has a mild reaction to diluted HCL because of the high carbonate content of the mudstone. It is usually topped by massive calcareous mudstone with a gradational contact (Figure 4-12C). An upward-fining trend (Figure 4-12D) and load structure (Figure 4-12B) are found locally in cores.

XRD results show that laminated calcareous mudstone and bioclastic packstone facies contain the highest carbonate content of the mudstone lithofacies. The average total carbonate content is 67.2 wt.% (N=16). Total carbonate minerals account for an average of 68.1 wt.% (N=16) within the three dominant components (quartz, clay, and carbonate). Calcite is the predominant carbonate mineral. Quartz accounts for 12.1 wt.% on average (N=16), and total clay minerals account for an average of 12.0 wt.% (N=16). Average TOC in laminated calcareous mudstone is 1.3 wt.% (N=16), which is lower than that of massive calcareous mudstone.

According to thin section observation, light-gray laminae are composed of bioclastic wackestone/packstone, while dark-gray laminae are composed of shaley carbonate mud (Figure 4-13A). Fossil fragments include ostracods, miliolid foraminifers, gastropods, and calcispheres (Figure 4-13B, C). Pore spaces within fossil fragments are filled with calcite cement (Figure 4-13B). The size of fossil fragments ranges from 50 to 110 microns, which is larger than that of massive calcareous mudstone.

SEM images show that organic matter is less commonly seen compared to that of calcareous mudstone (Figure 4-14). Quartz grains are present in a small amount, and albite and orthoclase are present locally.

The presence of shallow-marine fossils such as miliolid foraminifers in a deep-water depositional setting is the evidence of gravity-flow deposit (Flügel, 2004). Normal grading and soft sediment deformation are evidences of turbidity current deposit (Stow and Piper, 1984). Based on evidence discussed above and fine sediment size, laminated calcareous mudstone is interpreted to be deposited by diluted turbidity current (Stow et al., 1996).

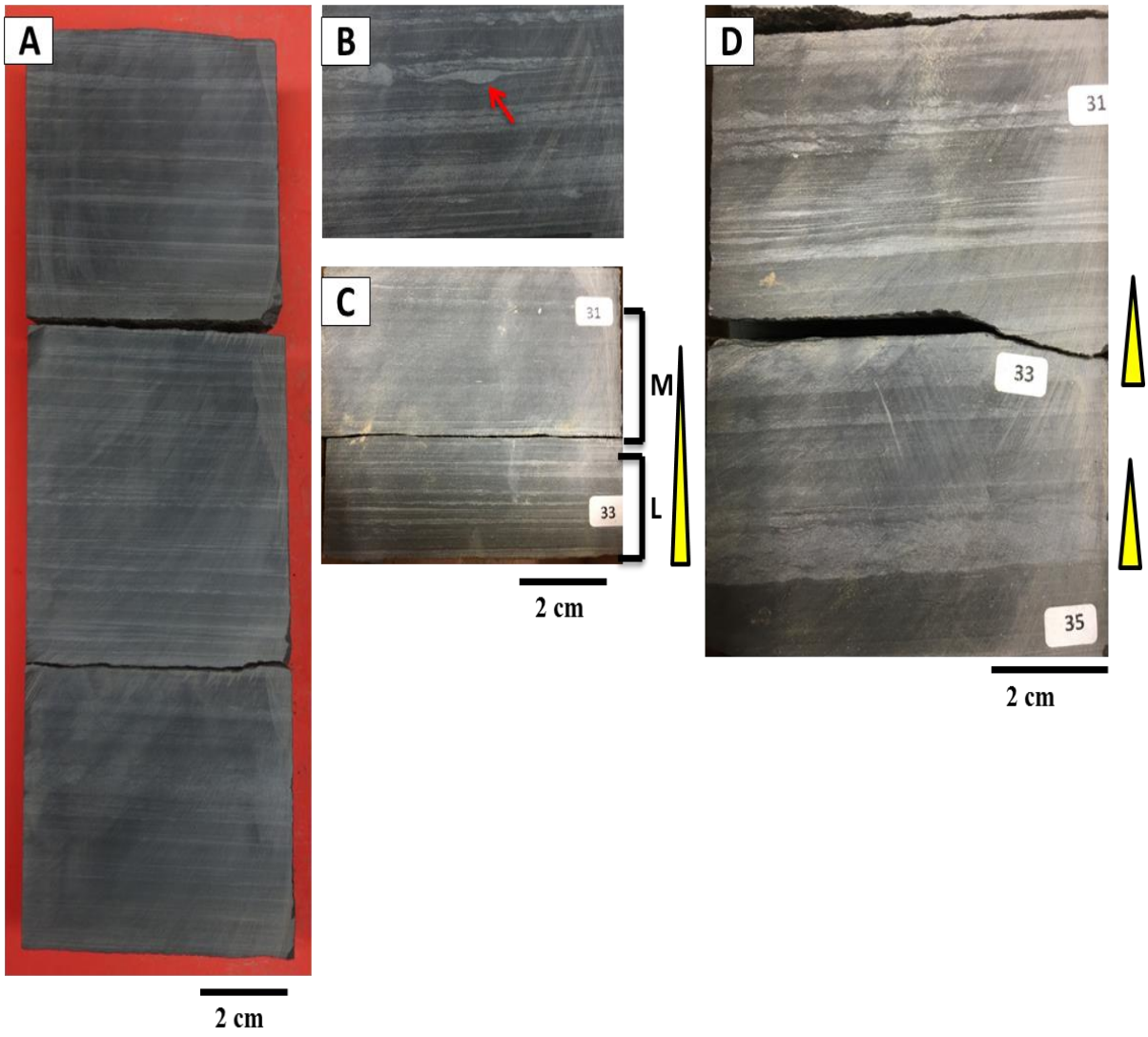

Figure 4-12: Slabbed core photo of laminated calcareous mudstone in Harwood Trust #2 core. **(A)** Laminated calcareous mudstone, 7709-7710 ft. **(B)** Load structure (arrow), 7669.1 ft. **(C)** Laminated calcareous mudstone (L) fines up into weakly laminated to massive calcareous mudstone (M), 7684 ft. **(D)** Lamination with small scale finning upward trend, 7718.9 ft.

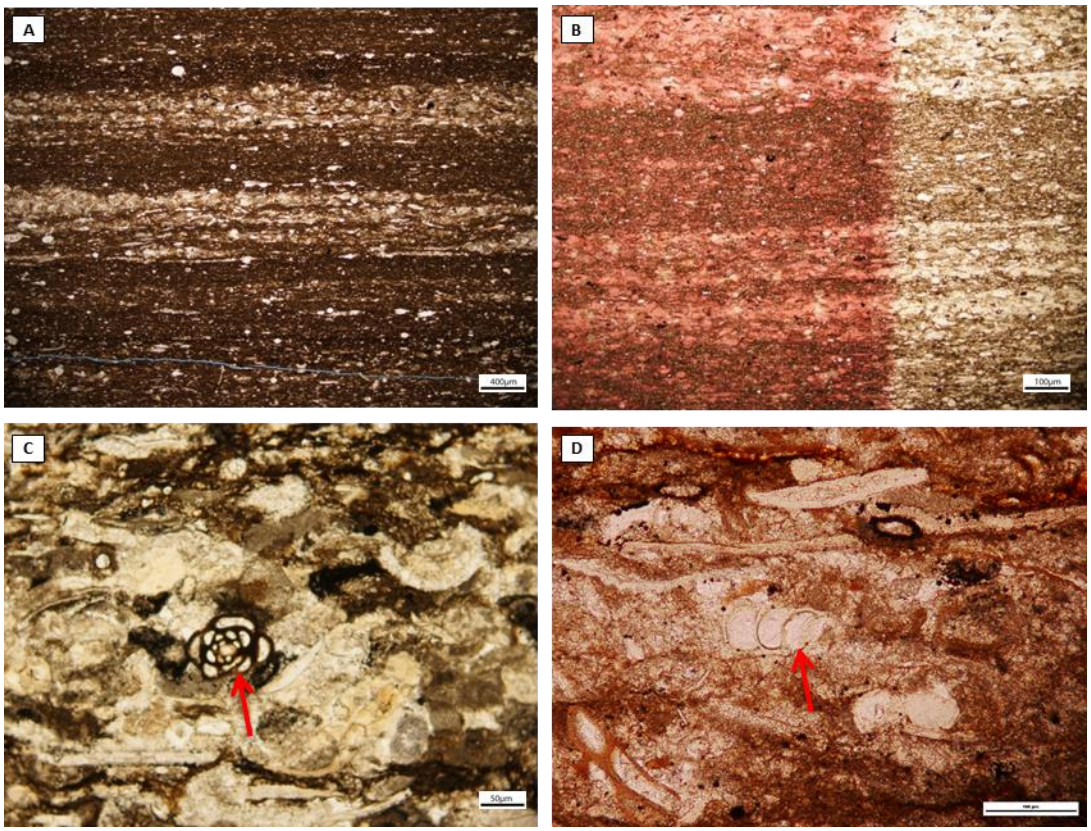

Figure 4-13: Photomicrographs of laminated calcareous mudstone. (A) Lamination is caused by grain size difference, Harwood Trust #2, 7554.6 ft. (B) Lamination is caused by grain size difference (the thin section was half stained), Harwood Trust #2, 7710.4 ft. (C) Miliolid foraminifer (red arrow) in the laminated bioclastic packstone, Harwood Trust #2, 77695.7 ft. (D) Gastropod fragment (red arrow) in the laminated wackestone, Harwood Trust #2, 7652 ft.

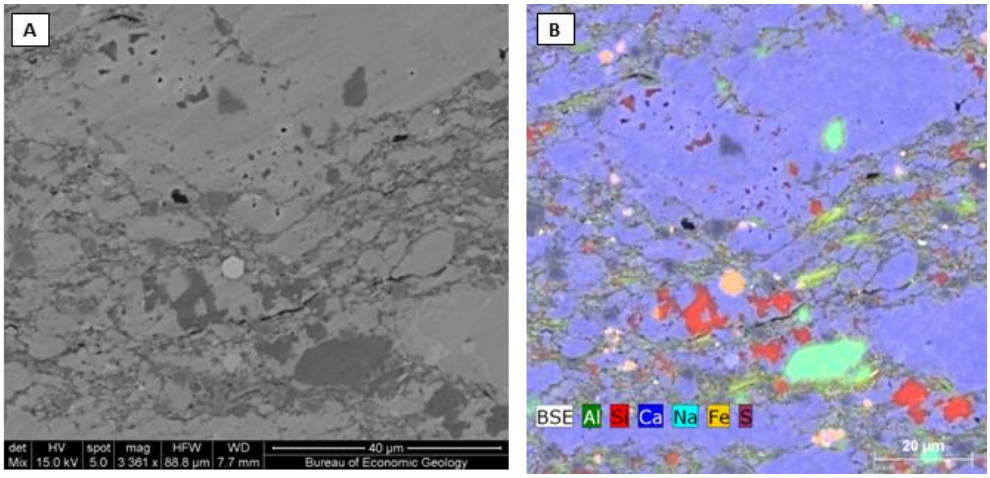

Figure 4-14: (A) SEM image of laminated calcareous mudstone and bioclastic packstone, Harwood Trust #2, 7679 ft. (B) SEM-EDS image: organic matters (in black) are less common compared to calcareous mudstone. Quartz grains (in red) and albite (in blue) are presence as a small amount.

Mud-dominated Bioclastic packstone/Rudstone

Mud-dominated bioclastic packstone/rudstone is characterized in core by dark to light-gray color. It is clay- to silt-sized matrix supported beds and composed of abundant scattered skeletal fossil debris such as crinoid (Figure 4-15A). Individual beds show massive structure ranging from a few inches up to 1 ft. This lithofacies is topped by calcareous mudstone (Figure 4-15B); it is not very commonly present, found only in the Powell E.L #1 core.

Thin sections observations show that the bioclast fragments consist of large fusulinid, echinoid, calcisphere, radiolarian, bivalves, bryozoan, and epimastoporids algae (Figure 4-16). It also contains lithoclasts (Figure 4-16E). Most fossil fragments preserve their internal structures, but some do not as a result of quartz replacement (Figure 4-16D). Calcite cement filled in intraparticle pore spaces within fossil grains (Figure 4-16B, C).

The presence of shallow-water bioclasts such as epimastoporid algae and large fusulinid indicates gravity-flow deposit at a deep-water depositional setting. Mud-dominated bioclastic packstone/rudstone is interpreted to deposit by debris flow based on the presence of scattered bioclasts and lithoclasts mixed with clay-sized matrix (Mulder and Alexander, 2001). Other evidence includes a lack of vertical grading or sedimentary structure, and chaotically distributed skeletal grains.

Figure 4-15: Slabbed core photo of mud-dominated bioclastic packstone/rudstone. (A) Skeletal fragments floating in the matrix rich sediments, Powell E.L #1, 8910-8911 ft. (B) Crinoid fragments are commonly seen (red box). It is topped by calcareous mudstone with a sharp contact, Powell E.L #1, 8905-8906 ft.

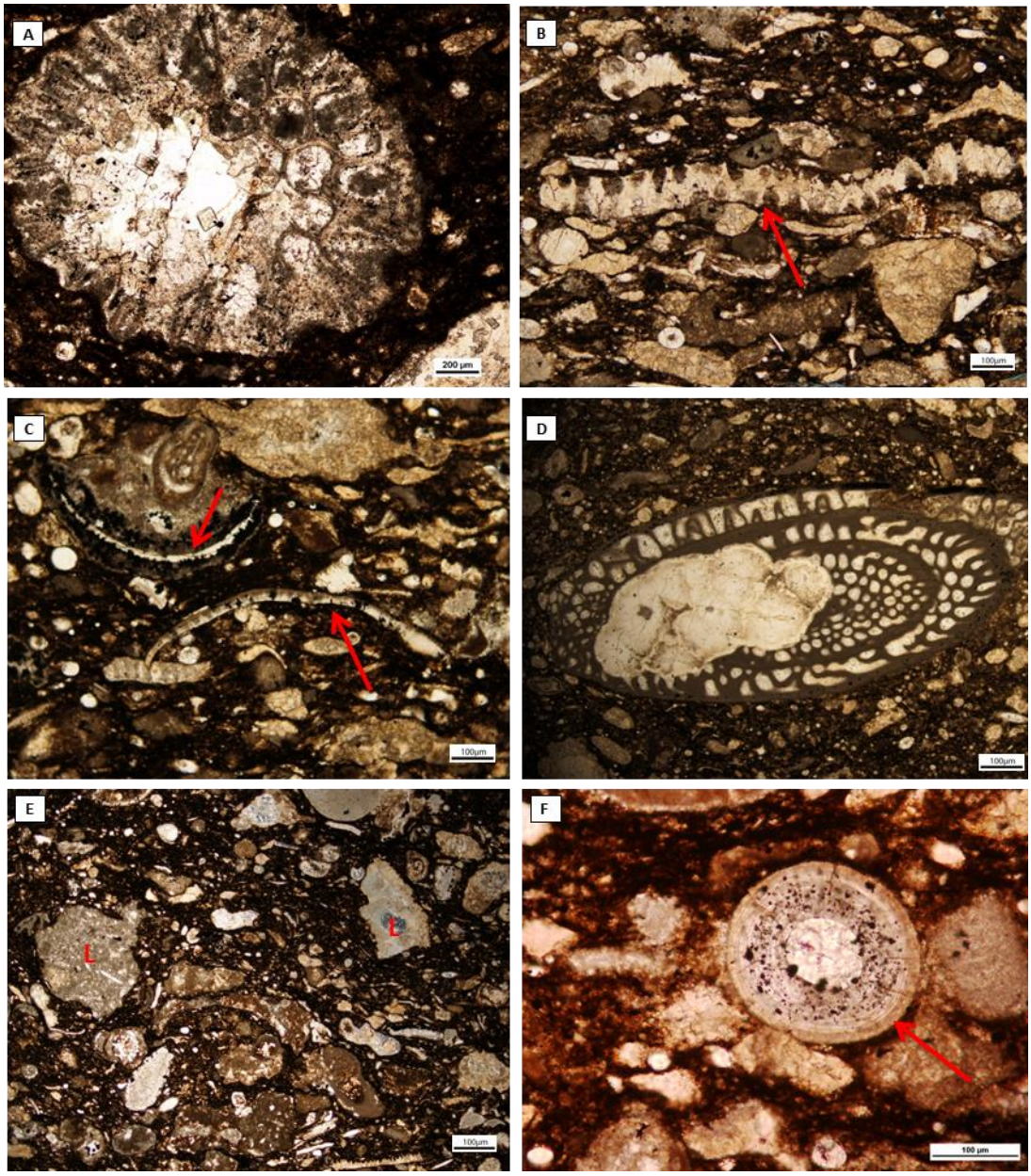

Figure 4-16: Photomicrographs of mud-dominated bioclastic packstone/rudstone, Powell E.L #1core. **(A)** Bryozoan fragment, 8907.6 ft. **(B)** Epimastoporid algae (arrow), 8907.6 ft. **(C)** Bivalve fragments, 8907.6 ft. **(D)** Large fusulinid fragment partially lose its internal structure due to quartz replacement, intraparticle pores are filled with calcite cements, 8907.6 ft. **(E)** Lithoclasts (L) present locally, 8907.6 ft. **(F)** Radiolarian (red arrow) showing concentric structure, 8822.3 ft.

Grain-dominated Bioclastic Packstone-Grainstone/Rudstone

Grain-dominated bioclastic packstone-grainstone/rudstone presents only in an 18-ft portion in the Harwood Trust #2 core. It is characterized in core by light-gray beds with the presence of fossil fragments (Figure 4-17A). It overlies and is topped by laminated calcareous mudstone and bioclastic packstone with a gradational contact. Mud stripes are commonly present toward the top (Figure 4-17B). Visible pores are observed in beds with abundant fusulinid grains toward the bottom (Figure 4-17C).

Based on thin section observation, fossil fragments are composed mainly of fusulinid, bivalve, large bryozoan fragment, crinoid, echinoid, and green algae (Figure 4-18). The green algae include epimastoporid algae (Figure 4-18B, E) and permocalculus algae (Figure 4-18F), which is of rock-building importance in Permian carbonates (Flügel, 2004). Peloid and lithoclast are also observed in the thin sections (Figure 4-18). Intraparticle pores within fossil fragments are highly cemented by calcite cement (Figure 4-18A, B).

Grain-dominated bioclastic packstone-grainstone/rudstone is interpreted to be deposited by hyperconcentrated density flow with evidence of outsized, shallow-water-origin fossil fragments present, including the presence of epimastoporid algae, which are commonly present in outer shelf environment, and large-sized fusulinid, which need a warm temperature to grow (Mulder and Alexander, 2001; Flügel, 2004). The good preservation of out-sized fossils such as bryozoans and fusulinids is interpreted to be caused by frictional freezing of hyperconcentrated density flow without much turbulence causing a loss of water from the flow (Beall, 1999; Mulder and Alexander, 2001).

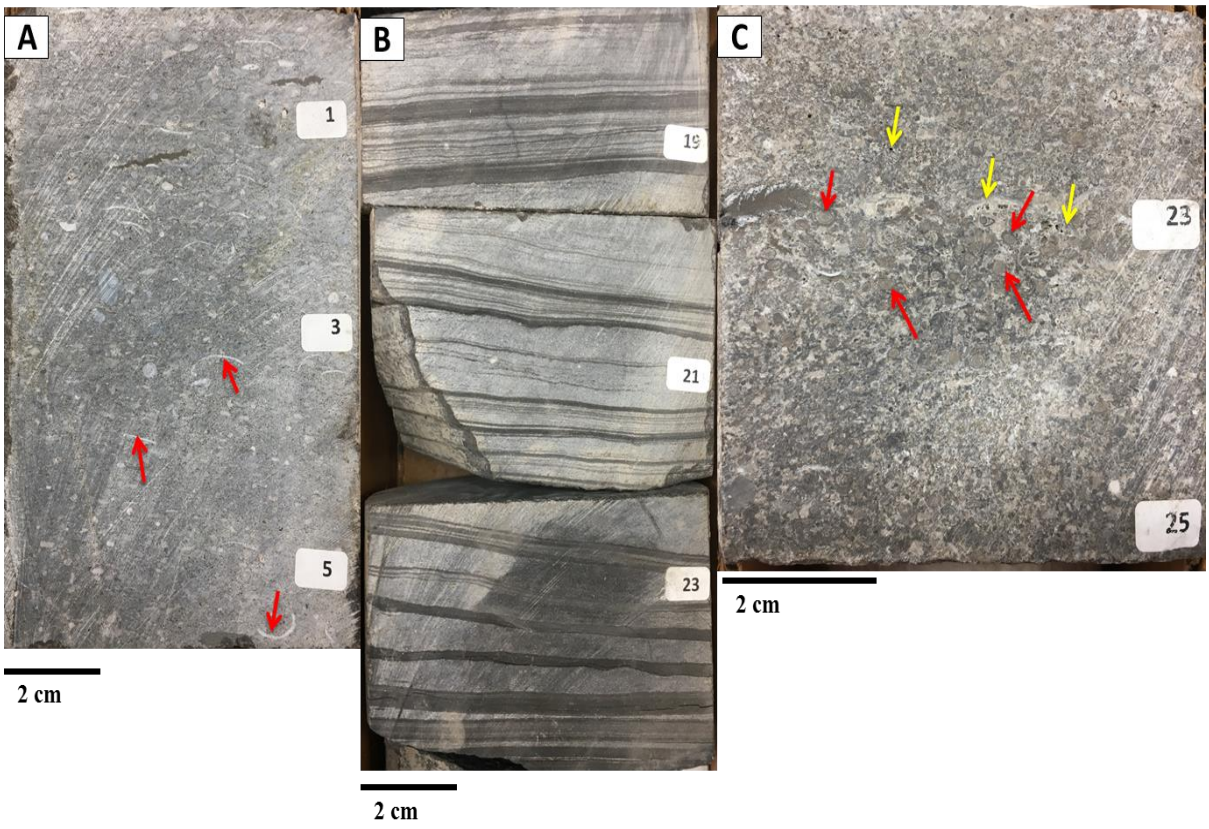

Figure 4-17: Slabbed core photo of grain-dominated bioclastic packstone-grainstone/rudstone in Harwood Trust #2 core. (A) Mollusk fragment (arrow) and other fossil fragment commonly present, 7572.8 ft. (B) Grain-dominated bioclastic packstone-grainstone/rudstone with muddy stripe, 7672.8 ft. (C) Concentrated fusulinid (red arrow) and visible porosity (yellow arrow), 7574.8 ft.

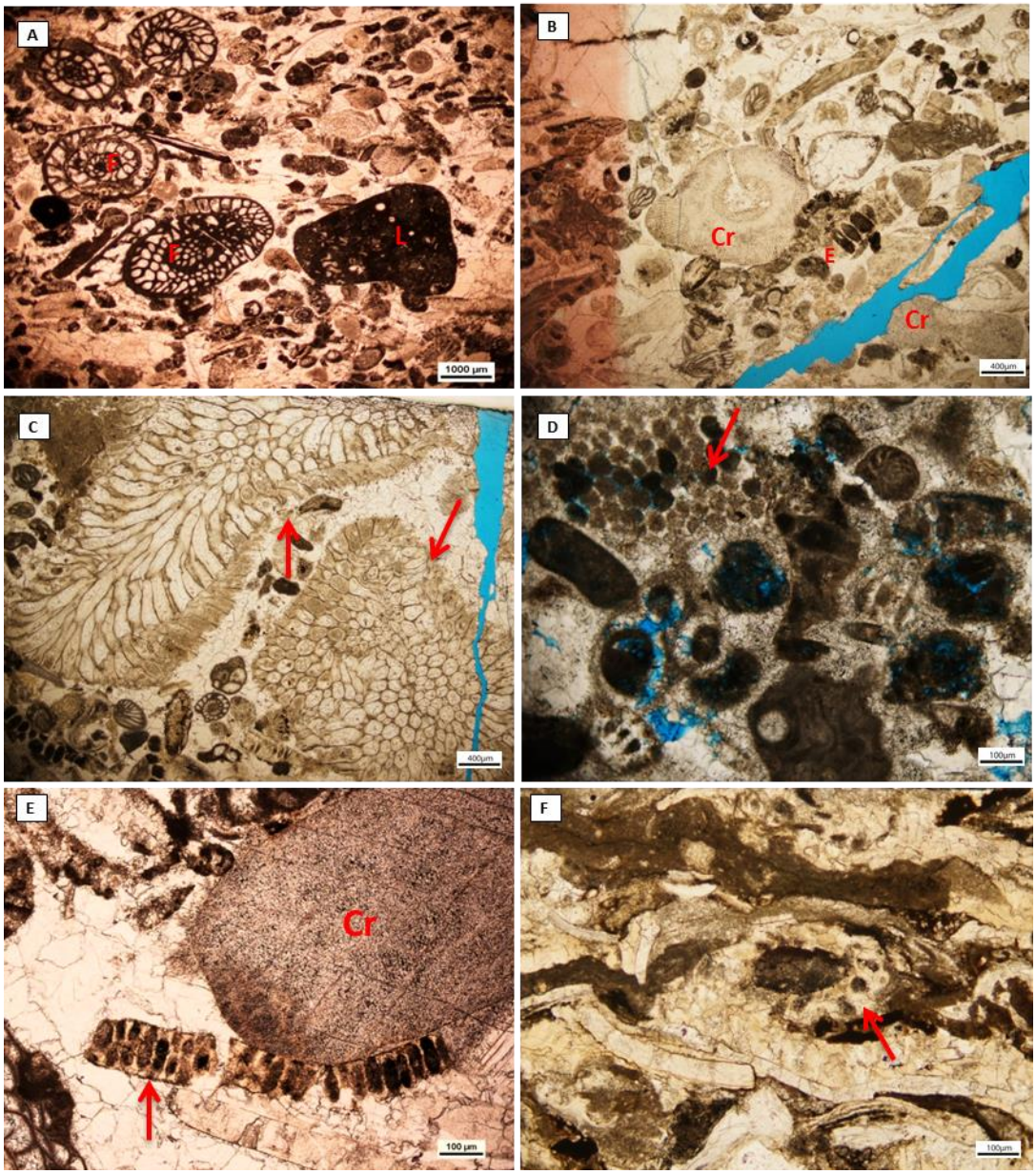

Figure 4-18: Photomicrographs of grain-dominated bioclastic packstone-grainstone/rudstone, Harwood Trust #2. **(A)** Lithoclast (L) and fusulinid (F) in bioclast grainstone, 7570.8 ft. **(B)** Crinoid (Cr), epimastoporids algae (E) in bioclast grainstone, thin section was half stained, 7569.2 ft. **(C)** Large bryozoan fragment in bioclast rudstone, 7570 ft. **(D)** Dissolution pores concentrated within skeletal fragments in bioclastic packstone, 7574.8 ft. **(E)** Epimastoporid algae (arrow) and crinoid (Cr), 7569.2 ft. **(F)** Permocalculus algae (arrow) in bioclastic packstone, 7568.8 ft.

DIAGENESIS AND PORE EVOLUTION

The Wolfcampian succession reveals a complex diagenesis history. Diagenetic processes of the siliciclastic-dominated interval include compaction, pyrite replacement, silica cementation, calcite cementation, siderite grain-coating, and dissolution. The calcareous-dominated interval experienced syntaxial-overgrowth calcite cementation, dissolution, isopachous-equant calcite cementation, compaction, blocky calcite cementation, mosaic calcite cementation, and minor dolomite cementation.

Compaction

The Wolfcampian succession experienced significant compaction, indicated in the very fine to fine sandstone lithofacies by long, concave-convex grain contacts between quartz grains (Figure 4-19A). Compaction caused the flow of ductile clay minerals into surrounding pore space (Figure 4-19A). Soft rock fragments underwent pseudoplastic deformation, resulting in the formation of pseudomatrix (Figure 4-19A) (Morad et al., 2010). Compared to sandstone, carbonate rocks show less significant evidence of compaction due to early calcite cementation. Skeletal grains show tangential to long contact (Figure 4-19B). However, intervals with less cementation show differential compaction between the more ductile, mud-dominated grains and the harder lithoclasts (Figure 4-19C).

Primary intergranular porosity is reduced significantly as a result of compaction. Some residual primary intergranular pores are preserved in sandstone with higher rigid-grain content.

Dissolution

Dissolution, which occurs in both siliciclastic-dominated and calcareous-dominated intervals, is demonstrated in sandstone by partial to pervasive dissolution of silica grains, which creates pore spaces (Figure 4-19D). Moldic pores, which are angular in shape and comparable with the size of very fine sand grain, are observed in some samples (Figure 4-19D). Partial dissolutions of feldspar grains and lithoclast grains were found in a small amount (Figure 4-19E, F, G). But most grains had been completely dissolved, leaving no evidence of the initial grain types. In the calcareous-dominated interval, dissolution occurs locally in grain-dominated bioclastic packstone-grainstone/rudstone lithofacies, which forms intraparticle pores within the skeletal fragments (Figure 4-19H).

Dissolution creates secondary porosity and is considered to have good reservoir potential. However, some secondary intragranular pores are poorly connected, especially in the calcareous-dominated interval, resulting in lower permeability.

Silica Cementation

Silica cement present only in the siliciclastic-dominated interval, is found in very fine to fine sandstone lithofacies in the form of partial to complete quartz overgrowth. A thin rim defines the boundary between the overgrowth and the detrital quartz grain (Figure 4-19I, J). It is more common to observe quartz overgrowth in sandstone with higher rigid-grain content than in sandstone with more-ductile clay content.

Quartz overgrowth occludes intergranular pores and further reduces primary porosity. It is present only in small quantities because of severe compaction, which reduces the space for silica cement to grow.

Siderite Coating

Siderite coating is commonly found in very fine to fine sandstone, especially in the Sterling Fee #6-G core. It is characterized by rhombic to slightly lozenge-shaped dark brown rim around silica grain (Figure 4-19K, L). Compared to diagenetic clay grain-coating, siderite rim is much thicker and the siderite crystal size is much larger than clay minerals (Ulmer-Scholle, 2014; Dr. Shirley P. Dutton at BEG, personal communication). Quartz overgrowth is less commonly seen in sandstones with grain-coating siderite minerals. Sandstones having poorly developed clay coats are highly cemented with authigenic quartz (Figure 4-19I, J), and are more compacted (Figure 4-19A). However, siderite grain-coating is unable to inhibit calcite cement precipitation which postdates the siderite rim (Figure 4-19M, N)

Siderite coats are of great importance in porosity preservation for sandstones in the Wolfcampian siliciclastic-dominated interval. Well-developed, continuous grain-coating siderite rims inhibit precipitation of quartz cement, thus preserving some intergranular porosity.

Calcite Cementation

Calcite cementation is commonly found in the Wolfcampian succession. In very fine to fine sandstone lithofacies, it occurs as blocky, homogeneous calcite cement around silica grains (Figure 4-19M, N).

In the calcareous-dominated interval, calcite cement occurs in various textural habitats. Syntaxial overgrowths of calcite cement around echinoid fragments are common

in mud-dominated bioclastic packstone/rudstone and grain-dominated bioclastic packstone–grainstone/rudstone (Figure 4-19S). In grain-dominated bioclastic packstone-grainstone/rudstone, isopachous-equant calcite cement precipitates around skeletal fragments, surrounded by pervasive blocky calcite cement (Figure 4-19O, P). In both mud-dominated bioclastic packstone/rudstone and grain-dominated bioclastic packstone-grainstone/rudstone lithofacies, mosaic calcite cement occurs within the intraparticle pores of fossil fragments (Figure 4-19R).

Calcite cement is commonly present in both intervals, occluding the pore space. Blocky calcite cement is of significant influence in reducing interparticle porosity in both siliciclastic- and calcareous-dominated intervals; mosaic calcite cement occludes intraparticle pore spaces in the calcareous-dominated interval.

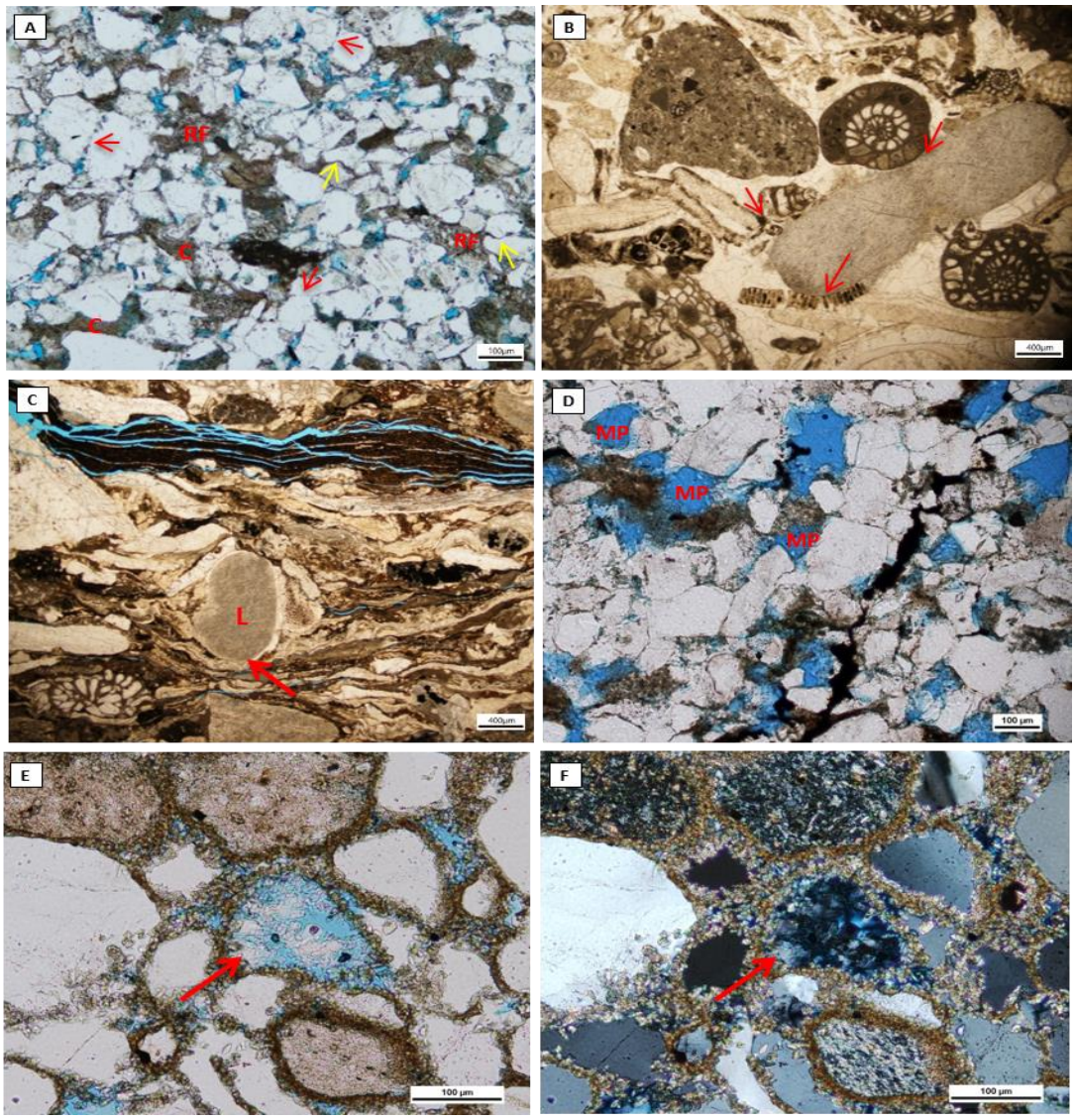

Figure 4-19: Photomicrographs and SEM-EDS photos of diagenesis processes in the Wolfcampian succession. **(A)** Quartz grains show line (red arrow) and concave-convex grain contacts (yellow arrow). Clay minerals (C) occlude surrounding pore space. Soft rock fragments (RF) form pseudomatrix, Sterling Fee #6-G, 7665 ft. **(B)** Skeletal grains show tangential to long contact (red arrow), Harwood Trust #2, 7567.8 ft. **(C)** Differential compaction (red arrow) between lithoclast (L) and mud dominated grains, Harwood Trust #2, 7567.8 ft. **(D)** Moldic pores (MP), and dissolution pores (P), Sterling Fee #6-G, 7948.2 ft. **(E)** Partial dissolution of feldspar grain (arrow), plane light, Sterling Fee # 6-G, 7950.9 ft. **(F)** Partial dissolution of feldspar grain (arrow), cross-polarized light, Sterling Fee # 6-G, 7950.9 ft.

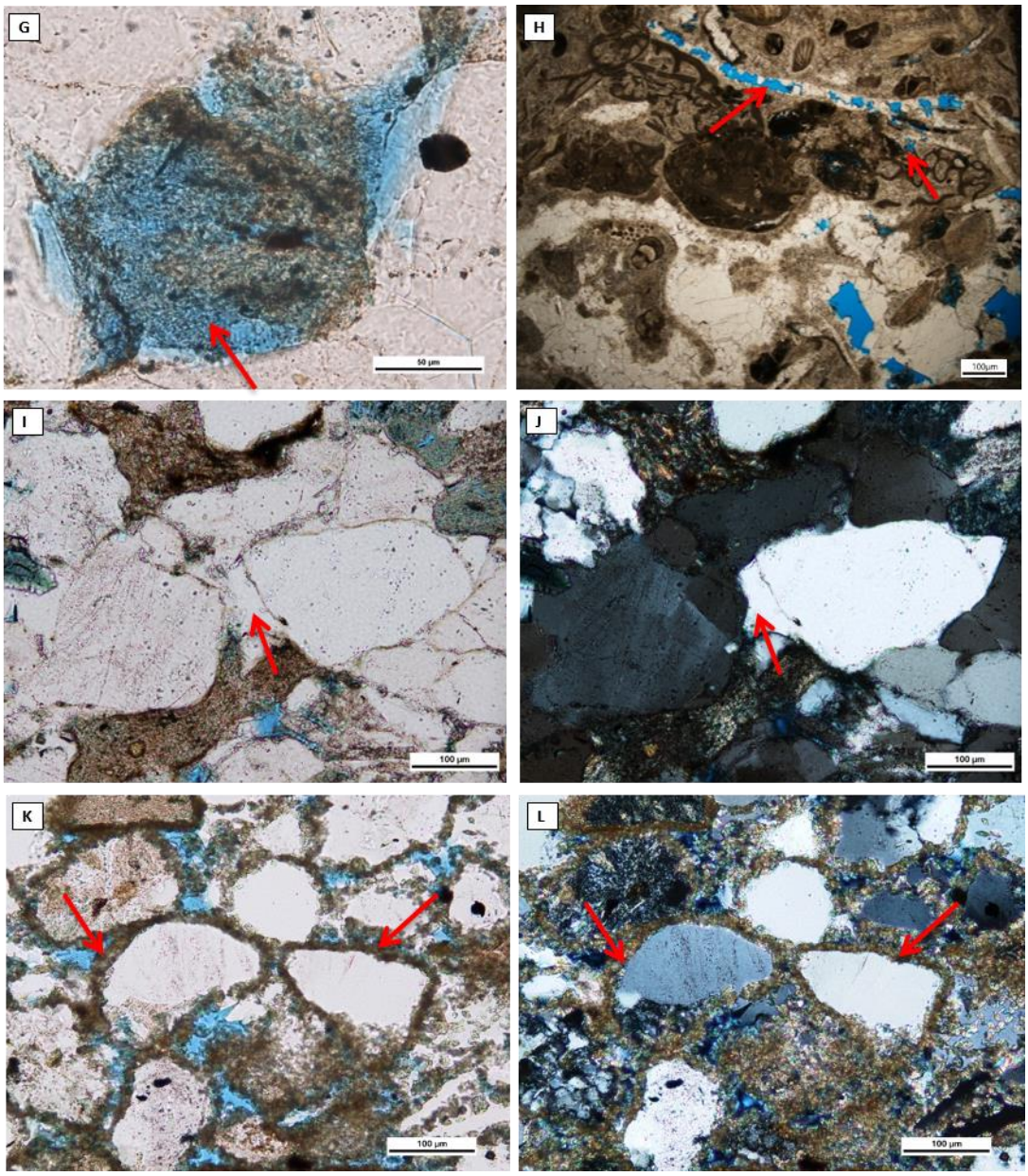

Figure 4-19: Continued. **(G)** Partial dissolution of rock fragment (arrow), Sterling Fee # 6-G, 7950.9 ft. **(H)** Dissolution within skeletal fragments in bioclastic packstone, Harwood Trust #2, 7574.8 ft. **(I)** Quartz overgrowth (arrow) in sandstone, cross-polarized light, Sterling Fee #6-G, 7917 ft. **(J)** Quartz overgrowth (arrow) in sandstone, plane light, Sterling Fee #6-G, 7917 ft. **(K)** Grain-coating siderite cement (arrow), plane light, Sterling Fee #6-G, 7950.9 ft. **(L)** Grain-coating siderite cement (arrow), plane light, Sterling Fee #6-G, 7950.9 ft.

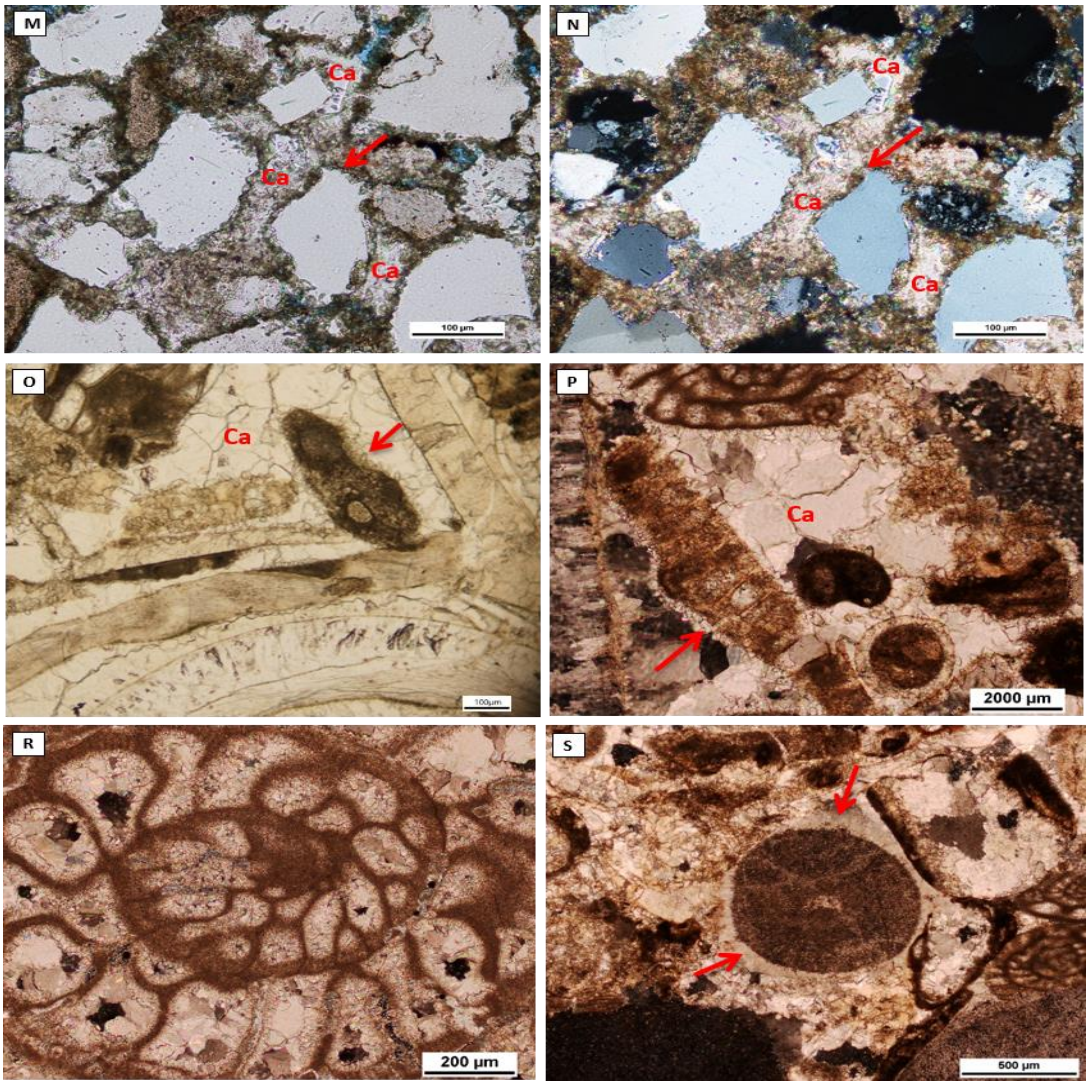

Figure 4-19: Continued. **(M)** Grain-coating siderite cement (arrow) predates calcite cement (Ca), plane light, Sterling Fee #6-G, 7651 ft. **(N)** Grain-coating siderite cement (arrow) predates calcite cement (Ca), cross-polarized light, Sterling Fee #6-G, 7651 ft. **(O)** Isopachous-equant calcite cement (red arrow) pre-dates the blocky calcite cement (Ca) in bioclastic packstone-rudstone, plane light, Harwood Trust #2, 7569.2ft. **(P)** Isopachous-equant calcite cement (red arrow) pre-dates the blocky calcite cement (Ca), cross-polarized light, Harwood Trust #2, 7570 ft. **(R)** Intraparticle pores of fusulinid fragment are filled with mosaic calcite cement, cross-polarized light, Harwood Trust #2, 7570.8 ft. **(S)** Syntaxial overgrowth calcite cementation (red arrow) around echinoid grain, cross-polarized light, Harwood Trust #2, 7592 ft.

GEOCHEMICAL DATA INTEGRATION

XRF-based Facies Correlations

Identification of lithofacies through petrographic observation is integrated with XRF measurements in order to interpret the overall trend in lithofacies variation and cyclicity, especially focusing on mudstone facies. In this study, it has been very difficult to correlate the interpreted lithofacies with the wireline log because of the rapid facies change (from a scale in feet down to inches) within the relative short core length, ranging from 61 to 157 ft. The conventional vertical resolution of the wireline log is several to tens of feet—e.g., 2 ft for gamma-ray log (Schlumberger Well Services, 1983). The XRF curve acts as a chemical log that can be correlated with the core descriptions for facies interpretation with the help of mineral composition, based on XRD results for mudstone facies. The XRF reveals the foot-scale cyclicity that the wireline log cannot identify.

XRD results from mudstone facies correlate well with XRF data. Three of the major elements from XRF data—calcium (Ca), silicon (Si), and aluminum (Al)—were used as proxies for three principal rock-forming minerals—calcite, quartz, and clay minerals, respectively—in the mudstone facies. The Si element and quartz, Ca and calcite, Al and clay minerals, and magnesium (Mg) and dolomite all show very good correlation (Figure 4-20). Si is also present in clay minerals in mudrocks. In order to remove the effect of clay minerals, Si/Al is used as a proxy for quartz in mudrocks (Pearce and Jarvis, 1992; Pearce et al., 1999). Aluminum and titanium (Ti) are commonly

of detrital origin and are usually immobile during diagenesis (Calvert and Pedersen, 1993; Tribovillard et al., 1994).

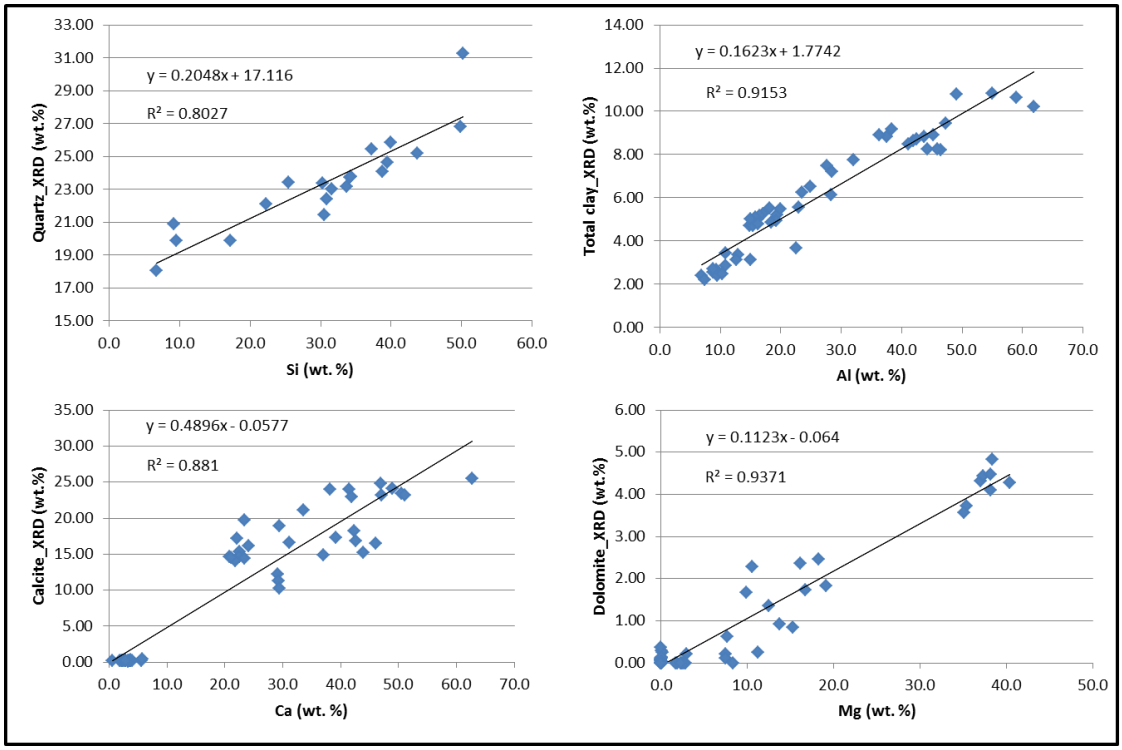

Figure 4-20: Plots showing correlative relationships between XRD minerology and XRF data.

XRF data were collected from the Noelke #38 core, representing the siliciclastic-dominated interval, and the Harwood Trust #2 core, representing the calcareous-dominated interval. XRF-based correlation was able to identify chemofacies used to reveal mineralogical variability, especially in mudrocks, at a sub-lithofacies scale. Computed gamma ray (CGR) logs were created, discussed in the Method and Dataset chapter, using XRF-based chemical data from the cores and were correlated to simplified

core descriptions. Chemofacies were defined based on XRF responses, and its correlative relationship with XRD mineralogical components data (Figure 4-21 and Figure 4-22). The results were also correlated to the simplified core description. In the calcareous-dominated interval, six chemofacies are identified including carbonate, calcareous mudstone, argillaceous calcareous mudstone, siliceous calcareous mudstone, dolomitic calcareous mudstone, and dolomitic argillaceous calcareous mudstone (Figure 4-21). The siliciclastic-dominated interval is characterized by theses six chemofacies: argillaceous mudstone, siliceous mudstone, dolomitic siliceous mudstone, sandstone (Figure 4-22).

Comparison of CGR and gamma ray (GR) curves shows that GR log responses are less subtle compared with XRF-element responses, which are able to detect small changes in mineral components to show facies variation and lithologic cyclicity. The separation of GR and CGR curves indicates high U content, resulting in high responses on the GR log. Overreliance on the GR log, however, will misinterpret rocks with high U content as rocks with high clay-mineral content. XRF-based facies interpretation is very applicable for mudrocks by recording small changes in mineralogy, while GR logs usually show similar responses for mudrocks. For example, at around 7696ft of the Harwood Trust #2 core, the CGR curve is able to detected the thin (<2 ft) beds in between the carbonate, which is difficult for the GR log to detect (Figure 4-21).

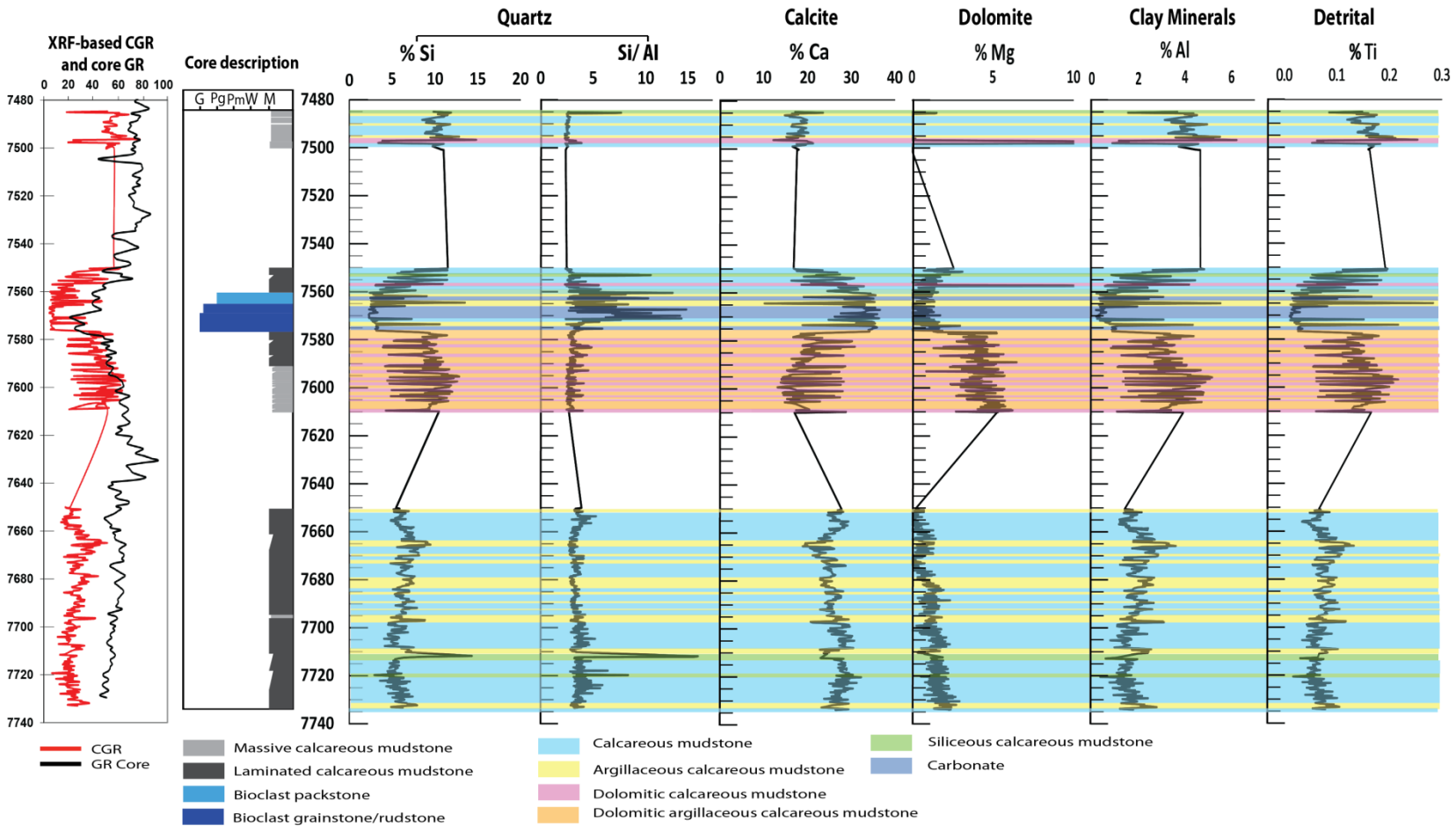

Figure 4-21: XRF-based facies correlation data in Harwood Trust #2 core with core description, GR log, and CGR log.

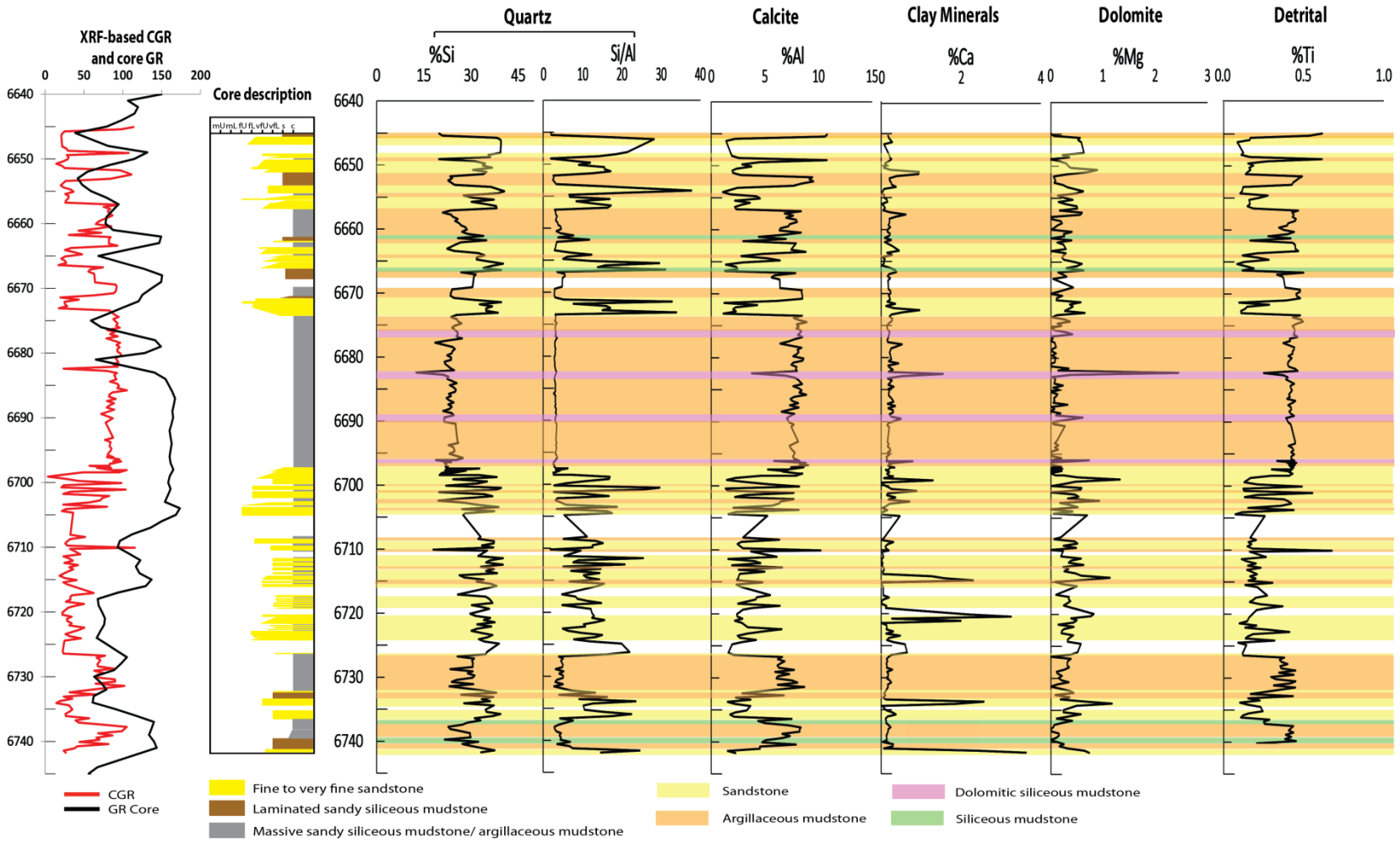

Figure 4-22: XRF-based facies correlation data in Noelke #38 core with core description, GR log, and CGR log.

Cyclicity

Depositional cyclicity during Pennsylvanian–Permian time has long been recognized in the Permian Basin (e.g., Silver and Todd, 1969; Elam and Chuber, 1972; Kerans and Kempter, 2002). However, basinal sediment cyclicity has been less discussed (e.g., Hobson et al., 1985; Nance and Rowe, 2015; Baumgardner et al., 2016). This study investigates chemofacies cycles in Wolfcampian basinal strata using XRF facies correlation.

High-frequency cycles are observed in both intervals with evidence of repetitive patterns of XRF-based chemofacies. Each individual cycle is meter-scale, with thickness ranges from 1 to 10 ft. These cycles are at the same scale of cycles discussed by Baumgardner et al. (2016) on Wolfcamp–lower Leonard basinal mudrocks (1–5 ft) in the Midland Basin. A typical cycle consists of a relatively carbonate-rich chemofacies overlain by a relatively siliclastic-rich chemofacies. Examples of these cycles, which are commonly present in the Harwood Trust #2 core, include calcareous mudstone overlain by argillaceous calcareous mudstone or siliceous calcareous mudstone (Figure 4-23 A), dolomitic calcareous mudstone overlain by dolomitic argillaceous calcareous mudstone (Figure 4-23 B). However, carbonate overlain by argillaceous calcareous mudstone is interpreted as event cycle (Figure 4-24). Because based on core and thin section observation, this interval is interpreted to be deposited by debris flow. For the Noelke #38 core, this type of cycle is more typical in mudrocks. An example is dolomitic siliceous mudstone overlain by argillaceous mudstone (Figure 4-25).

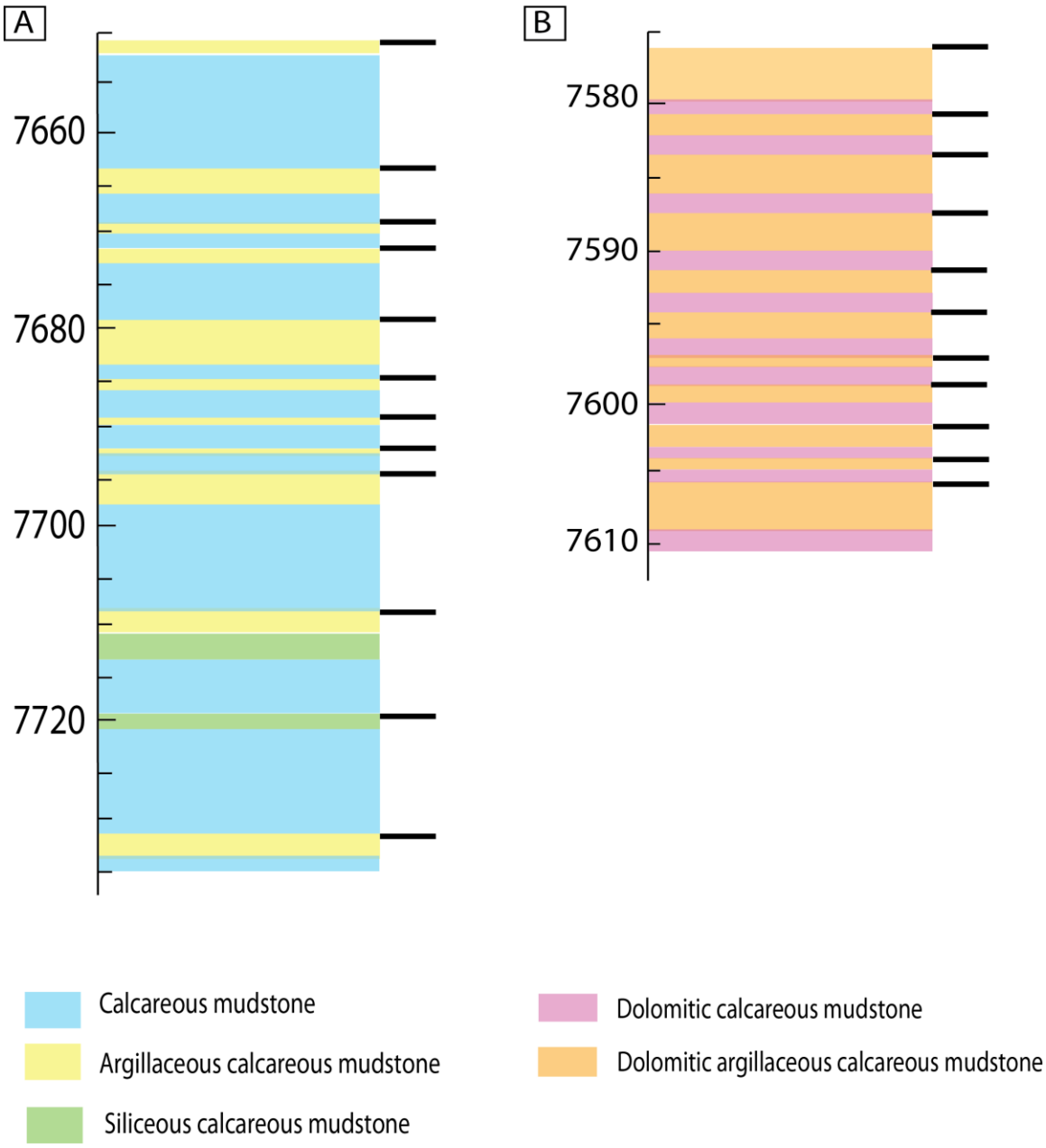

Figure 4-23: Closed up sections from the Harwood Trust #2 core showing the siliciclastic/calcareous cycles with marked cycle tops

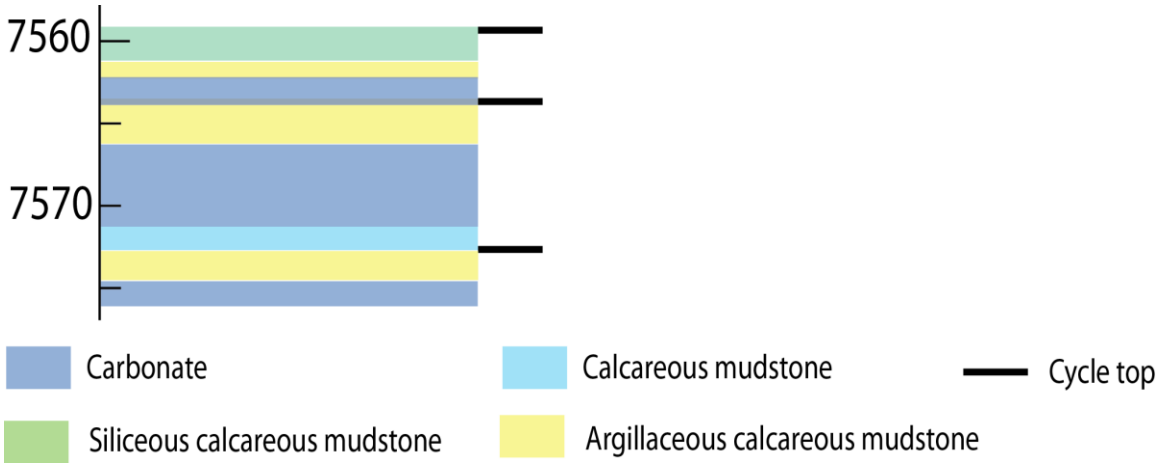

Figure 4-24: Even cycles caused by gravity-flow deposition from the Harwood Trust #2 core with marked cycle tops.

Figure 4-25: Closed up sections from the Noelke #38 core mudrock interval showing the siliciclastic/calcareous cycles with marked cycle tops.

Paleoenvironment and TOC Preservation

Three main factors control the enrichment of organic matter in sediment: (1) primary surficial productivity (Pedersen and Calvert, 1990; Sageman et al., 2003), (2) sediment accumulation/dilution (clastic influx) (Murphy et al., 2000; Sageman et al., 2003), and (3) organic-matter preservation/decomposition (redox conditions) (Sageman et al., 2003; Mort et al., 2007). These controlling factors can be inferred from the variation of XRF elemental concentration. Examples of correlative relationships between TOC enrichment and XRF elemental concentration are shown in Figure 4-26.

Organic matter is produced above the water–sediment interface with nutrient supply (Pedersen and Calvert, 1990). Nickel (Ni) and copper (Cu) are good values as proxy for organic-carbon sinking flux, which is frequently referred to as productivity (Tribovillard et al., 2006; personal commun., Dr. Stephen C. Ruppel, Bureau of Economic Geology). However, if trace elements have a good correlation with Al or titanium (Ti), which indicate detrital origin (Calvert and Pedersen, 1993; Tribovillard et al., 1994), the trace elements are mainly of detrital provenance and cannot be used for paleoenvironmental studies (Tribovillard et al., 2006). This phenomenon happens in the Noelke #38 core, where Ni and Cu show very strong correlation with Al and Ti (R^2 = 0.7). As a result, Ni/Al and Cu/Al are used as proxies of paleoproductvity by removing the influence of detrital input (Tribovillard et al., 2006; Wang et al., 2017). Phosphorus (P) is an important nutrient for biological growth and thus is used as an indicator of biological productivity (Ingall et al., 1993; Schmitz et al., 1997). Results from the

mudrock intervals in both cores show that TOC value has positive covariance with Ni, Cu, and P (Figures 4-27, 4-28). A typically example is at around 7,560 ft in the Harwood Trust #2 core, where the sharp increase of the three productivity indicators (Ni, Cu, P) correlates to an increase in the TOC value (Figure 4-25).

After production, the preservation of organic matter requires a low-oxygen-level, reducing environment (Demaison and Moore, 1980; Wilkin et al., 1997). Trace elements can be used as proxies for bottom-water anoxia because they are redox-sensitive and relatively immobile in the sediments (Algeo and Rowe, 2012). Molybdenum (Mo) and U are considered to be reliable redox indicators with minimal detrital influence (Dean et al., 1997; Rimmer, 2004; Tribovillard et al., 2006; Algeo et al., 2007) and are thus selected as representative proxies for paleoredox-condition reconstruction. Other redox-sensitive trace elements—including vanadium (V), thorium (Th), and chromium (Cr)—are also assessed as paleoredox proxies. Results from the mudrock intervals in both the Harwood Trust and Noelke cores show that TOC has a positive correlation with redox indicators, especially for Mo (Figures 4-27, 4-28). For example, from 6,690 to around 6,670 ft in the Noelke #38 core, TOC value increases with an increasing Mo value (Figure 4-26).

Deposition of a large amount of inorganic sediment will "dilute" organic-matter deposition and result in low organic-matter sediment (Sageman et al., 2003; Rimmer, 2004). Ti in the sediments is partly from aluminosilicates (e.g., clay minerals) and partly silt-sized heavy minerals such as augite and sphene, while Al is entirely from aluminosilicates (Bertrand et al., 1996; Rimmer, 2004). Thus Ti/Al can be used as an

indicator for siliciclastic grain size in mud-dominated facies (Bertrand et al., 1996). Sediment grain size increases with sedimentation rate; thus, higher Ti/Al is an indication of higher sedimentation rate (Bertrand et al., 1996; Murphy et al., 2000; Wang et al., 2017). Ti/Al shows a steady trend in the mudrock interval in the Harwood Trust #2 core and at the 6,673–6,697 ft interval in the Noelke #38 core, but a much higher value in the carbonate rock and sandstone interval (Figures 4-27, 4-28). Both cores show very weak correlations between Ti/Al and TOC values ($R^2 = 0.01$ for Harwood Trust #2 and $R^2 = 0.1$ for Noelke #38).

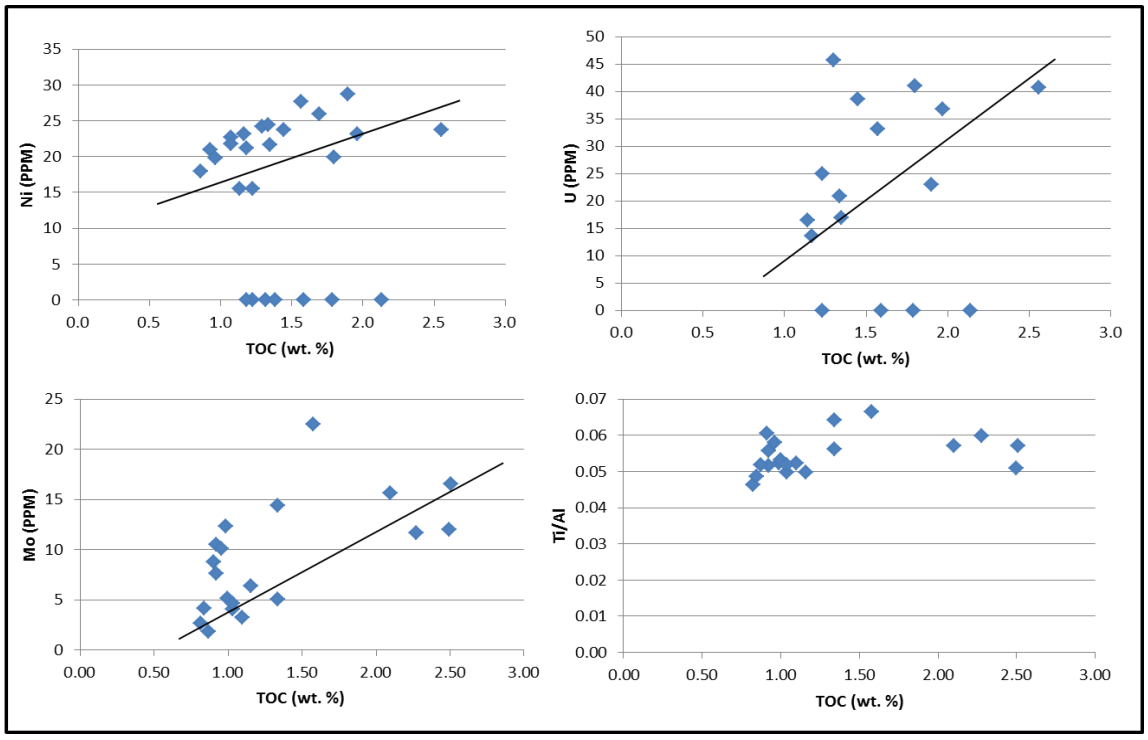

Figure 4-26: Plots showing correlative relationships between TOC enrichment and XRF elemental concentration.

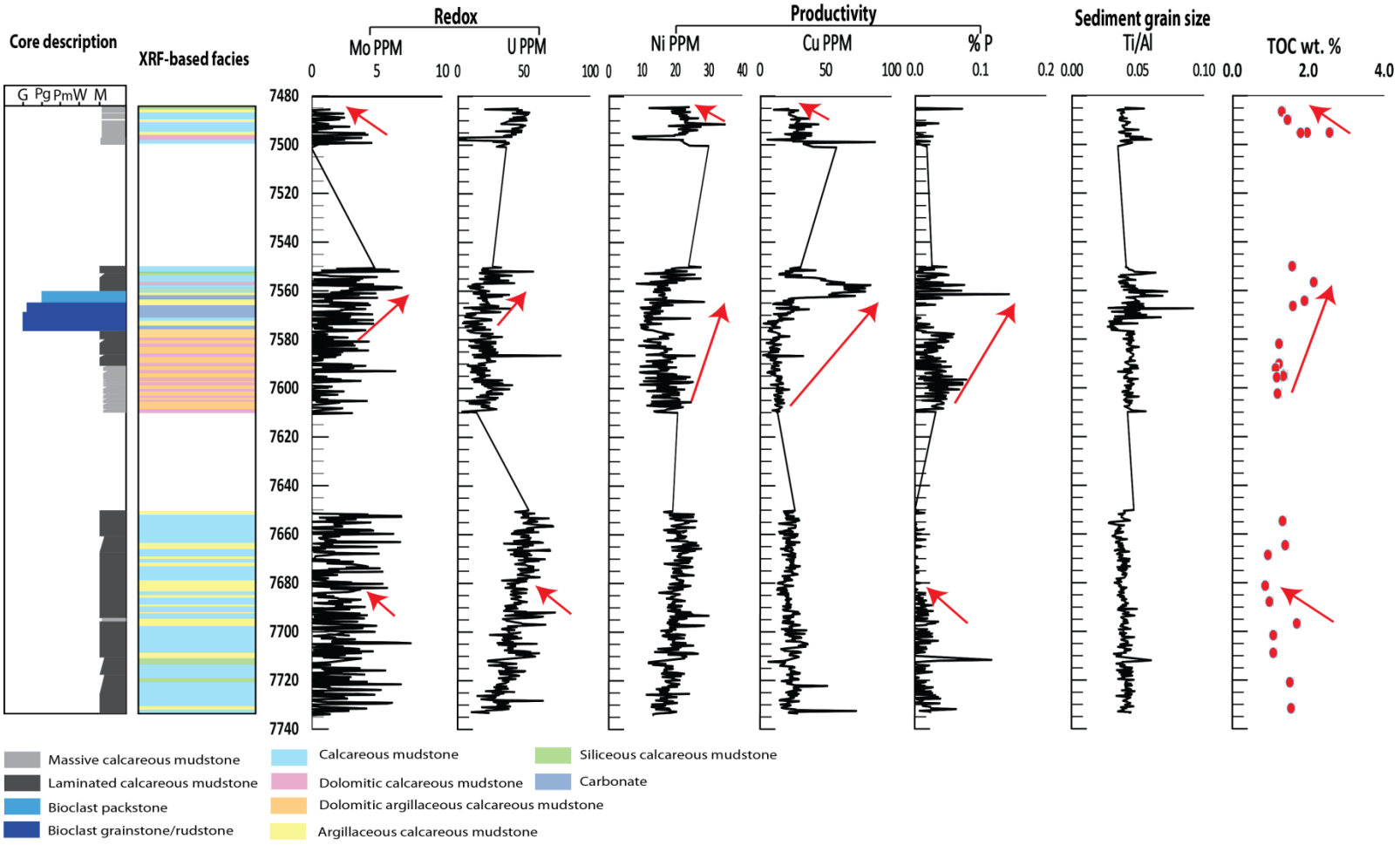

Figure 4-27: Variation of trace elements, P, Ti/Al, TOC, XRF-based facies interpretation and core description for Harwood Trust #2 core. TOC show positive covariance with redox indicators and productivity indicators (red arrow).

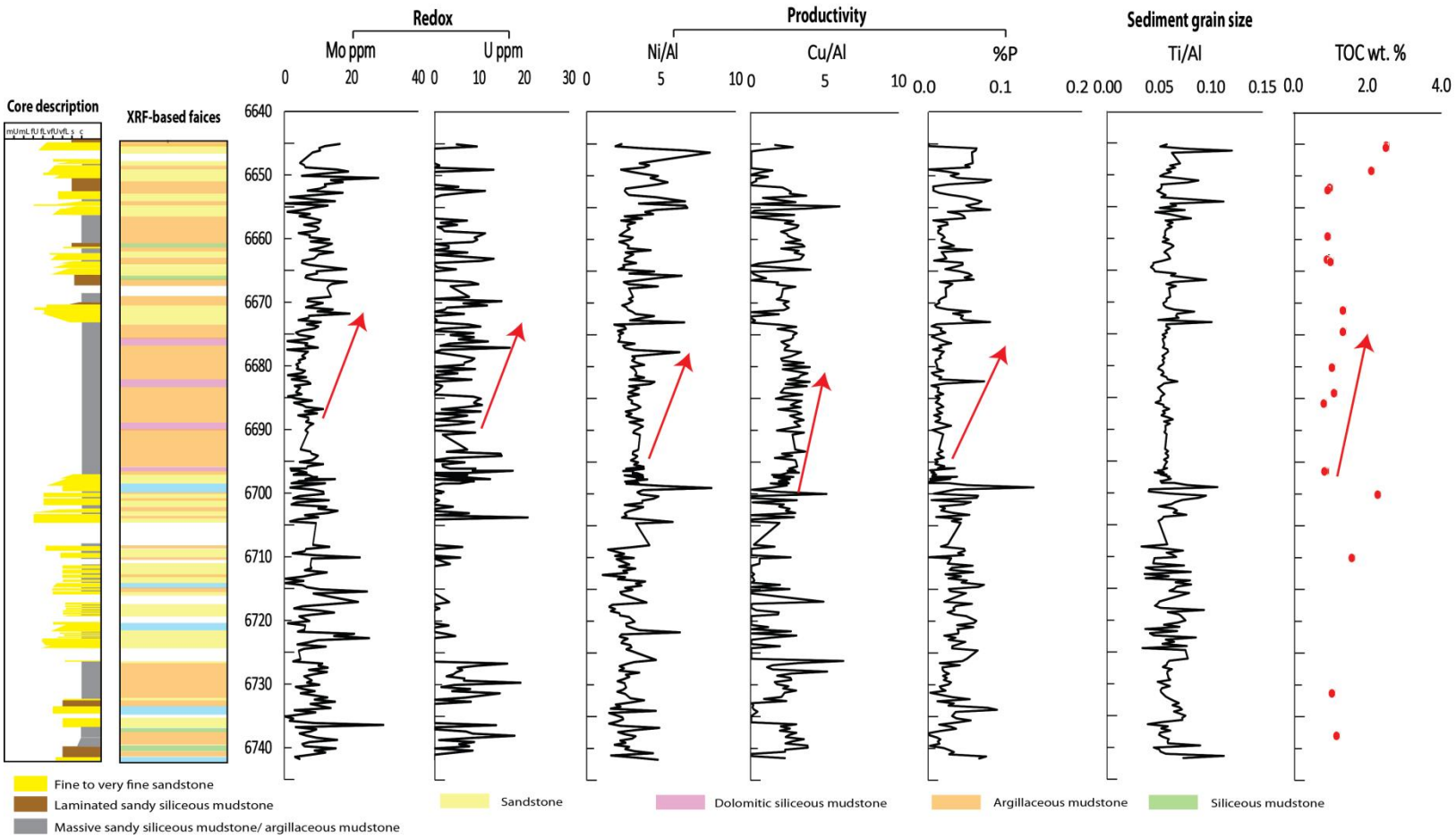

Figure 4-28: Variation of trace elements, P, Ti/Al, TOC, XRF-based facies interpretation and core description for Nolke #38 core. In the mudrock interval, TOC show positive covariance with redox indicators and productivity indicators (red arrow).

RESERVOIR POTENTIAL EVALUATION

Compaction and cementation have been recognized as importance factors in reducing original pore spaces (Ehrenberg et al., 2008; Taylor et al., 2010). As discussed in previous sections, the combined effect of compaction and cementation results in relatively low porosity and low permeability in the Wolfcampian succession. However, dissolution pores are found in both grain-dominated bioclastic packstone-grainstone/rudstone and very fine to fine sandstone lithofacies. Sandstone contains dissolution pores is considered to be potential reservoirs for hydrocarbon storage. The siderite grain coating in very fine to fine sandstone inhibits precipitation of quartz cement, thus preserving primary pore space and making effective storage spaces.

Based on thin section observation, the presence of dissolution pore increases from northwest to southeast, and is most abundant in the State University #1-EM core. Dissolution pores in both bioclastic packstone-grainstone/rudstone and very fine to fine sandstone are either intragranular pores or very poorly connected, thus having low permeability. Based on thin section observation, the presence of dissolution pore increases from northwest to southeast, and are most abundant in the Noelke #38 core.

Measured core plug porosity and permeability in sandstone and carbonate succession suggest moderate porosity up to 11.6%, and relative low permeability ranging from less than 0.001 md to 0.856 md (Figure 4-29). Porosity-permeability results in carbonate is relatively lower than results in sandstone succession. The highest porosity and permeability were reported in siderite-coated sandstone in the Noelke #38 core. The

siderite-coated sandstone is considered to have the best reservoir potential because of its good porosity-permeability value and its commonly presence in the study cores.

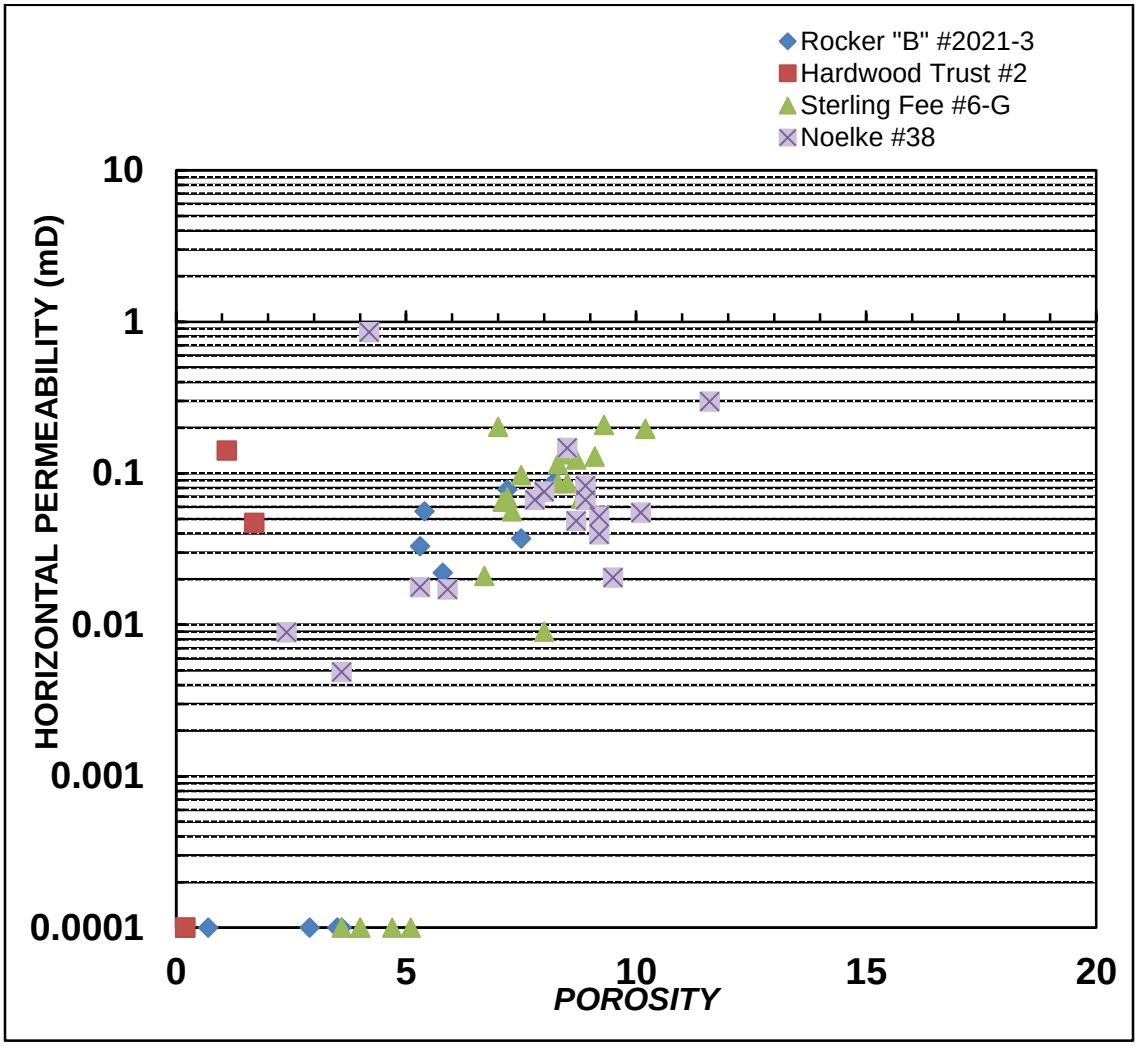

Figure 4-29: Measured core plug porosity and permeability result

The Wolfcamp mudrock succession is fair to good in organic richness (Peters, 1986). TOC varies from 0.8 wt.% to 2.6 wt.%, with an average of 1.4 wt.% (N = 48). Three types of pores have been identified based on SEM observation: interparticle pore, intraparticle pore, and organic pore. Interparticle pores are nanopores to micropores between particles (Loucks et al., 2012). It is the dominant pore type in the observed samples. Interparticle pores are commonly present between clay minerals, and they develop effective porosity (Figure 4-30B, C). Intraparticle pores are pores within particles (Loucks et al., 2012). They commonly present within silica grains in the observed samples (Figure 4-30D). Organic pore are intraparticle pores found specifically within the organic matter (Loucks et al., 2012). Organic pores are rarely present in the observed samples. They are characterized as small, bubble like shape, and are completely separate from each other (Figure 4-30D). Based on Milliken et al. (2013), these organic pores are classified as discrete spherelike organic pore, and they tend to be abundant in less mature kerogen. Evidence of rarely present discrete spherelike organic pore in the observed samples implies that the Wolfcamp mudrocks in the study area is relatively less mature. However, it is recommended that more information from kerogen type and thermal maturity measurements, and mudrock samples from different depth, locations need to be investigated.

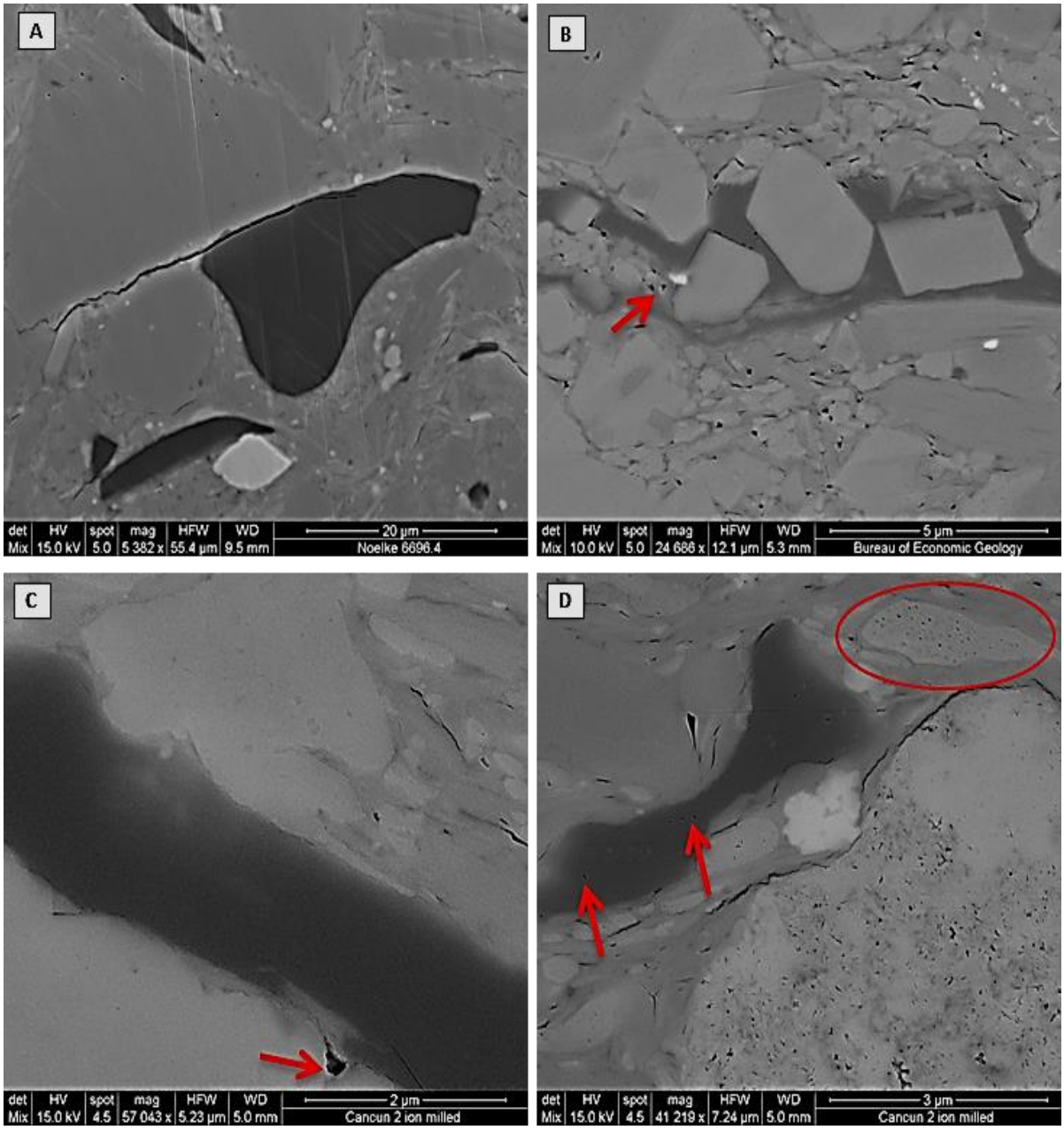

Figure 4-30: SEM images for Wolfcampian mudrock pore system. (A) SEM image of organic matter (in black), no organic pore presence, Noelke #38, 6696.4 ft. (B) SEM image of interparticle pores between clay minerals and quartz grains (arrow), Harwood Trust #2, 7697ft. (C) SEM image of interparticle pores, Harwood Trust #2, 7486.6 ft. (D) SEM images of intraparticle pores (circle) and organic pores (arrow), Harwood Trust #2, 7486.6 ft.

Discussion

Depositional setting

The Wolfcampian succession of the southeast Midland Basin is interpreted to be deposited in a deep-water slope to basinal setting. Covariation of redox indicators and TOC indicate that dysoxic to anoxic paleoceanographic conditions prevailed during deposition of mudrock intervals (Algeo and Lyons, 2006; Dahl et al., 2013). This interpretation is supported by evidence that includes enrichment of organic matter, rare bioturbation, and lack of deep-water benthic fauna.

Depositional processes for mudrock intervals include hemipelagic settling and diluted turbidite deposition; depositional processes for sandstone and carbonate intervals involve turbidity flow, debris flow, and hyperconcentrated density-flow deposits. Hemipelagic settling is interrupted by periodic gravity flows, as evidenced by incomplete Bouma sequence, soft-sediment deformation, and chaotic distribution of large skeletal grains. The periodic occurrence of shelf-derived gravity flow also disrupts the accumulation of organic matter.

Depositional cyclicity

Deposition of the Wolfcampian succession occurred during a period of high-amplitude, high-frequency eustatic sea-level fluctuation (Ross and Ross, 1987; Brown et al., 1990). Evidence of sea-level fluctuation was recorded on the Eastern Shelf with meter-scale sequences (Holterhoff, 2010). Eustatic changes can trigger changes in

nutrient levels and primary productivity rates, which, in turn, can change organic-carbon fluxes and redox conditions in the deep-water basin (Algeo and Rowe, 2012). In this study, basinal sediments were able to record evidence of high-frequency sea-level changes. Although meter-scale cyclicity is well defined from study cores within the basin, it has been difficult to make a correlation from the Eastern Shelf down to the Midland Basin because of facies lateral heterogeneity caused by periodic gravity-flow influx. There is also difficulty in recognizing fine-grained sediment cyclicity on a wireline log because of its limitations in vertical resolution. More data—such as isotope data, biostratigraphic data, and a more complete portion of the Wolfcampian period core in the study area—are needed to delineate the correlation between slope to basinal cycles and the deposited sediment on the Eastern Shelf.

TOC PRESERVATION AND RESERVOIR QUALITY

TOC is facies-dependent in Wolfcampian mudrock succession. Higher TOC tends to appear in argillaceous-dominated mudstone lithofacies such as argillaceous calcareous mudstone (Figure 4-25), and the highest TOC (N = 48) appears in argillaceous mudstone (Figure 4-26). Despite disturbance from periodic gravity flow, TOC value increases with higher productivity rate, as indicated by higher Cu, Ni, or P value. Also, the abundance of TOC increases with increasing bottom-water anoxia, as indicated by higher Mo or U value. Stratigraphic intervals present in the study core are mostly in Lower Wolfcampian (Figure 3-1). During early Wolfcampian, the final episodes of Ouachita orogeny created uplifted sediment source areas to the east and south of the Permian Basin (Ross, 1986).

This is confirmed by isopach map during Wolfcampian age by Hamlin and Baumgardner, 2012. The Wolfcamp thickens into the southeast Midland Basin, where the study area is located, as a result of large sediment influx (Hamlin and Baumgardner, 2012; Dr. H. Scott Hamlin at BEG, personal communication). Sediment influx during early Wolfcampian explains the relatively low TOC value in the study area compare to previous studies at the basin center (e.g., Baumgardner et al., 2016). But more data are needed to calculate sedimentation rate in each intervals in the early Wolfcampian. Ti/Al is not able to detect the relation between TOC and sediment influx. This is probably because the limitations in sample selection. More samples that cover different kinds of mudrock lithofacies are recommended to be investigated.

Siderite-coated sandstone is considered to be an important reservoir target in the Wolfcampian succession. Although siderite has commonly been recognized as authigenic mineral in freshwater environment, but many studies reported siderite in marine environment (e.g. Mozley, 1989; Dutton et al., 1996). According to Dutton et al., 1996, siderite grain coating was also found in Sonora Canyon sandstones (Wolfcampian) in the Val Verde Basin, which located the south of the study area. Siderite-cemented sandstone were considered as of the best reservoir quality (Dutton et al., 1996).

Conclusions

As a mixed siliciclastic and carbonate interval, the Wolfcampian unconventional succession in the southeast Midland Basin reveals great heterogeneity. Lithofacies change rapidly, from a scale of feet to inches. Based on the integration of petrographic observation and XRD data analysis, seven lithofacies in the Wolfcampian succession were defined based on sedimentary features, grain size, texture, mineral composition, and bioclast. The lithofacies include: (1) sandy siltstone, (2) argillaceous mudstone, and (3) very fine to fine sandstone as siliciclastic-dominated lithofacies; and (4) massive to weakly laminated calcareous mudstone, (5) Laminated calcareous mudstone, (6) mud-dominated bioclastic packstone/rudstone, and (7) grain-dominated bioclastic packstone-grainstone/rudstone as calcareous-dominated lithofacies. The Wolfcamp succession reveals a complex diagenetic history, including compaction, calcite and silica cementation, siderite grain coating, and dissolution.

Depositional processes include hemipelagic settling, diluted turbidity flow, turbidity flow, debris flow, and hyperconcentrated density flow deposits in a deep-water, dysoxic to anoxic paleooceanographic condition. Through integration of petrographic observation and geochemical data, high-frequency cyclicity, which indirectly records evidence of high-frequency sea-level change, is observed in meter scale. A typical cycle consists of a relatively carbonate-rich chemofacies overlain by a relatively siliclastic-rich chemofacies.

Primary pores in sandstone and carbonate rocks are rarely preserved because of significant compaction and later cementation. However, siderite grain-coating inhibits further quartz cementation of primary pore space, making the siderite-coated sandstone a potential reservoir target. Also, secondary porosity created by dissolution in both siliciclastic and calcareous-dominated intervals is of great importance for Wolfcamp reservoir potential. Mudstone facies show mostly interparticle porosity between clay minerals. Intraparticle pores and organic pores are less present. Siderite-coated sandstone is considered to have the best reservoir potential since it shows good porosity and permeability value, and is regionally continuous. The Wolfcamp mudrock succession is fairly organic rich. Based on SEM observation, organic matter is commonly present in the mudstone facies, which is fair to good in organic-matter richness (Peters, 1986). TOC varies from 0.8 wt. % to 2.6 wt. %, with an average of 1.4 % (N = 48). The enrichment of organic matter is influenced by primary productivity, bottom water anoxia, and sediment influx.

Appendix: Wolfcampian Core Description

Legend:

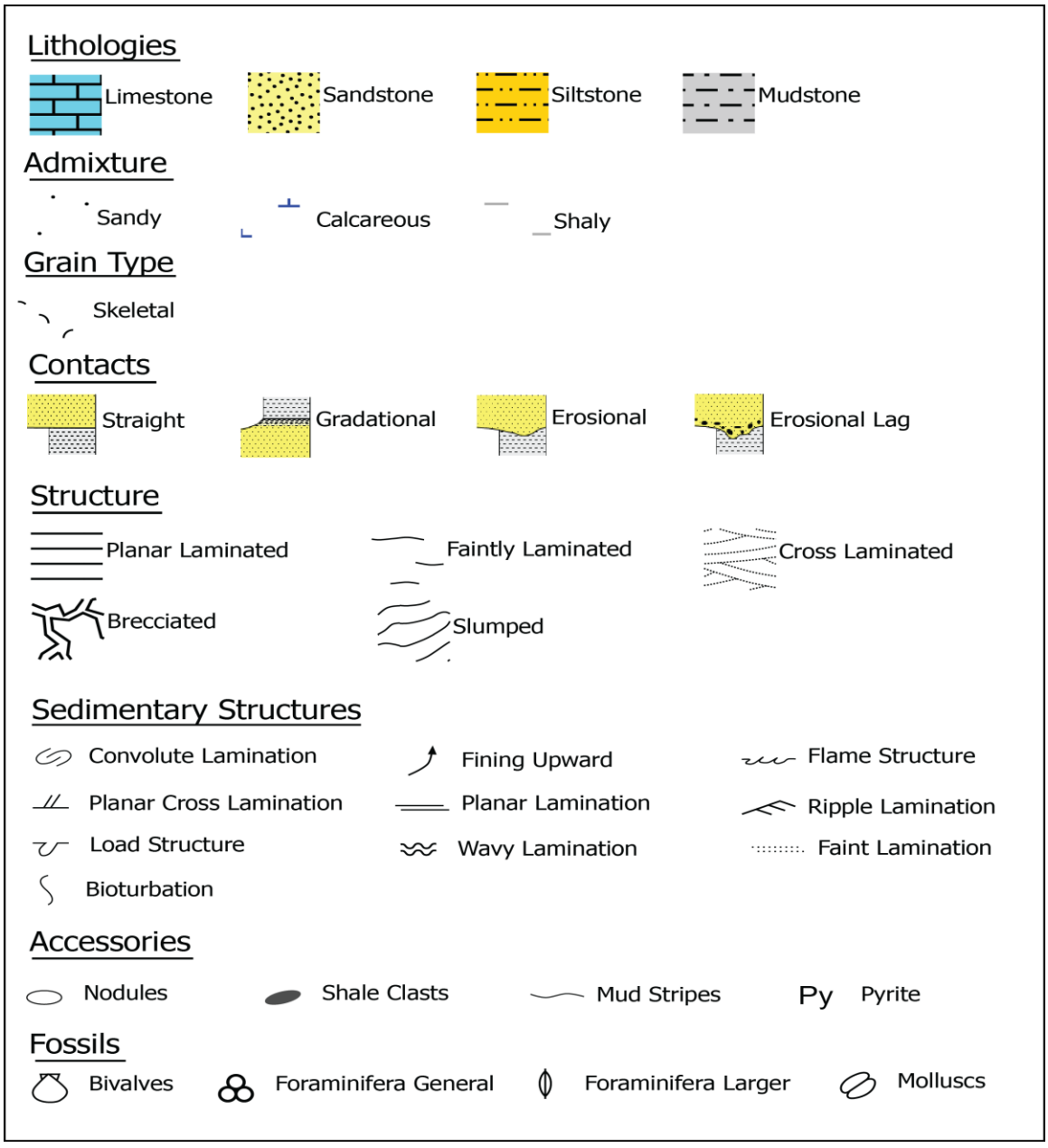

Harwood Trust #2

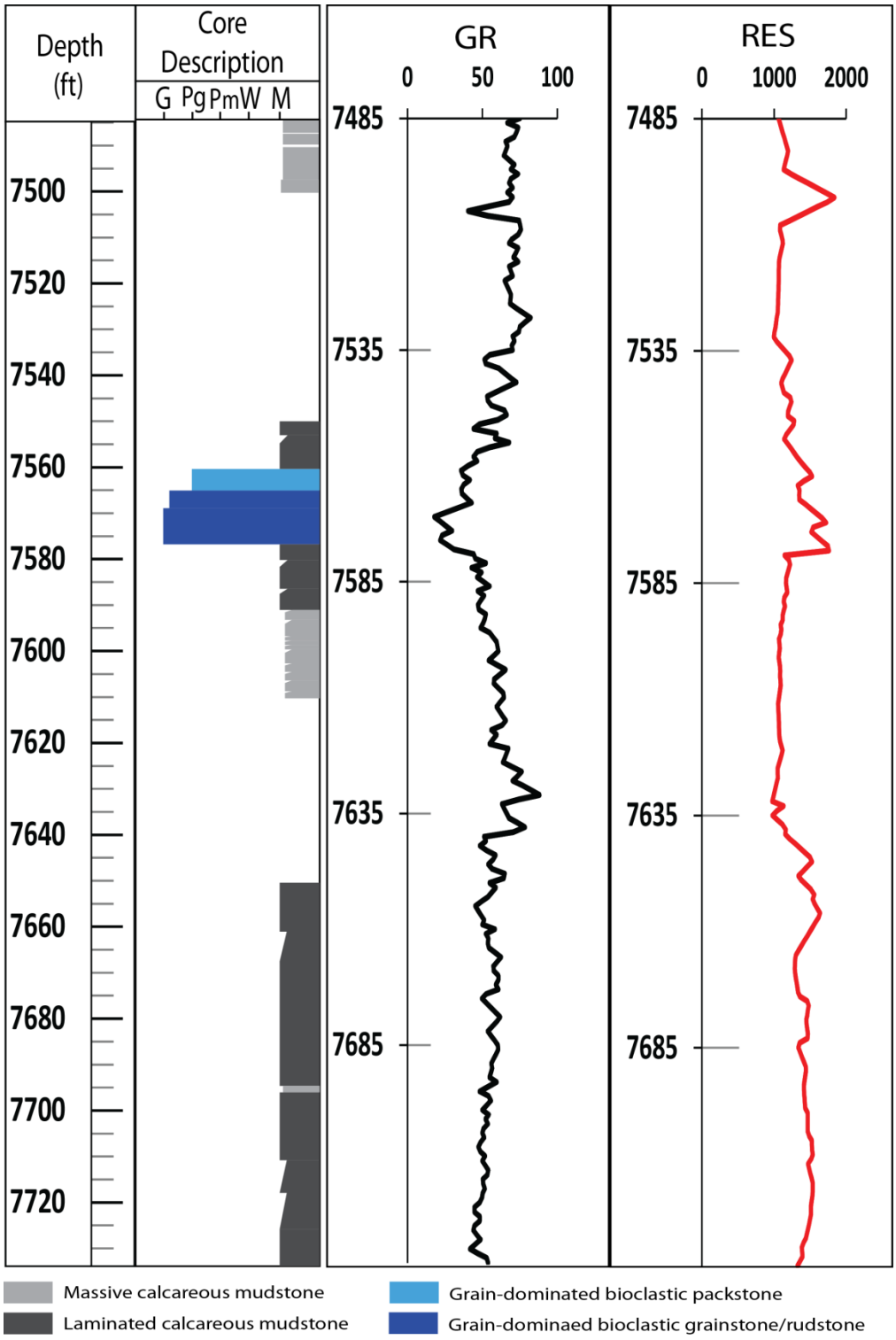

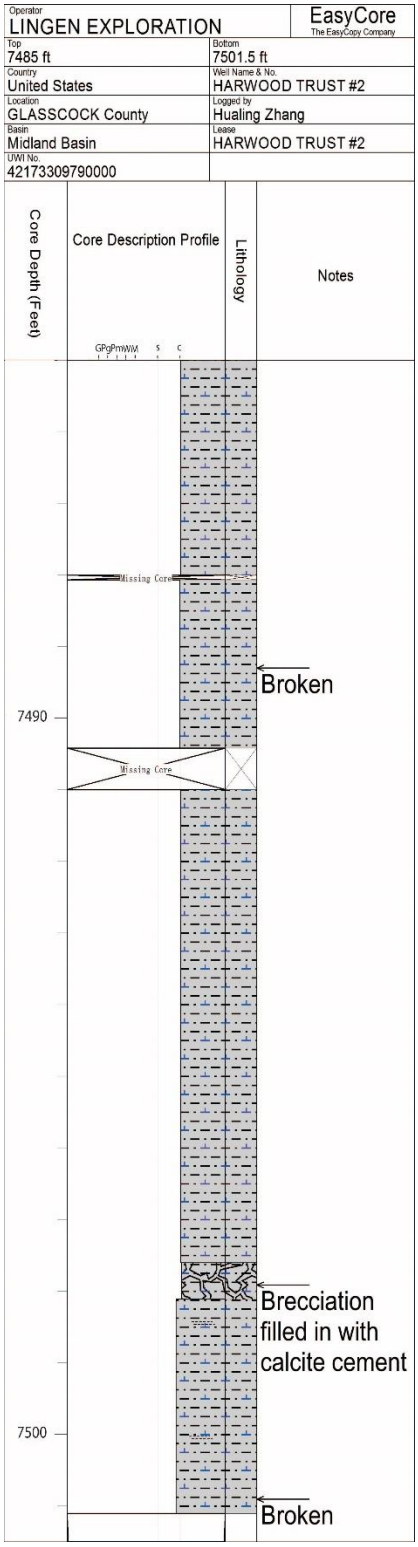
Operator
LINGEN EXPLORATION
EasyCore
The EasyCopy Company
Top
7485 ft
Bottom
7501.5 ft
Country
United States
Well Name & No.
HARWOOD TRUST #2
Location
GLASSCOCK County
Logged by
Hualing Zhang
Basin
Midland Basin
Lease
HARWOOD TRUST #2
UWI No.
42173309790000
Core Depth (Feet)
Core Description Profile
Lithology
Notes
GPgPmWM
S
C
Missing Core
Missing Core
Broken
7490
Brecciation
filled in with
calcite cement
7500
Broken

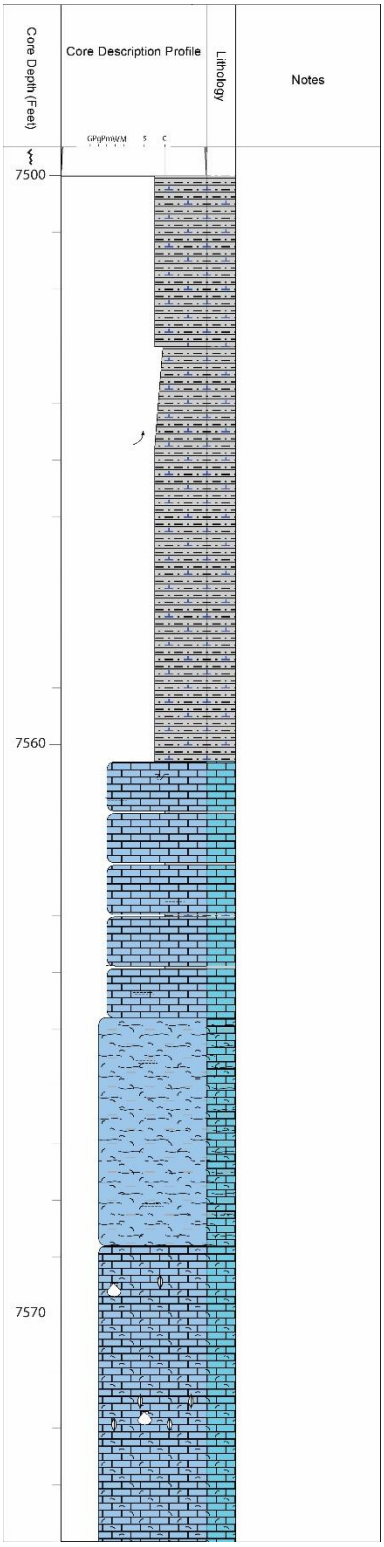
Core Depth (Feet)
Core Description Profile
Lithology
Notes
GPgPmWM
S
C
7500
7560
7570

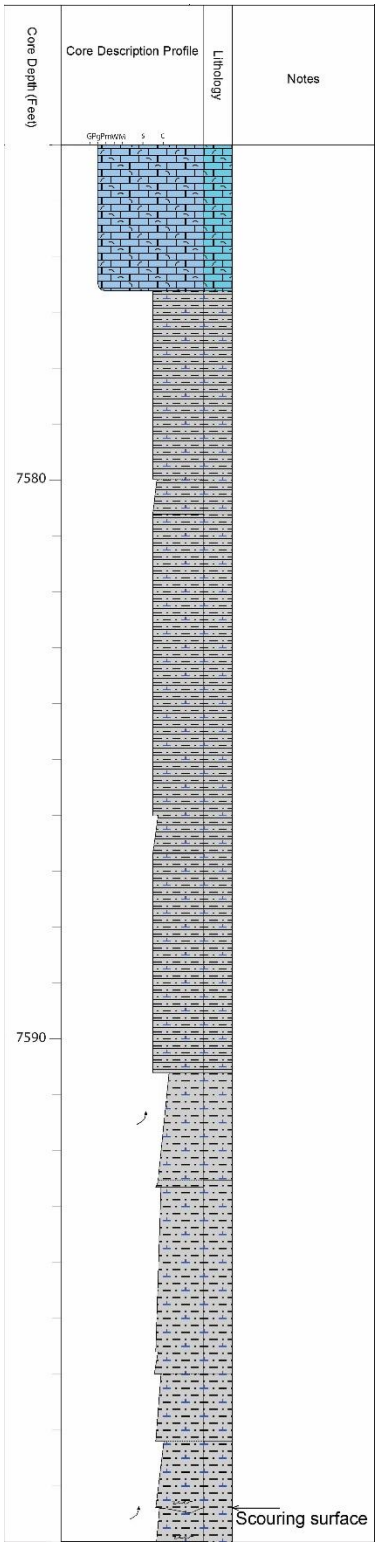
Core Depth (Feet)
Core Description Profile
Lithology
Notes
GPgPmWM
S
C
7580
7590
Scouring surface

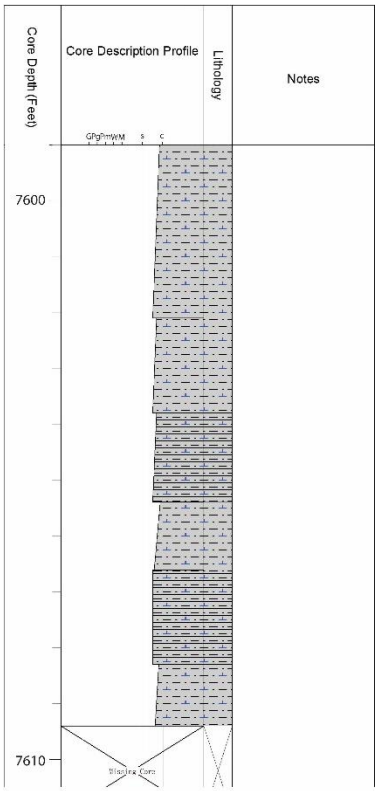
Core Depth (Feet)
Core Description Profile
Lithology
Notes
GPgPmWM
S
C
7600
7610
Sidewall Core

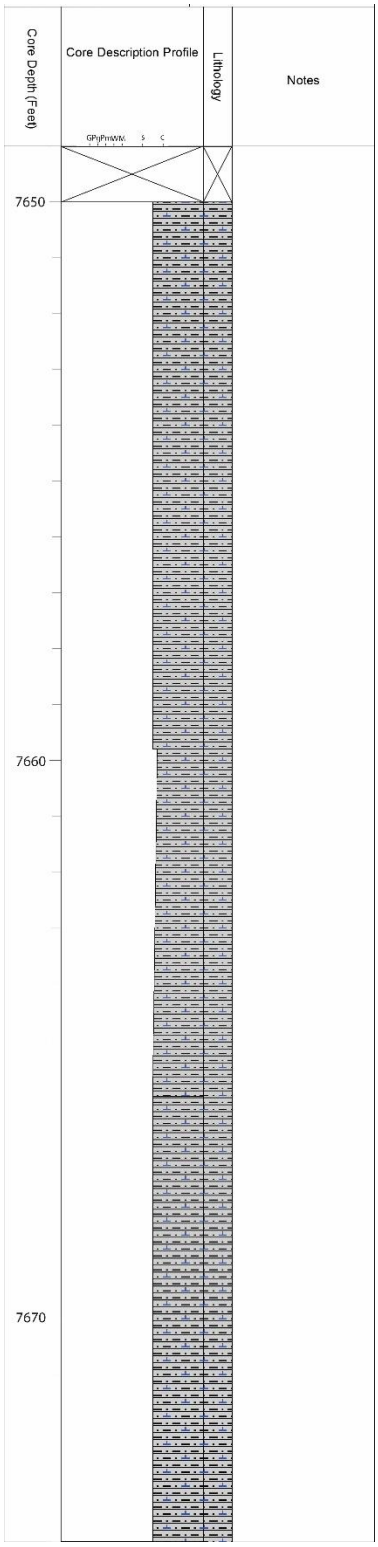
Core Depth (Feet)
Core Description Profile
Lithology
Notes
7650
7660
7670

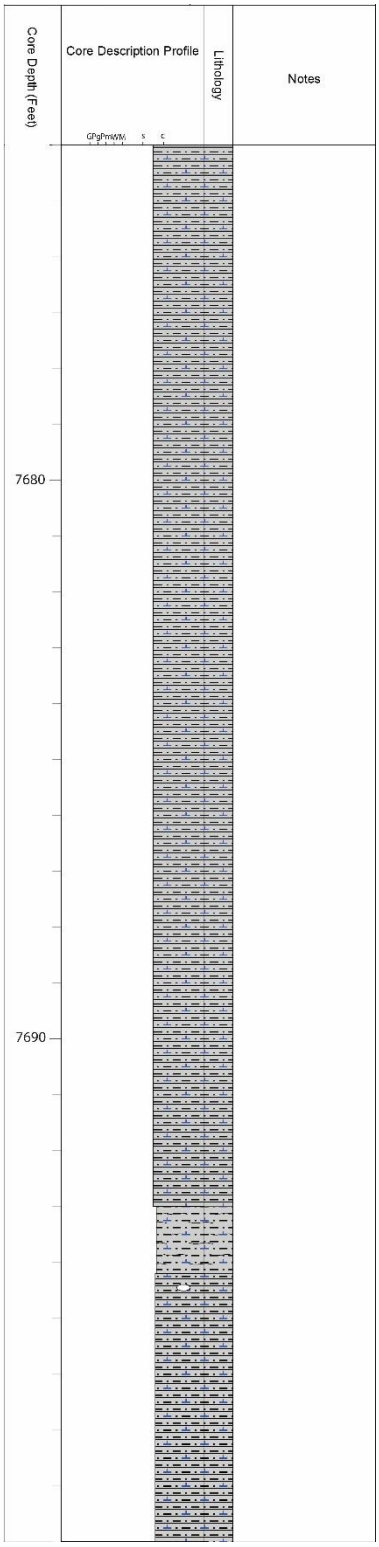
Core Depth (Feet)
Core Description Profile
Lithology
Notes
7680
7690

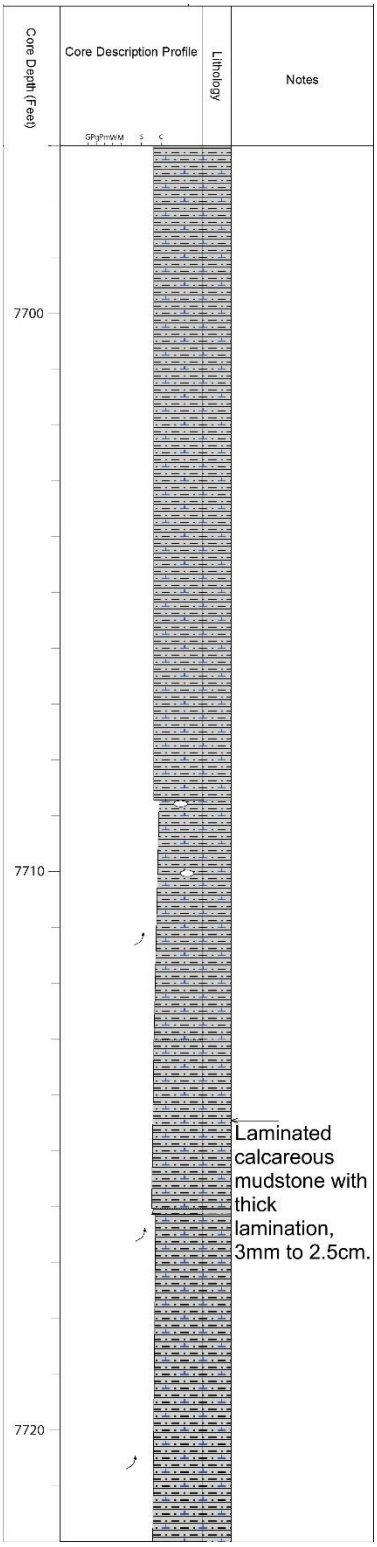
Core Depth (Feet)
Core Description Profile
Lithology
Notes
GPgPmWM
S
C
7700
7710
7720
Laminated calcareous mudstone with thick lamination, 3mm to 2.5cm.

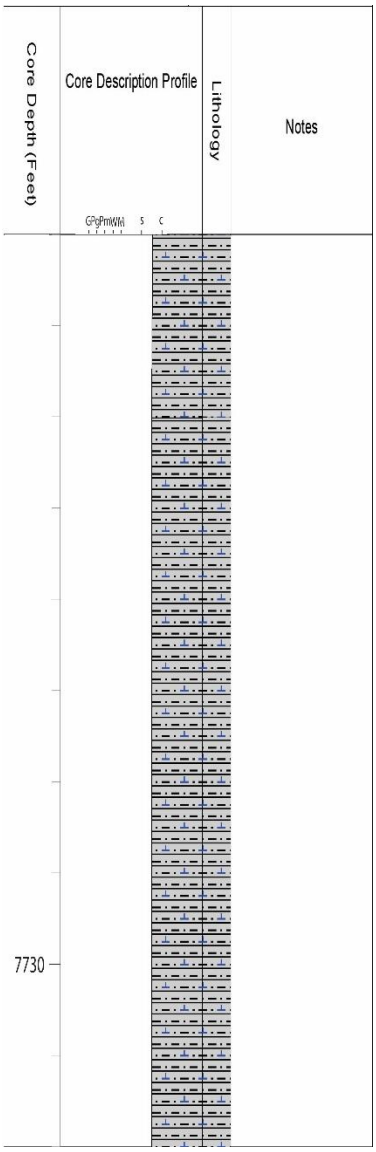
Core Depth (Feet)
Core Description Profile
Lithology
Notes
GPgPmWM
S
C
7730

Powell E.L. #1

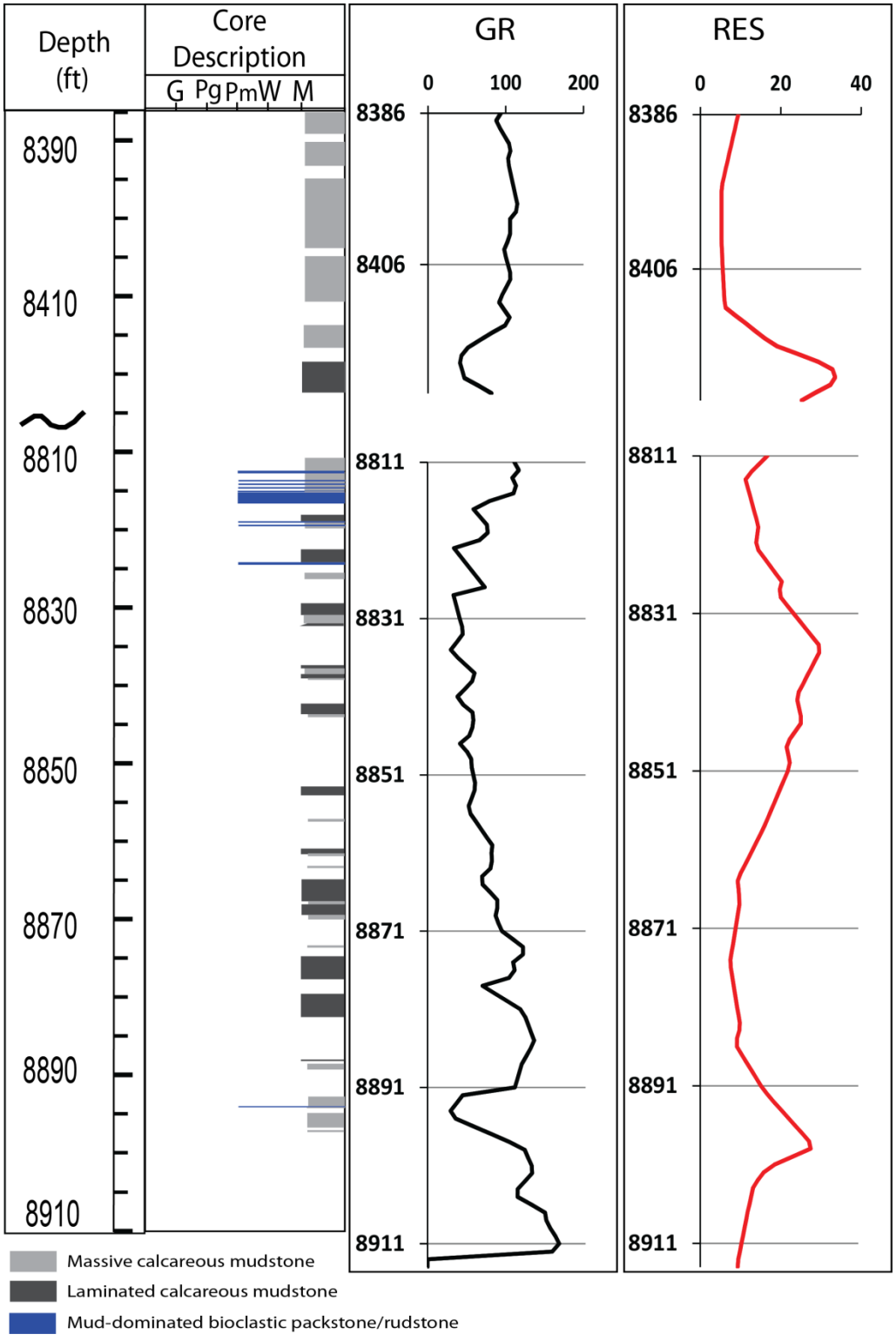
Depth (ft)
Core Description
G Pg PmW M
GR
0 100 200
RES
0 20 40
8386
8406
8811
8831
8851
8871
8891
8911
8390
8410
8810
8830
8850
8870
8890
8910
Massive calcareous mudstone
Laminated calcareous mudstone
Mud-dominated bioclastic packstone/rudstone

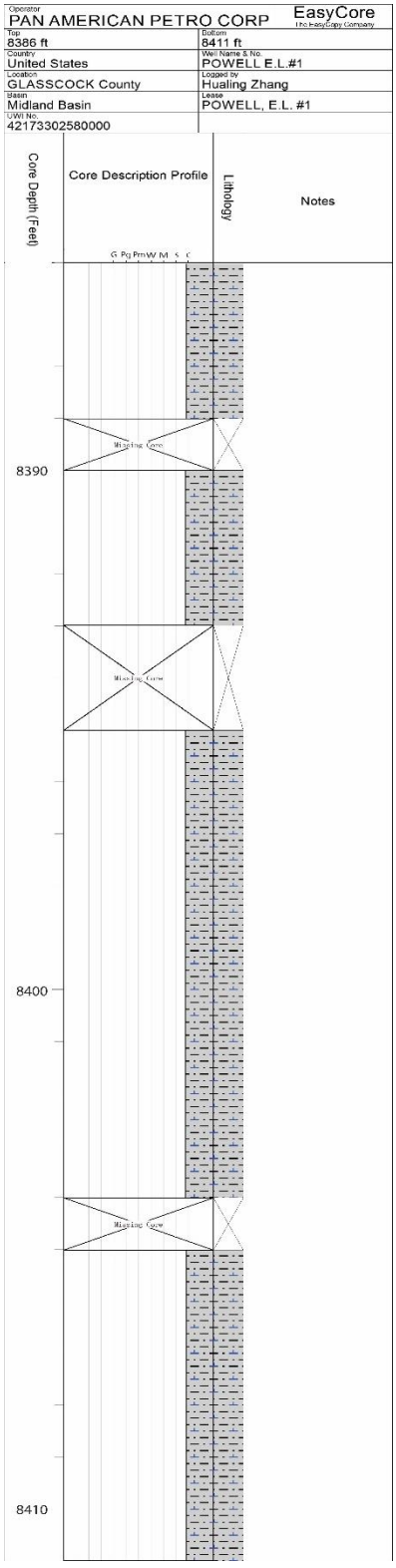
Operator
PAN AMERICAN PETRO CORP
EasyCore
Top
8386 ft
Bottom
8411 ft
Country
United States
Well Name & No.
POWELL E.L.#1
Location
GLASSCOCK County
Logged by
Hualing Zhang
Basin
Midland Basin
Lease
POWELL, E.L. #1
UWI No.
42173302580000
Core Depth (Feet)
Core Description Profile
G Pg PmW M S C
Lithology
Notes
Missing Core
Missing Core
Missing Core
8390
8400
8410

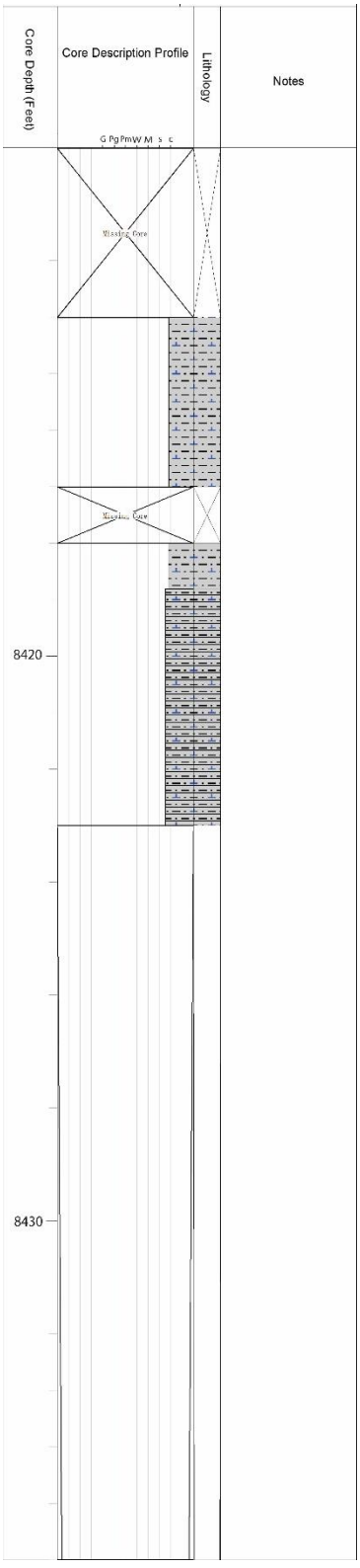
Core Depth (Feet)
Core Description Profile
G Pg PmW M S C
Lithology
Notes
Missing Core
Missing Core
8420
8430

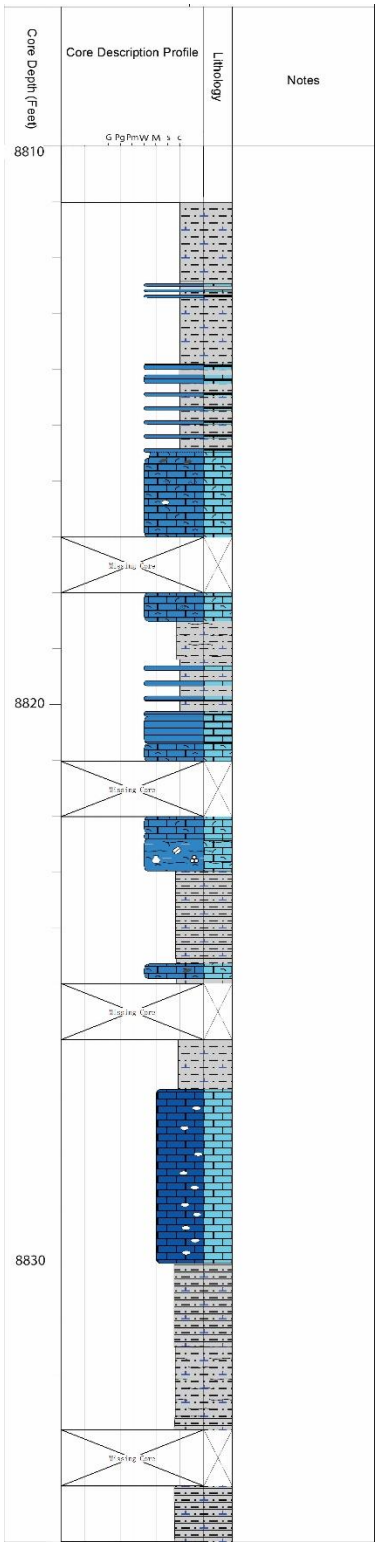
Core Depth (Feet)
Core Description Profile
Lithology
Notes
G Pg Pm W M S C
8810
8820
8830
Wireline Core

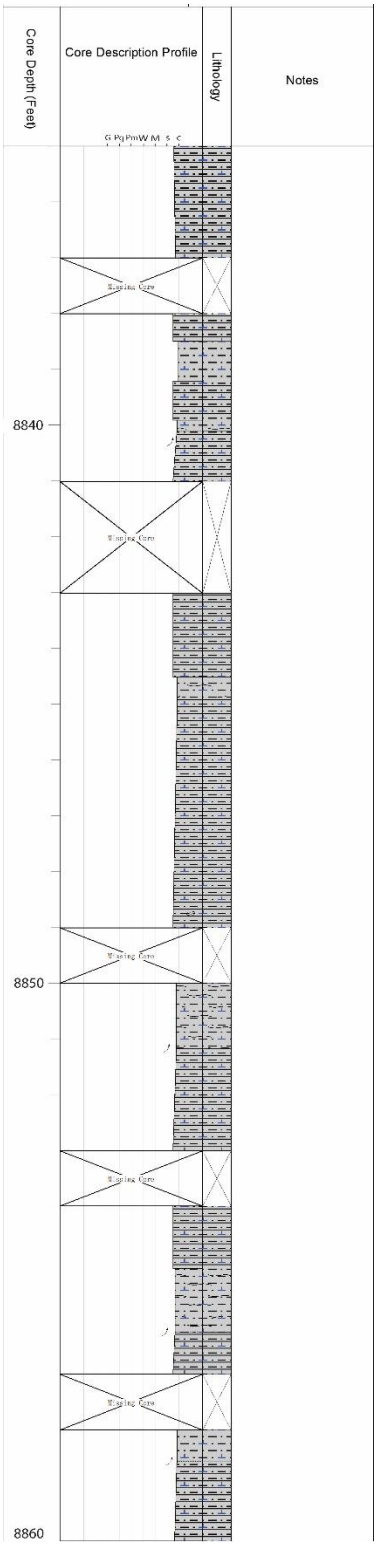
Core Depth (Feet)
Core Description Profile
Lithology
Notes
G Pg Pm W M S C
8840
8850
8860
Wireline Core

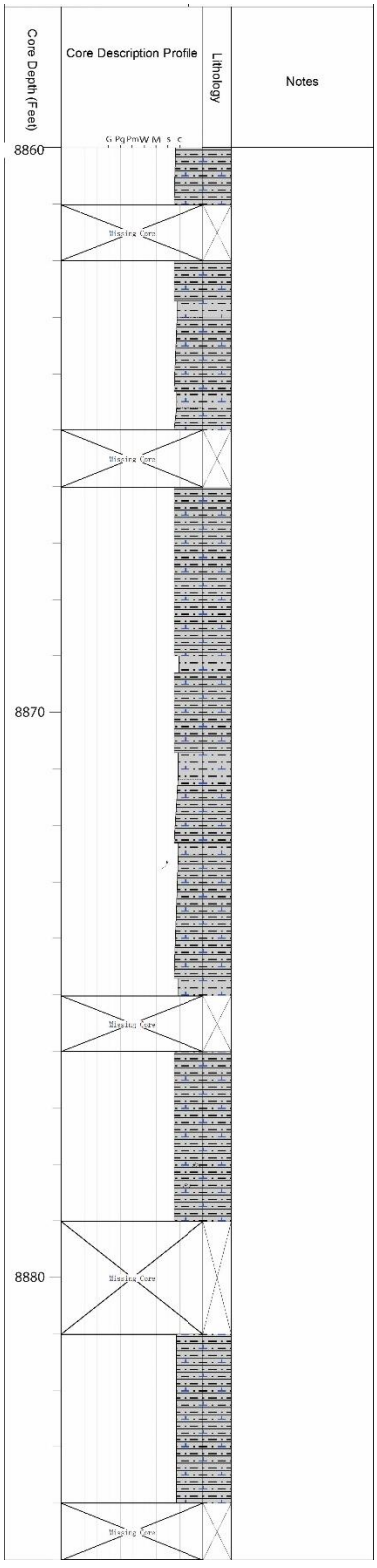
Core Depth (Feet)
Core Description Profile
Lithology
Notes
8860
8870
8880
Missing Core

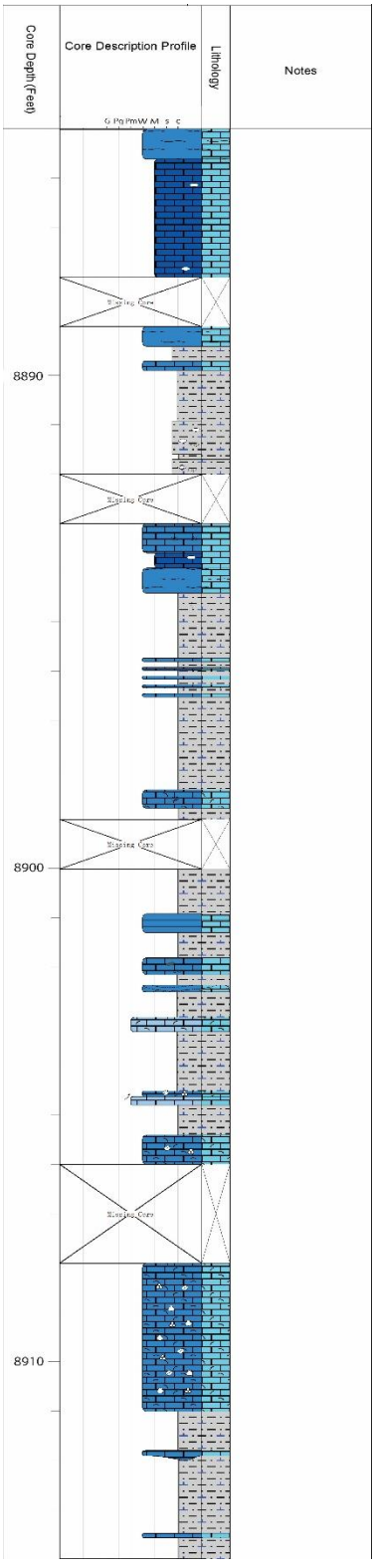
Core Depth (Feet)
Core Description Profile
Lithology
Notes
8890
8900
8910
Missing Core

Noelke #38

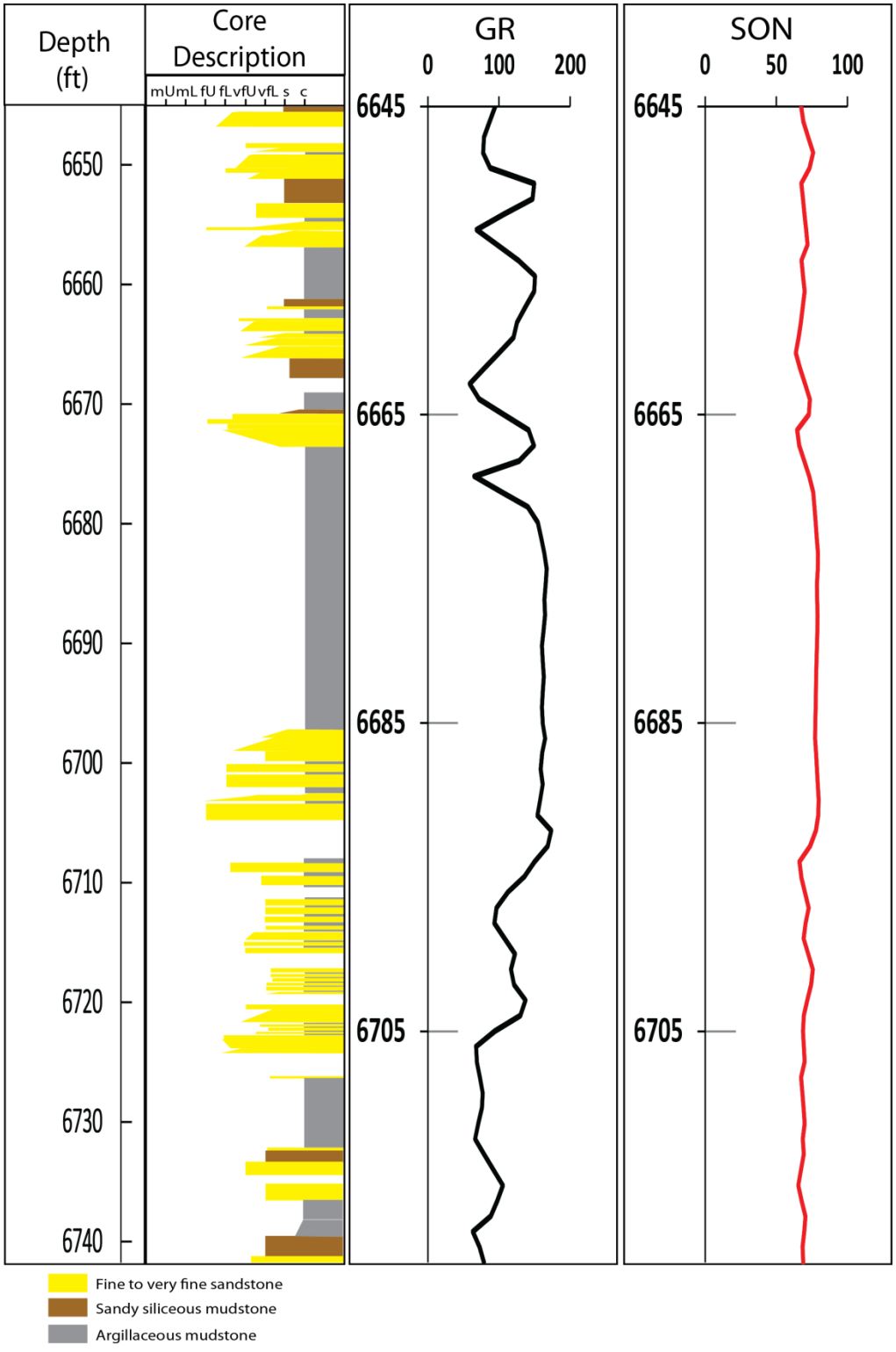
Depth (ft)
Core Description
mU mL fU fL vfU vfL s c
6650
6660
6670
6680
6690
6700
6710
6720
6730
6740
GR
0 100 200
6645
6665
6685
6705
SON
0 50 100
6645
6665
6685
6705
Fine to very fine sandstone
Sandy siliceous mudstone
Argillaceous mudstone

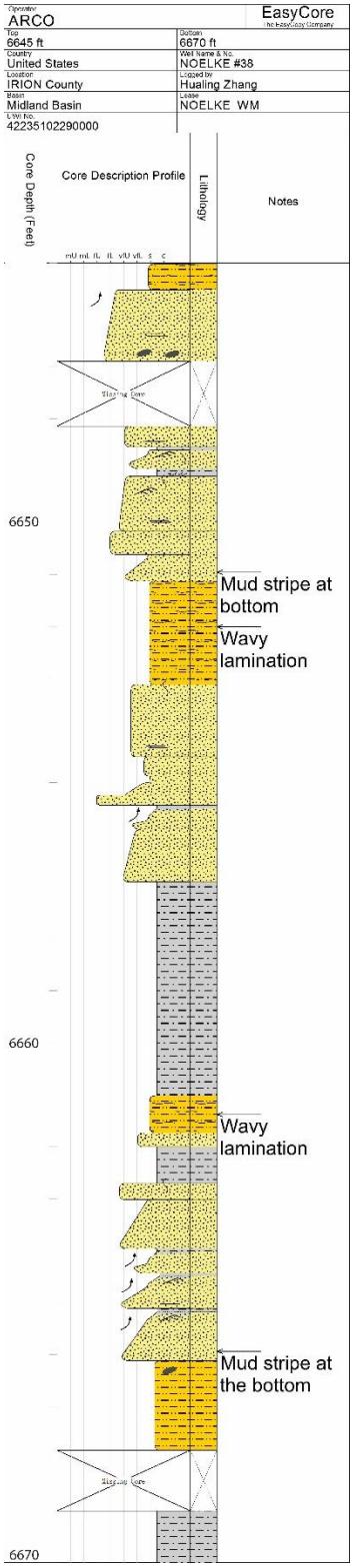
Operator
ARCO
EasyCore
Top
6645 ft
Bottom
6670 ft
Country
United States
Well Name & No.
NOELKE #38
Location
IRION County
Logged by
Hualing Zhang
Basin
Midland Basin
Leader
NOELKE WM
UWI No.
42235102290000
Core Depth (Feet)
Core Description Profile
Lithology
Notes
mU mL fU fL vfU vfL s c
6650
6660
6670
Mud stripe at bottom
Wavy lamination
Wavy lamination
Mud stripe at the bottom

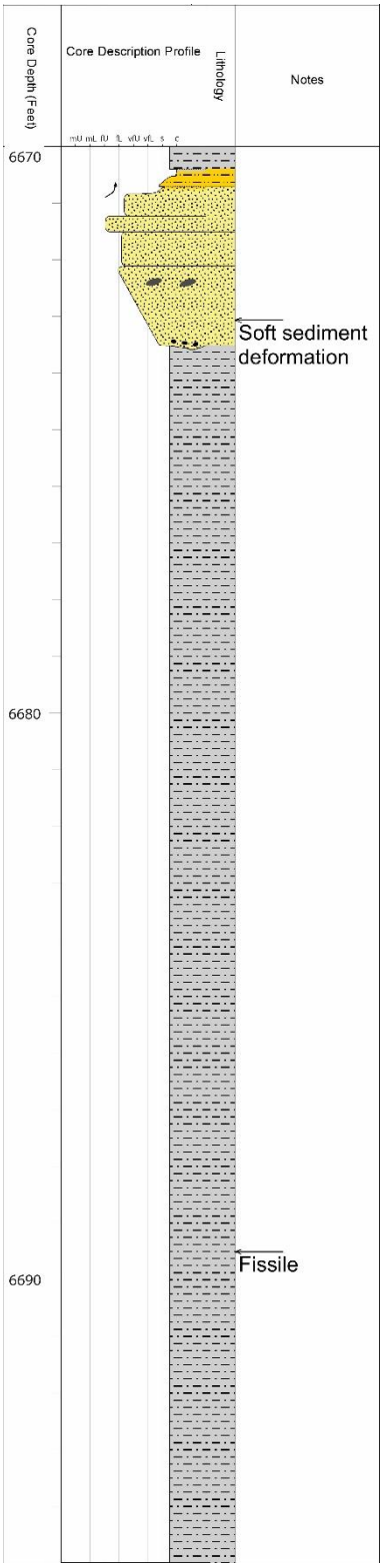
Core Depth (Feet)
Core Description Profile
Lithology
Notes
mU mL fU fL vfU vfL s c
6670
6680
6690
Soft sediment deformation
Fissile

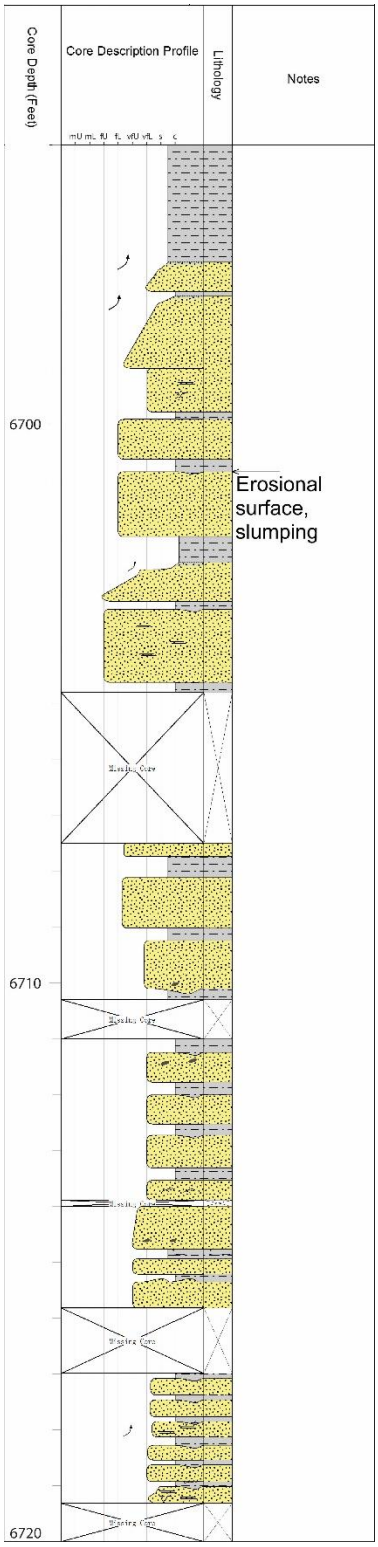
Core Depth (Feet)
Core Description Profile
Lithology
Notes
6700
6710
6720
Erosional surface, slumping

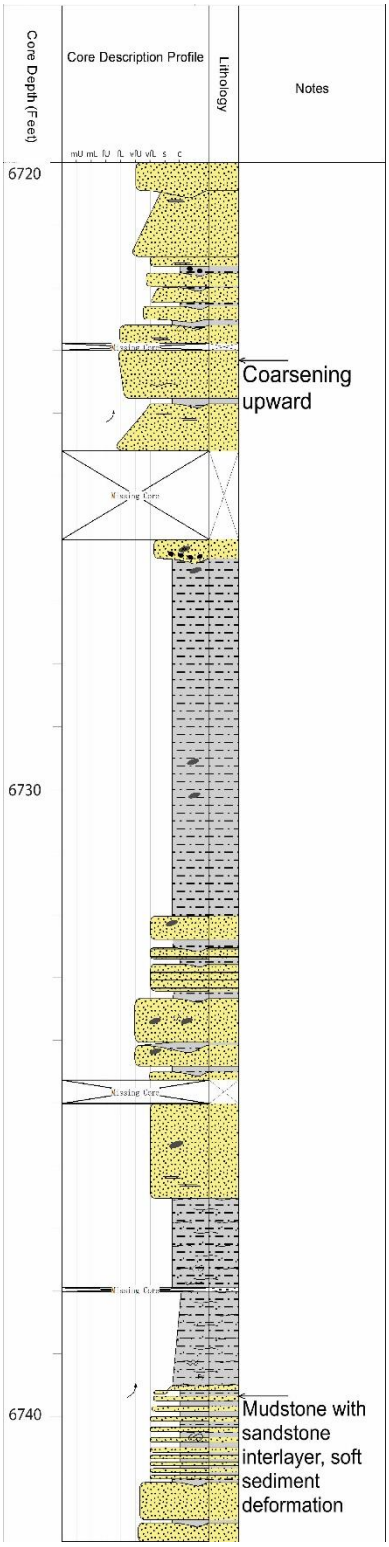
Core Depth (Feet)
Core Description Profile
Lithology
Notes
6720
6730
6740
Coarsening upward
Mudstone with sandstone interlayer, soft sediment deformation

Rocker “B” #3031-3

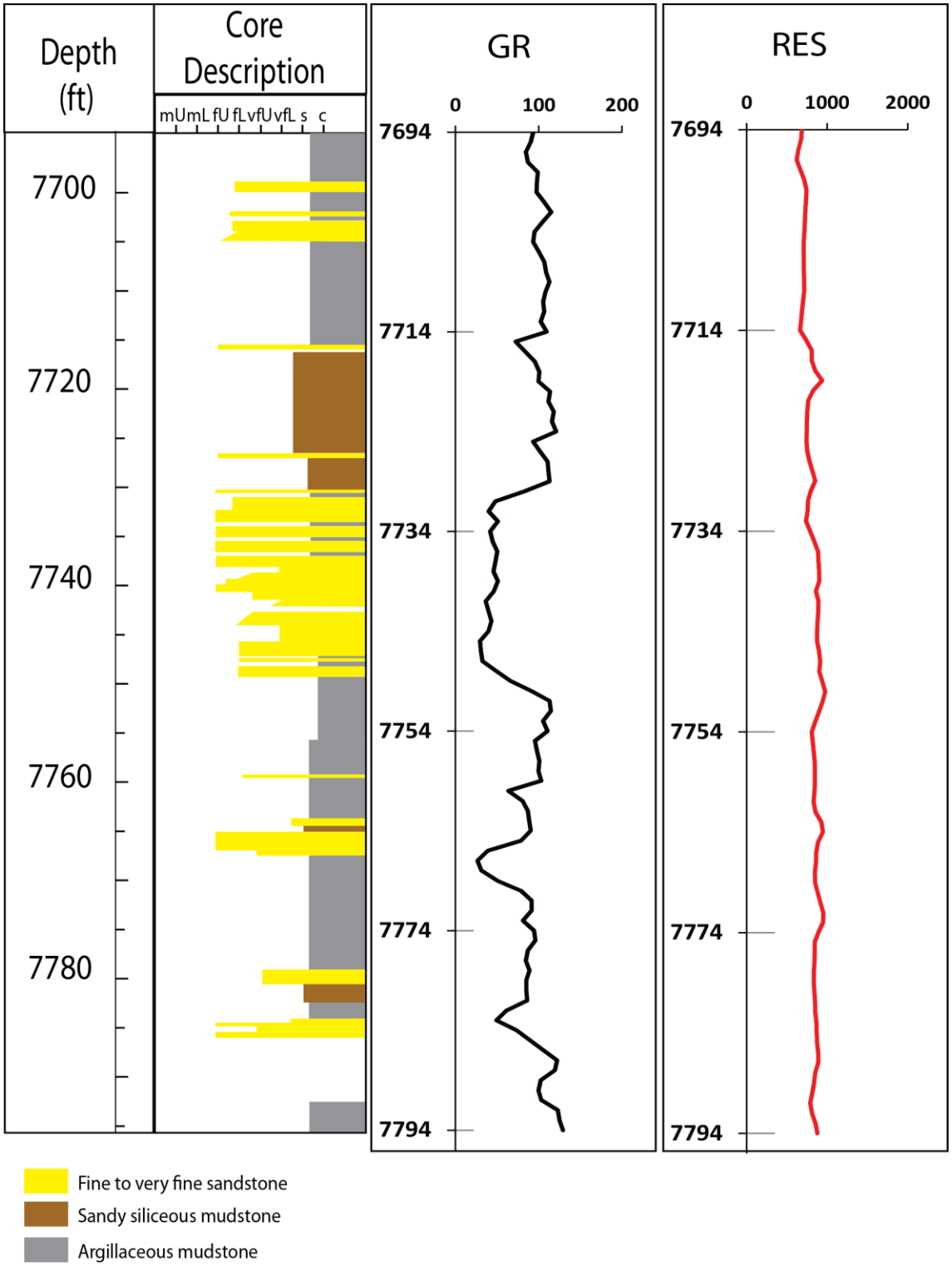

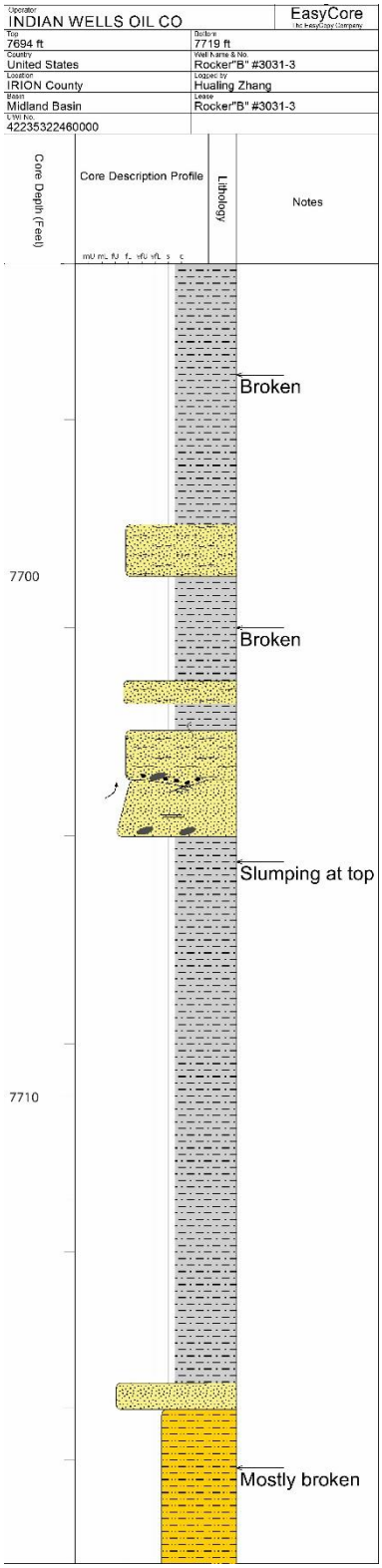
Operator
INDIAN WELLS OIL CO
EasyCore
Top
7694 ft
Bottom
7719 ft
Country
United States
Well Name & No.
Rocker"B" #3031-3
Location
IRION County
Logged by
Hualing Zhang
Basin
Midland Basin
Lease
Rocker"B" #3031-3
UWI No.
42235322460000
Core Depth (Feet)
Core Description Profile
Lithology
Notes
7700
7710
Broken
Broken
Slumping at top
Mostly broken

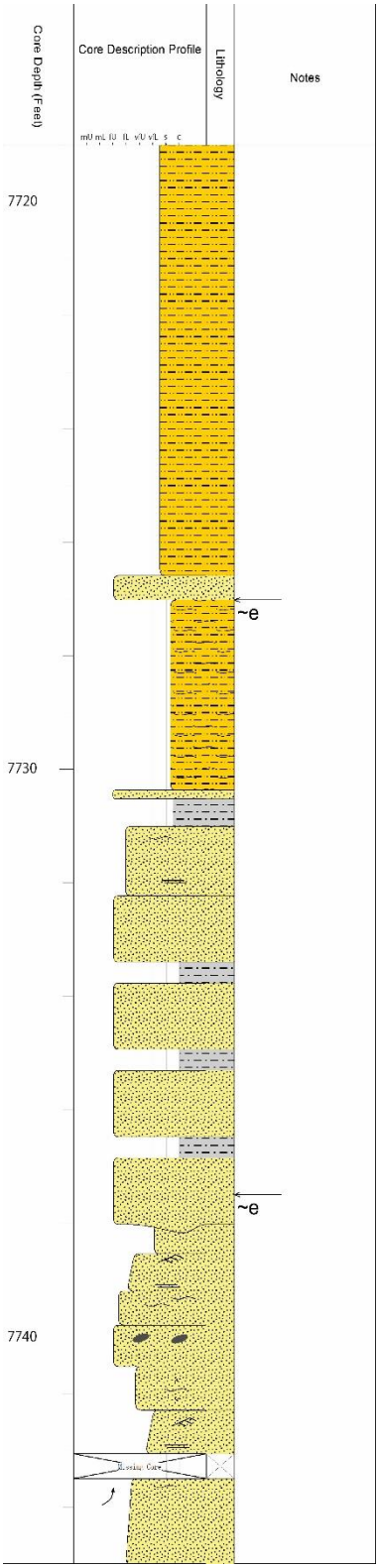
Core Depth (Feet)
Core Description Profile
Lithology
Notes
7720
7730
7740
~e
~e

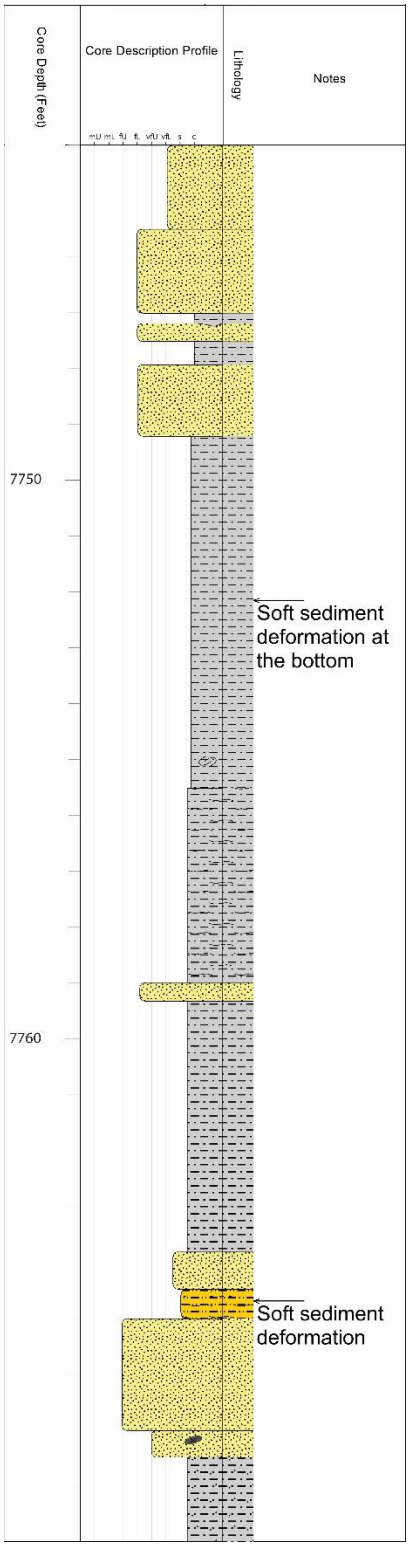
Core Depth (Feet)
Core Description Profile
Lithology
Notes
7750
7760
Soft sediment deformation at the bottom
Soft sediment deformation

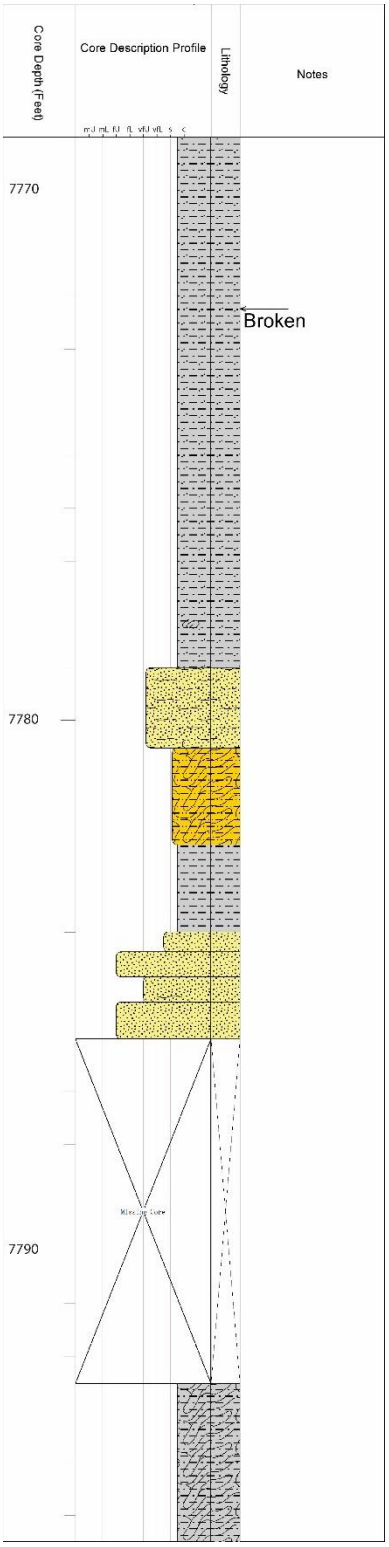
Core Depth (Feet)
Core Description Profile
Lithology
Notes
7770
7780
7790
Broken

State University #1-EM

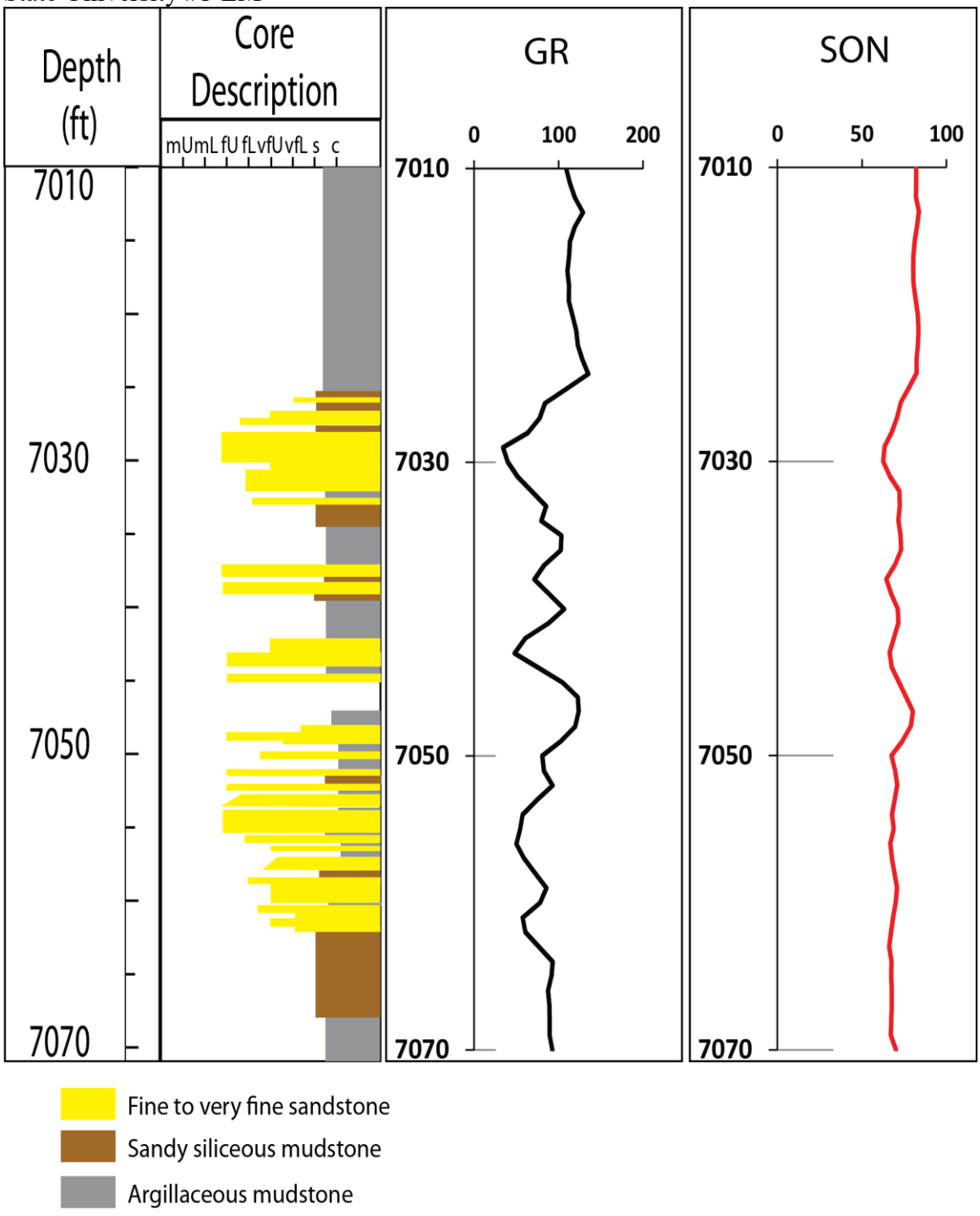

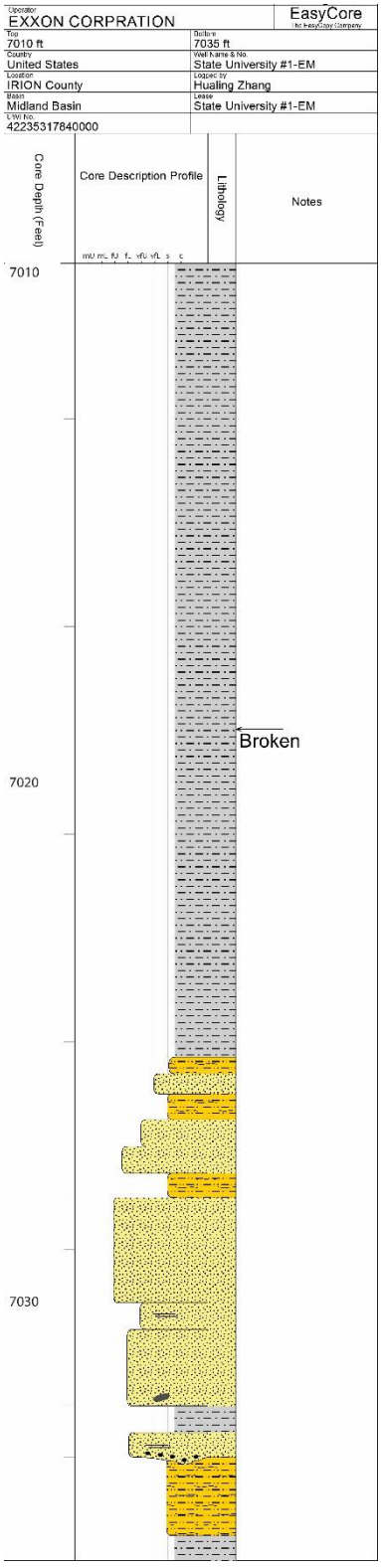
Operator
EXXON CORPRATION
EasyCore
Top
7010 ft
Bottom
7035 ft
Country
United States
Well Name & No.
State University #1-EM
Location
IRION County
Logged by
Hualing Zhang
Basin
Midland Basin
Lease
State University #1-EM
UWI No.
42235317840000
Core Depth (Feet)
Core Description Profile
Lithology
Notes
7010
7020
7030
Broken

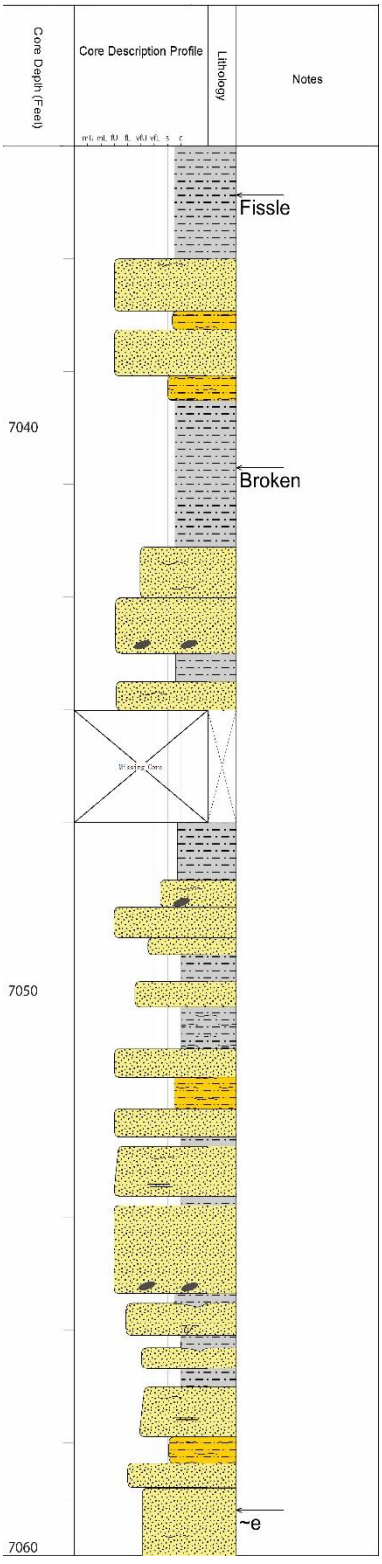
Core Depth (Feet)
Core Description Profile
Lithology
Notes
Fissle
7040
Broken
7050
~e
7060

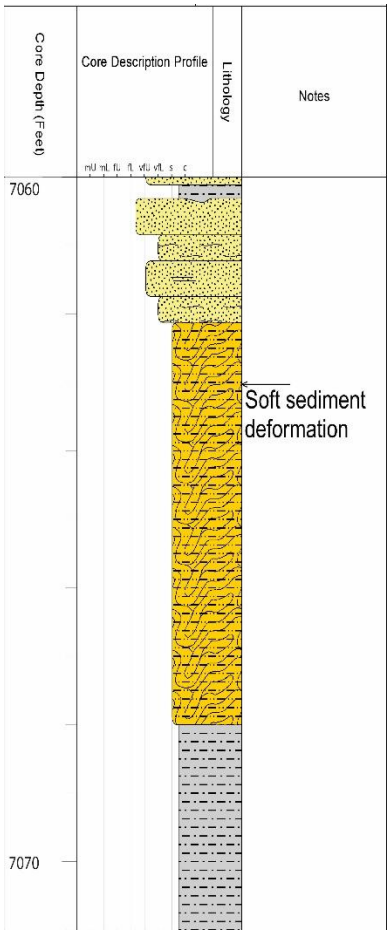
Core Depth (Feet)
Core Description Profile
Lithology
Notes
7060
7070
Soft sediment deformation

Sterling Fee #6-G

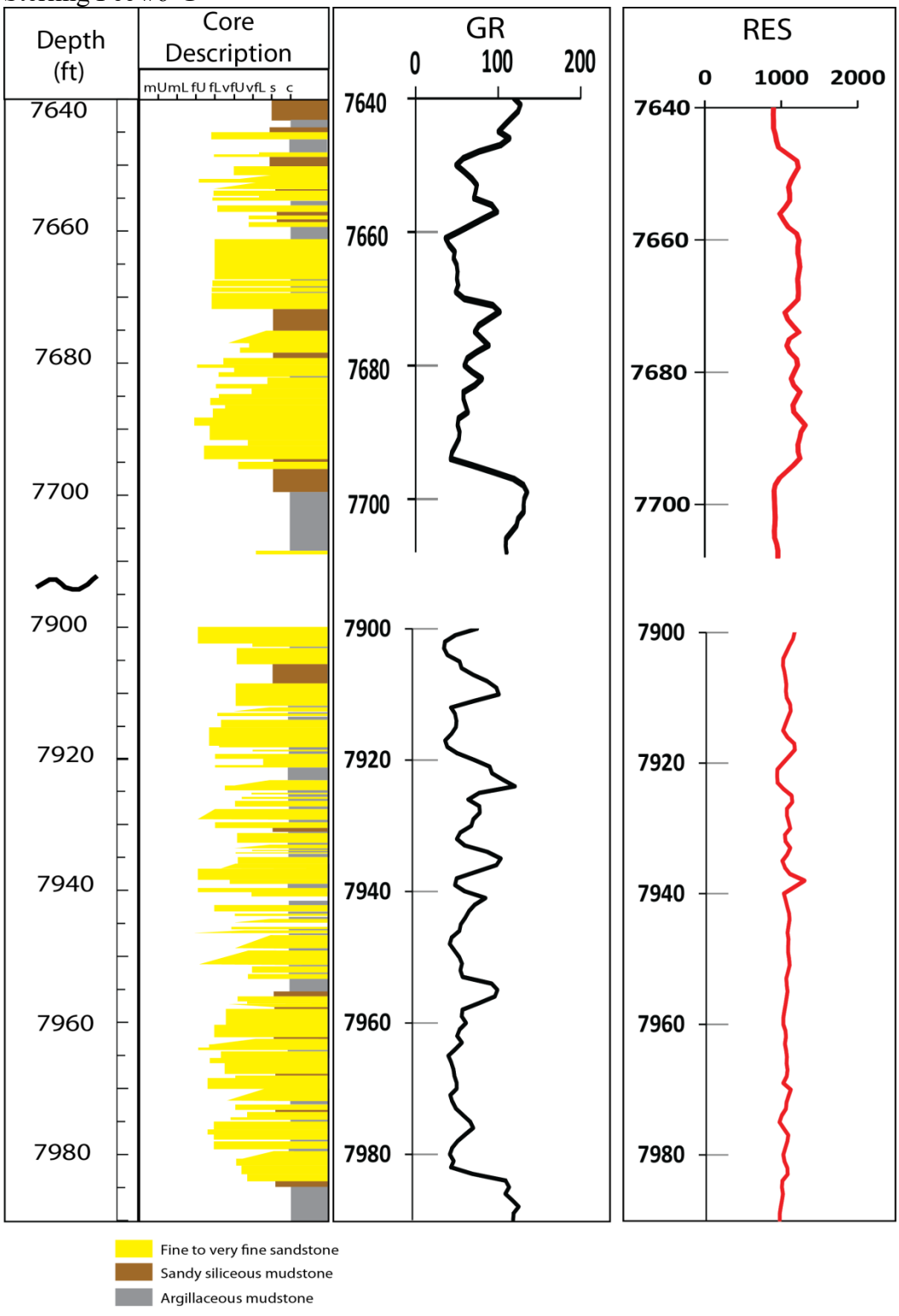

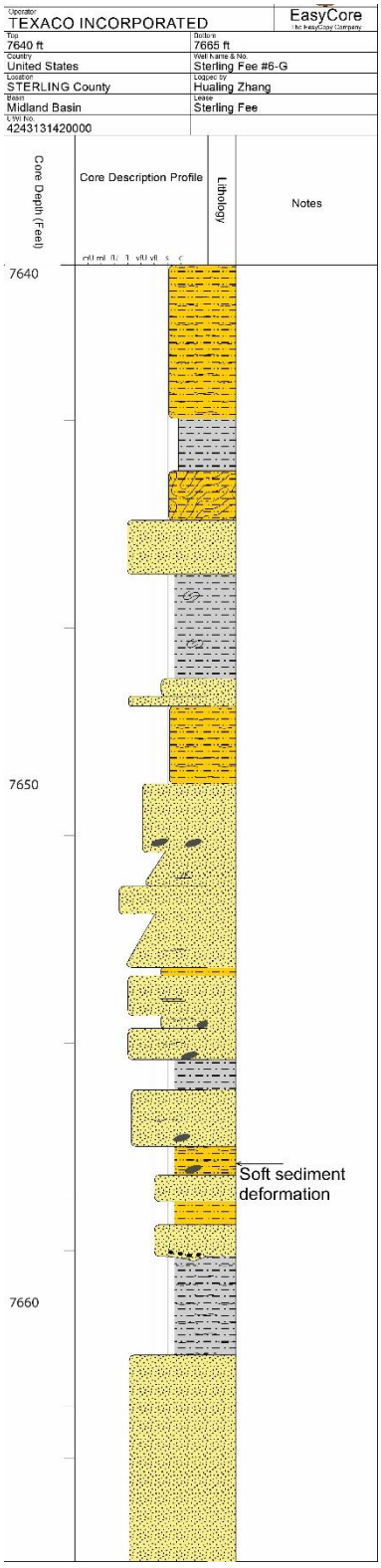
Operator
TEXACO INCORPORATED
EasyCore
Top
7640 ft
Bottom
7665 ft
Country
United States
Well name & No.
Sterling Fee #6-G
Location
STERLING County
Logged by
Hualing Zhang
Basin
Midland Basin
Lease
Sterling Fee
API No.
4243131420000
Core Depth (Feet)
Core Description Profile
Lithology
Notes
7640
7650
7660
Soft sediment deformation

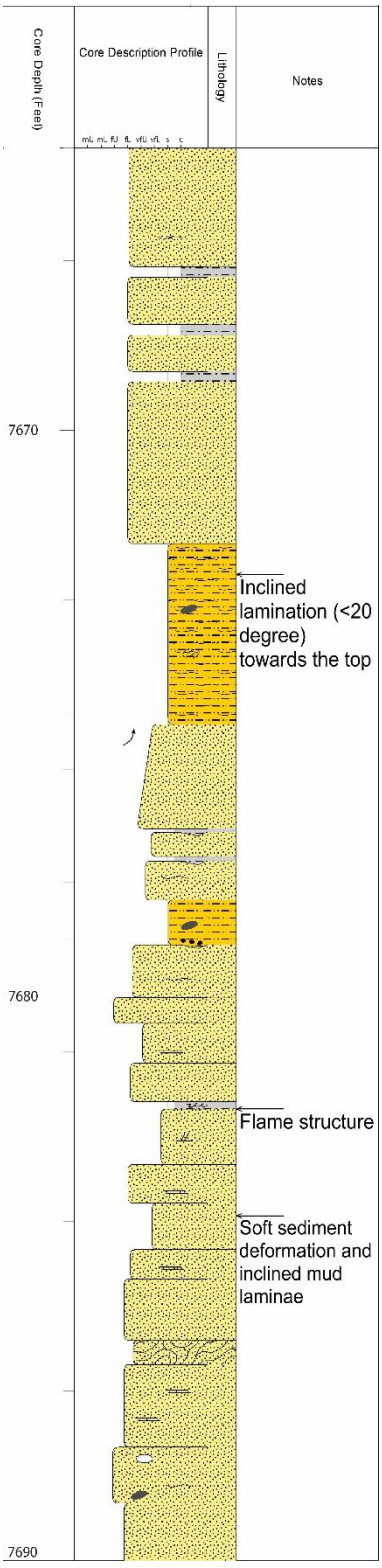
Core Depth (Feet)
Core Description Profile
Lithology
Notes
7670
7680
7690
Inclined lamination (<20 degree) towards the top
Flame structure
Soft sediment deformation and inclined mud laminae

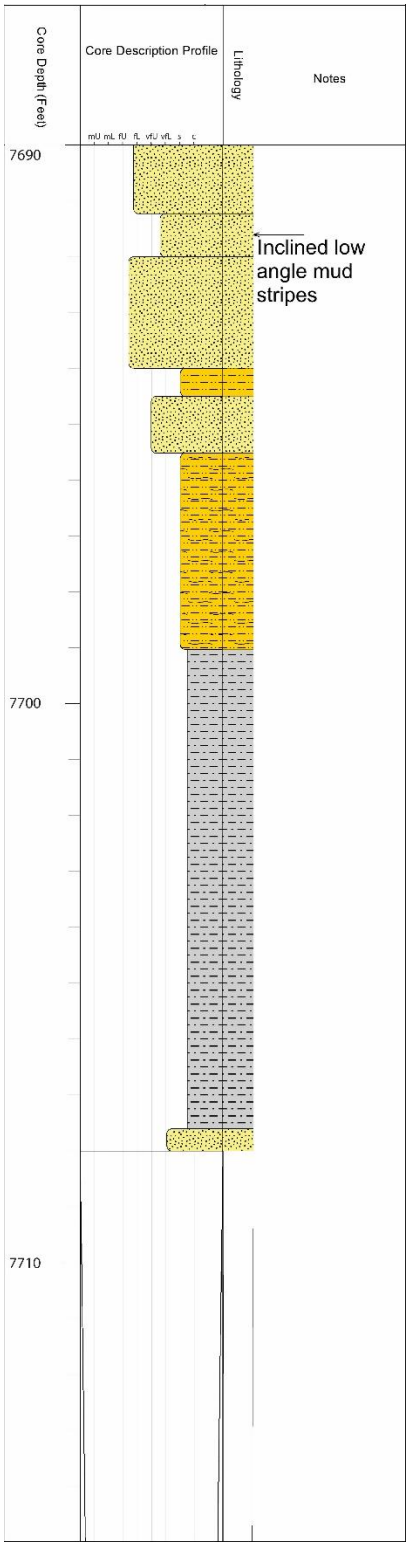
Core Depth (Feet)
Core Description Profile
Lithology
Notes
7690
7700
7710
Inclined low angle mud stripes

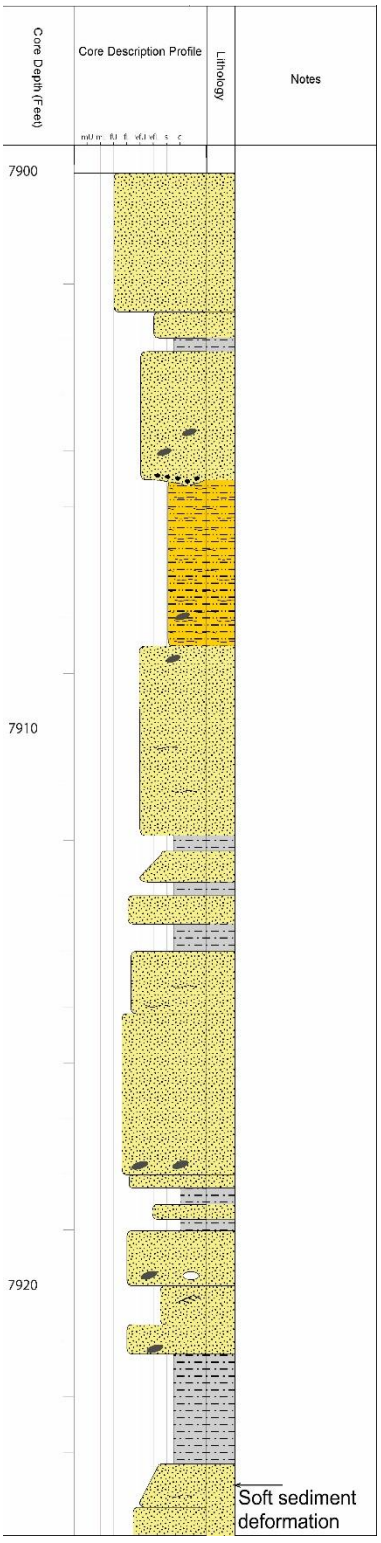
Core Depth (Feet)
Core Description Profile
Lithology
Notes
7900
7910
7920
Soft sediment deformation

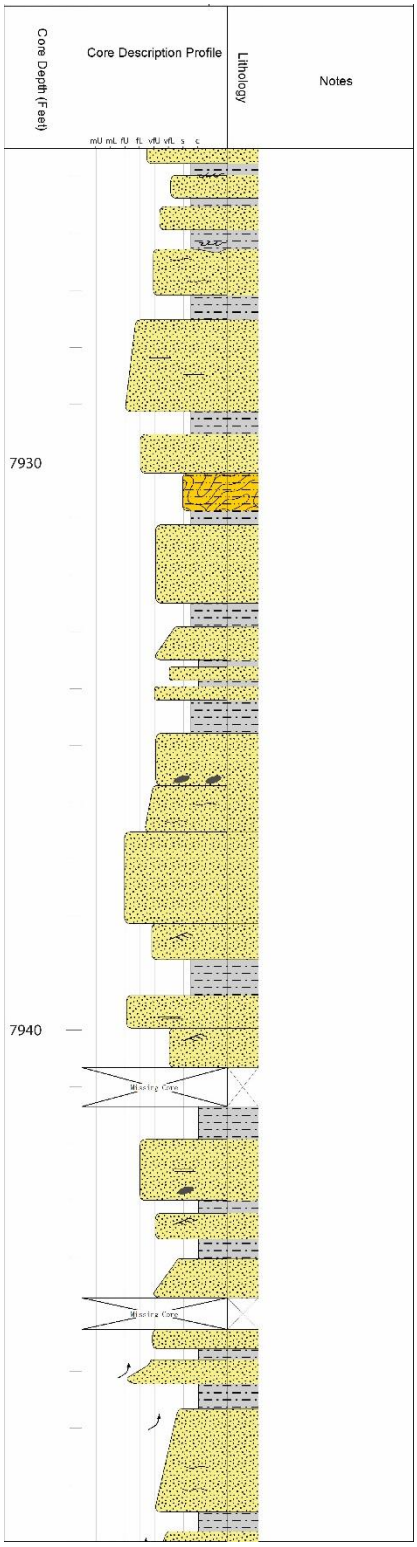
Core Depth (Feet)
Core Description Profile
Lithology
Notes
mU mL fU fL vfU vfL s c
7930
7940
Missing Core
Missing Core

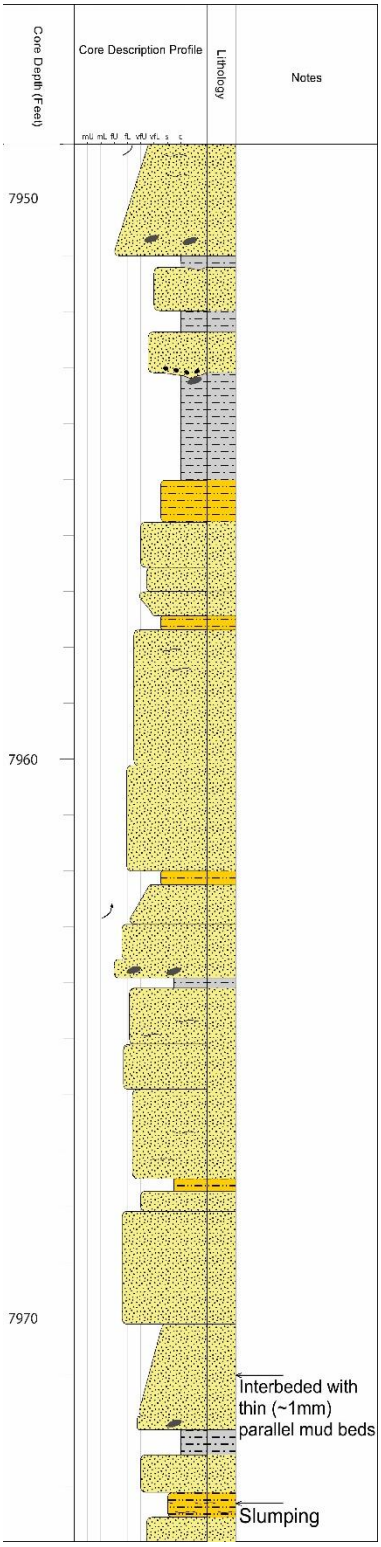
Core Depth (Feet)
Core Description Profile
Lithology
Notes
mU mL fU fL vfU vfL s c
7950
7960
7970
Interbeded with thin (~1mm) parallel mud beds
Slumping

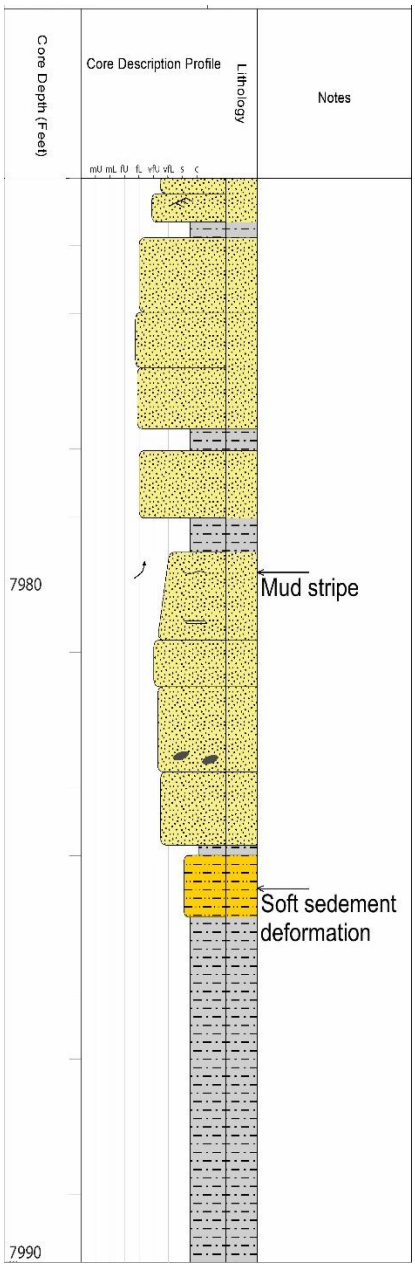
Core Depth (Feet)
Core Description Profile
Lithology
Notes
mU mL fU fL vfU vfL S C
7980
Mud stripe
Soft sedement deformation
7990

References

Algeo, T.J., Lyons, T.W., Blakey, R.C. and Over, D.J., 2007. Hydrographic conditions of the Devono–Carboniferous North American Seaway inferred from sedimentary Mo–TOC relationships. Palaeogeography, Palaeoclimatology, Palaeoecology, 256(3), pp.204-230.

Algeo, T.J. and Rowe, H., 2012. Paleoceanographic applications of trace-metal concentration data. Chemical Geology, 324, pp.6-18.

Arthur, M.A., Sageman, B.B., 1994. Marine black shales: a review of depositional mechanisms and significance of ancient deposits. Annu. Rev. Earth Planet. Sci. 22, 499–551.

Ball, M. M., 1995, Permian Basin Province (044): US Geological Survey, <http://certmapper.cr.usgs.gov/data/noga95/prov44/text/prov44.pdf>, accessed March 2016.

Baumgardner, R. W., Hamlin, H. S. and Rowe, H., 2012. Lithofacies of the Wolfcamp and Lower Leonard Intervals, Southern Midland Basin, Texas: University of Texas at Austin, Bureau of Economic Geology Report of Investigations No 281, 67 p.

Beall, J.L., 1999. Wolfcampian (lower Permian) Platform and Basin Carbonates: Hueco Mountains and Midland Basin, West Texas.

Bertrand, P., Shimmield, G., Martinez, P., Grousset, F., Jorissen, F., Paterne, M., Pujol, C., Bouloubassi, I., Menard, P.B., Peypouquet, J.P. and Beaufort, L., 1996. The glacial ocean productivity hypothesis: the importance of regional temporal and spatial studies. Marine Geology, 130(1-2), pp.1-9.

Blakey, R.C., 2003, August. Carboniferous–Permian paleogeography of the assembly of Pangaea. In Proceedings of the XVth International Congress on Carboniferous and Permian Stratigraphy. Utrecht (Vol. 10, p. 16).

Blakey, R., 2005, <http://jan.ucc.nau.edu/rcb7/namP290.jpg>, accessed April 2017.

Bouma, A.H., Kuenen, P.H. and Shepard, F.P., 1962. Sedimentology of some flysch deposits: a graphic approach to facies interpretation (Vol. 168). Amsterdam: Elsevier.

Brown, L.F., Raúl Fernando Solís I. and Johns, D.A., 1987. Regional stratigraphic cross sections, Upper Pennsylvanian and Lower Permian strata (Virgilian and Wolfcampian Series), north-central Texas. Bureau of Economic Geology, University of Texas at Austin.

Brown, L.F., Solís-Iriarte, R.F. and Johns, D.A., 1990. Regional depositional systems tracts, paleogeography, and sequence stratigraphy, upper Pennsylvanian and lower Permian strata, North-and-West-Central Texas.

Carvalho, M.V.F., De Ros, L.F., Gomes, N.S., 1995. Carbonate cementation patterns and diagenetic reservoir facies in the Campos Basin Cretaceous turbidites, offshore eastern Brazil. Marine and Petroleum Geology 12, 741–758.

Calvert, S.E., Pedersen, T.F., 1993. Geochemistry of recent oxic and anoxic sediments: implications for the geological record. Mar. Geol. 113, 67–88.

Cook, H. E., 1983, Ancient carbonate platform margins, slopes and basins, in SEPM Short Course 12: Platform margin and deep water carbonates, p. 5-1–5-189.

Crowell, J. C., 1999, Pre-Mesozoic ice ages: Their bearing on understanding the climate system: Geological Society of America Memoir 192, p. 1–106.

Crowley, T.J. and Baum, S.K., 1991. Estimating Carboniferous sea-level fluctuations from Gondwanan ice extent. Geology, 19(10), pp.975-977.

Crowley, T.J. and Baum, S.K., 1992. Modeling late Paleozoic glaciation. Geology, 20(6), pp.507-510.

Dahl, T.W., Ruhl, M., Hammarlund, E.U., Canfield, D.E., Rosing, M.T. and Bjerrum, C.J., 2013. Tracing euxinia by molybdenum concentrations in sediments using handheld X-ray fluorescence spectroscopy (HHXRF). Chemical Geology, 360, pp.241-251.

Davies, Graham R. "Turbidites Debris Sheets and Truncation Structures in Upper Paleozoic Deep-Water Carbonates of the Sverdrup Basin, Arctic Archipelago." (1977).

Dean, W., Gardner, J., Piper, D., 1997. Inorganic geochemical indicators of glacial – interglacial changes in productivity and anoxia on the California continental margin. Geochim. Cosmochim. Acta. 61, pp. 4507 – 4518.

Demaison, G.J. and Moore, G.T., 1980. Anoxic environments and oil source bed genesis. Organic geochemistry, 2(1), pp.9-31.

Dunham, R.J., 1962. Classification of carbonate rocks according to depositional textures.

Dutton, S.P., Hamlin, H.S., Folk, R.L. and Clift, S.J., 1996. Early siderite cementation as a control on reservoir quality in submarine fan sandstones, Sonora Canyon gas play, Val Verde Basin, Texas.

Dutton, S.P, Kim, E.M., Broadhead, R.F., Raatz, W.D., Breton, C.L., Ruppel, S.C, and Kerans, C., 2005, Play analysis and leading-edge oil-reservoir development methods in the Permian basin: Increased recovery through advanced technologies, AAPG Bulletin, v. 89, no. 5, p. 553–576.

Ehrenberg, S. N., A. A. M. Aqrawi, and P. H. Nadeau, 2008, An overview of reservoir quality in producing Cretaceous strata of the Middle East: Petroleum Geoscience, v. 14, p. 307–318, doi:10.1144/1354-079308-783.

Elam, J.G. and Chuber, S. eds., 1972. Cyclic sedimentation in the Permian basin (No. 72). West Texas Geological Society.

Ewing, T. E., 1993, Erosional margins and patterns of subsidence in the late Paleozoic West Texas Basin and adjoining basins of West Texas and New Mexico: New Mexico Geological Society, guidebook prepared for the 44th Field Conference, Carlsbad Region, New Mexico and West Texas, p. 155–166.

Fielding, C.R., Frank, T.D. and Isbell, J.L., 2008a. The late Paleozoic ice age—A review of current understanding and synthesis of global climate patterns. Geological Society of America Special Papers, 441, pp.343-354.

Fielding, C.R., Frank, T.D., Birgenheier, L.P., Rygel, M.C., Jones, A.T. and Roberts, J., 2008b. Stratigraphic imprint of the Late Palaeozoic Ice Age in eastern Australia: a record of alternating glacial and nonglacial climate regime. Journal of the Geological Society, 165(1), pp.129-140.

Flamm, D. S., 2008 Wolfcampian Development of the Nose of the Eastern Shelf of the Midland Basin, Glasscock, Sterling and Reagan Counties: Master thesis, Brigham Young University, Provo, Utah, 54 p.

Flügel, E., 2004. Microfacies Data: Fabrics. In Microfacies of Carbonate Rocks (pp. 177-242). Springer Berlin Heidelberg.

Folk, R. L. (1980). Petrology of sedimentary rocks. Hemphill Publishing Company

Frakes, L.A., Francis, J.E. and Syktus, J.I., 1992. Climate Modes of the Phanerozoic Cambridge University Press Cambridge. UK Google Scholar.

Frakes, L.A. and Francis, J.E., 1988. A guide to Phanerozoic cold polar climates from high-latitude ice-rafting in the Cretaceous. Nature, 333(6173), pp.547-549.

Frenzel, H. N., et al., 1988, The Permian basin region, in L. L. Sloss, ed., Sedimentary cover—North American craton; U.S.: Boulder, Colorado, Geological Society of America, The Geology of North America, v. D-2, p. 261– 306.

Fu, Q., 2015, Wolfcamp Platform Carbonate and Basinal Facies in the Midland Basin: SEPM-PBS Meeting, < https://www.pbs-sepm.org/wp-content/uploads/2015/10/Wolfcamp-in-the-Midland-Basin_SEPM-PBS.pdf>

Fu, Q., R.W. Baumgardner, Jr., and H. S. Hamlin, Early Permian (Wolfcampian) Succession in the Permian Basin: Icehouse Platform, Slope Carbonates, and Basinal Mudrocks, in press

Garzanti, Eduardo. "Non-carbonate intrabasinal grains in arenites: their recognition, significance, and relationship to eustatic cycles and tectonic setting." Journal of Sedimentary Research 61.6 (1991).

Golonka, J., Ross, M.I. and Scotese, C.R., 1994. Phanerozoic paleogeographic and paleoclimatic modeling maps.

Golonka, J., and Kiessling, W. 2002. Phanerozoic time scale and definition of time slices. In Kiessling, W.; Flugel, E.; and Golonka, J., eds. Phanerozoic reef patterns. Tulsa, Okla., SEPM Spec. Publ. 72, p. 11–20.

Hamlin, H. S. and Baumgardner, R. W., 2012, Wolfberry (Wolfcampian-Leonardian) Deep-water Depositional Systems in the Midland Basin: Stratigraphy, Lithofacies, Reservoirs, and Source Rocks: University of Texas at Austin, Bureau of Economic Geology Report of Investigations No 277, 61 p.

Hentz, T.F., Ambrose, W.A. and Hamlin, H.S., Upper Pennsylvanian and Lower Permian Shelf-to-Basin Facies Architecture and Trends, Eastern Shelf of the Southern Midland Basin, West Texas. In Southwest Section AAPG Annual Convention.

Hills, J. M, 1972, Late Paleozoic Sedimentation in West Texas Permian Basin: American Association of Petroleum Geologists Bulletin, v. 56, p. 2303-2322.

Holterhoff, P., 2010. Sequence Stratigraphy and Depositional Systems of the Eastern Shelf Lower Permian, Central Texas: Examining the Tropical Record of Late Paleozoic Climate Change. Permian Basin Section Sepm.

Horak, R. L., 1985, Tectonic and hydrocarbon maturation history in the Permian basin: Oil & Gas Journal, May 27, v. 83, no. 21, p. 124– 129.

Houseknecht D W, Ross Jr L M., 1992, Clay minerals in Atokan deep-water sandstone facies, Arkoma basin: origins and influence on diagenesis and reservoir quality.

Isbell, J.L., Miller, M.F., Wolfe, K.L. and Lenaker, P.A., 2003. Timing of late Paleozoic glaciation in Gondwana: Was glaciation responsible for the development of Northern Hemisphere cyclothems?. SPECIAL PAPERS-GEOLOGICAL SOCIETY OF AMERICA, pp.5-24.

Ingall, E.D., Bustin, R.M. and Van Cappellen, P., 1993. Influence of water column anoxia on the burial and preservation of carbon and phosphorus in marine shales. Geochimica et Cosmochimica Acta, 57(2), pp.303-316.

Johnston, T.W., 2012. Integrated Analysis and Application of Reservoir Models to Early Permian Detrital Carbonate Deposits, Midland Basin, Texas (Doctoral dissertation, Texas A&M University).

Kerans, C. and Kempter, K., 2002. Hierarchical stratigraphic analysis of a carbonate platform, Permian of the Guadalupe Mountains. Bureau of Economic Geology, The University of Texas at Austin.

Kim, E.M. and Ruppel, S.C., 2005. Oil and Gas Production in Texas. Bureau of Economic Geology Pub. 2.

Lazar, O.R., Bohacs, K.M., Macquaker, J.H., Schieber, J. and Demko, T.M., 2015. Capturing key attributes of fine-grained sedimentary rocks in outcrops, cores, and thin sections: nomenclature and description guidelines. Journal of Sedimentary Research, 85(3), pp.230-246.

Lowe, D.R., 1982. Sediment gravity flows: II Depositional models with special reference to the deposits of high-density turbidity currents. Journal of Sedimentary Research, 52(1).

Loucks, R.G. and Ruppel, S.C., 2007. Mississippian Barnett Shale: Lithofacies and depositional setting of a deep-water shale-gas succession in the Fort Worth Basin, Texas. AAPG bulletin, 91(4), pp.579-601.

Loucks, R.G., Reed, R.M., Ruppel, S.C. and Jarvie, D.M., 2009. Morphology, genesis, and distribution of nanometer-scale pores in siliceous mudstones of the Mississippian Barnett Shale. Journal of sedimentary research, 79(12), pp.848-861.

Loucks, R.G., Reed, R.M., Ruppel, S.C. and Hammes, U., 2012. Spectrum of pore types and networks in mudrocks and a descriptive classification for matrix-related mudrock pores. AAPG bulletin, 96(6), pp.1071-1098.

Mansurbeg, Howri, et al. "Diagenesis and reservoir quality evolution of palaeocene deep-water, marine sandstones, the Shetland-Faroes Basin, British continental shelf." Marine and Petroleum Geology 25.6 (2008): 514-543.

Mazzullo, S. J., and Reid, A. M., 1987, Basinal lower Permian facies, Permian Basin: Part II—Depositional setting and reservoir facies of Wolfcampian-Lower Leonardian basinal carbonates: West Texas Geological Society Bulletin, v. 26, no. 8, p. 5–9.

Mazzullo, S.J. and Reid, A.M., 1989. Lower Permian platform and basin depositional systems, northern Midland Basin, Texas.

Meisler, H., Leahy, P.P., Knobel, L.L., 1984. Effect of eustatic sea-level changes on saltwater-freshwater in the northern Atlantic coastal plain. US Geological Survey Water-Supply Paper 2255, 28.

Milliken, K.L., Rudnicki, M., Awwiller, D.N. and Zhang, T., 2013. Organic matter–hosted pore system, Marcellus formation (Devonian), Pennsylvania. AAPG bulletin, 97(2), pp.177-200.

Montgomery, S.L., 1996, Permian “Wolfcamp” Limestone Reservoirs: Powell Ranch Field, Eastern Midland Basin, AAPG Bulletin, v. 80, no. 9, p.1349-1365.

Morad, S., Al-Ramadan, K., Ketzer, J.M. and De Ros, L.F., 2010. The impact of diagenesis on the heterogeneity of sandstone reservoirs: A review of the role of depositional facies and sequence stratigraphy. AAPG bulletin, 94(8), pp.1267-1309.

Morgan, W.A., Clopine, W.W., Kokkoros, G.F. and Wiley, B.H., 1996. Sequence stratigraphic framework and exploration potential of lower Permian (Wolfcampian) gravity-flow deposits, eastern Midland Basin, Texas. AAPG Bulletin, 5(CONF-960527--).

Mort, H., Jacquat, O., Adatte, T., Steinmann, P., F€ollmi, K., Matera, V., Berner, Z., Stüben, D., 2007. The Cenomanian/Turonian anoxic event at the Bonarelli Level in Italy and Spain: enhanced productivity and/or better preservation? Cretac. Res. 28, 597-612.

Mozley, P.S., 1989. Relation between depositional environment and the elemental composition of early diagenetic siderite. Geology, 17(8), pp.704-706.

Mulder, T. and Alexander, J., 2001. The physical character of subaqueous sedimentary density flows and their deposits. Sedimentology, 48(2), pp.269-299.

Murphy, A.E., Sageman, B.B., Hollander, D.J., Lyons, T.W. and Brett, C.E., 2000. Black shale deposition and faunal overturn in the Devonian Appalachian basin: Clastic starvation, seasonal water-column mixing, and efficient biolimiting nutrient recycling. Paleoceanography, 15(3), pp.280-291.

Peters, K.E., 1986. Guidelines for evaluating petroleum source rock using programmed pyrolysis. AAPG bulletin, 70(3), pp.318-329.

Pearce, T.J. and Jarvis, I., 1992. Applications of Geochemical Data to Modeling Sediment Dispersal Patterns in Distal Turbidites: Late Quaternary of the Madeira Abyssal Plain. J. of Sedimentary Petrology 62 (6): 1112-1129.

Pearce, T.J., Besly, B.M., Wray, D.S. and Wright, D.K., 1999. Chemostratigraphy: a method to improve interwell correlation in barren sequences—a case study using onshore Duckmantian/Stephanian sequences (West Midlands, UK). Sedimentary Geology, 124(1), pp.197-220.

Pedersen, T.F., Calvert, S.E., 1990. Anoxia vs. productivity: what controls the formation of organic-carbon-rich sediments and sedimentary Rocks? AAPG Bull. 74, 454-466.

Playton, T.E., and Kerans, C., 2002, Slope and Toe-of-Slope Deposits Shed from a Late Wolfcampian Tectonically Active Carbonate Ramp Margin, GCAGS Transactions, v. 52, p. 811-820.

Plink-Bjo¨rklund, P., Steel, R., 2004. Initiation of turbidity currents: evidence for hyperpycnal flow turbidites in Eocene Central Basin of Spitsbergen. Sedimentary Geology 165, 29–52.

Poole, F. G., W. J. Perry, Jr., P. Madrid, and R. Amaya-Martinez, 2005, Tectonic synthesis of the Ouachita-Marathon-Sonora orogenic margin of southern

Laurentia: stratigraphic and structural implications for timing of deformational events and plate tectonic model: Geological Society of America Special Paper 393, p. 543-596.

Rimmer, S.M., 2004. Geochemical paleoredox indicators in Devonian–Mississippian black shales, central Appalachian Basin (USA): Chemical Geology, v. 206, p. 373-391.

RL, A.J., 1982. Sedimentary structures, their character and physical basis (Vol. 1). Elsevier.

Rowe, H., Hughes, N. and Robinson, K., 2012. The quantification and application of handheld energy-dispersive x-ray fluorescence (ED-XRF) in mudrock chemostratigraphy and geochemistry. Chemical Geology, 324, pp.122-131.

Ross, C. A., 1986, Paleozoic evolution of the southern margin of the Permian Basin: Geological Society of America Bulletin, v. 97, p. 536–554.

Ross, C.A. and Ross, J.R., 1987. Late Paleozoic sea levels and depositional sequences. Cushman foundation for foraminiferal research, pp.137-149.

Ross, C.A. and Ross, J.R., 1988. Late Paleozoic transgressive-regressive deposition.

Ross, J.P.R. and Ross, C.A., 1990. Late Palaeozoic bryozoan biogeography. Geological Society, London, Memoirs, 12(1), pp.353-362.

Sageman, B.B., Murphy, A.E., Werne, J.P., Ver Straeten, C.A., Hollander, D.J. and Lyons, T.W., 2003. A tale of shales: the relative roles of production, decomposition, and dilution in the accumulation of organic-rich strata, Middle–Upper Devonian, Appalachian basin. Chemical Geology, 195(1), pp.229-273.

Sarg, J.F., Markello, J.R. and Weber, L.J., 1999. The second-order cycle, carbonate-platform growth, and reservoir, source, and trap prediction.

Schlumberger Well Services, 1983, Schlumberger Open Hole Services Catalog: Houston, TX

Schmitz, B., Charisi, S.D., Thompson, E.I. and Speijer, R.P., 1997. Barium, SiO2 (excess), and P2O5 as proxies of biological productivity in the Middle East during

the Palaeocene and the latest Palaeocene benthic extinction event. Terra Nova, 9(2), pp.95-99.

Silver, B.A. and Todd, R.G., 1969. Permian cyclic strata, northern Midland and Delaware basins, west Texas and southeastern New Mexico. AAPG Bulletin, 53(11), pp.2223-2251.

Stow, D.A. and Piper, D.J.W., 1984. Deep-water fine-grained sediments: facies models. Geological Society, London, Special Publications, 15(1), pp.611-646.

Stow, D.A.V., Huc, A.Y. and Bertrand, P., 2001. Depositional processes of black shales in deep water. Marine and Petroleum Geology, 18(4), pp.491-498.

Suess, E., 1980. Particulate organic carbon flux in the oceans: surface productivity and oxygen utilization. Nature 288, 260– 263.

Tribovillard, N., Desprairies, A., Lallier-Vergès, E., Moureau, N., Ramdani, A., Ramanampisoa, L., 1994. Geochemical study of organic-rich cycles from the Kimmeridge Clay Formation of Yorkshire (G.B.): productivity vs. anoxia. Palaeogeogr. Palaeoclimatol. Palaeoecol. 108, 165–181.

Tribovillard, N., Algeo, T.J., Lyons, T. and Riboulleau, A., 2006. Trace metals as paleoredox and paleoproductivity proxies: an update. Chemical geology, 232(1), pp.12-32.

Tyson, R.V., 1995. Sedimentary Organic Matter: Organic Facies and Palynofacies. Chapman & Hall, London. 615 pp.

Udden, J.A., Baker, C.L., and Bose, Emil, 1916, Review of the geology of Texas: University of Texas Bulletin, no. 44, p. 164.

Ulmer-Scholle, D.S., Scholle, P.A., Schieber, J. and Raine, R.J., 2014. A color guide to the petrography of sandstones, siltstones, shales and associated rocks. American Association of Petroleum Geologists.

Veevers, J. J., and C. M. Powell, 1987, Late Paleozoic glacial episodes in Gondwanaland reflected in transgressive-regressive depositional sequences in Euramerica: Geological Society of America Bulletin, v. 98, p. 475–487.

Walker, D. A., J. Golonka, A. Reid, and S. Reid, 1995, The effects of paleolatitude and paleogeography on late Paleozoic carbonate sedimentation in West Texas: West Texas Geological Society Bulletin 34, p. 5-15.

Wang, C., Wang, Q., Chen, G., He, L., Xu, Y., Chen, L. and Chen, D., 2017. Petrographic and geochemical characteristics of the lacustrine black shales from the Upper Triassic Yanchang Formation of the Ordos Basin, China: Implications for the organic matter accumulation. Marine and Petroleum Geology.

Wilde, G. L., 1975, Fusulinid-defined Permian stages, in Permian exploration, boundaries, and stratigraphy: WTGS and PBS-SEPM Publication No. 75–65, p. 67–83.

Wilkin, R.T., Arthur, M.A. and Dean, W.E., 1997. History of water-column anoxia in the Black Sea indicated by pyrite framboid size distributions. Earth and Planetary Science Letters, 148(3-4), pp.517-525.

Wilson, A.M., Garvin, G., Boles, J.R., 1999. Paleohydrology of the San Joaquin Basin, California. Geological Society of America Bulletin 111, 432–449.

Vita

Hualing Zhang was born in Xinjiang, China. This small but bustling regional capital, was a launching pad for her early interest in Geology since it's home to vast sedimentary basins, spectacular mountain ranges, and several national geological parks. She attend China University of Petroleum (Beijing) and was selected for a dual degree university exchange program with the University of Tulsa. After graduation, she began her Master degree program in Geological Science at the University of Texas at Austin. Her research focuses on sedimentation and unconventional reservoir characterization supervised by Dr. Xavier Janson and Dr. Qilong Fu.

Permanent address (or email): hualing-zhang@utexas.edu

This thesis (report) was typed by Hualing Zhang.